Delineation of the Nootka Fault Zone and Structure of the Shallow Subducted Southern Explorer Plate as Revealed by the Seafloor Earthquake Array Japan Canada Cascadia Experiment (SeaJade)

by

Jesse Hutchinson

B.Sc., Western Washington University, 2007
M.Sc., Western Washington University, 2012

A Dissertation Submitted in Partial Fulfillment of the Requirements for the Degree

of

DOCTOR OF PHILOSOPHY

in the School of Earth and Ocean Sciences

©Jesse Hutchinson, 2020
University of Victoria

All rights reserved. This dissertation may not be reproduced in whole or in part, by photocopy or other means, without the permission of the author.

Delineation of the Nootka Fault Zone and Structure of the Shallow Subducted Southern Explorer Plate as Revealed by the Seafloor Earthquake Array Japan Canada Cascadia Experiment (SeaJade)

by

Jesse Hutchinson

B.Sc., Western Washington University, 2007
M.Sc., Western Washington University, 2012

Supervisory Committee

Dr. Honn Kao, Co-Supervisor
School of Earth and Ocean Science

Dr. George Spence, Co-Supervisor
School of Earth and Ocean Science

Dr. Garry Rogers, Departmental Member,
School of Earth and Ocean Science

Dr. Eva Kwoll, Outside Member,
Department of Geography

Abstract

At the northern extent of the Cascadia subduction zone, the subducting Explorer and Juan de Fuca plates interact across a translational deformation zone, known as the Nootka fault zone. The Seafloor Earthquake Array Japan-Canada Cascadia Experiment (SeaJade) was designed to study this region. In two parts (SeaJade I and II, deployed from July – September 2010 and January – September 2014), seismic data from the SeaJade project has led to several important discoveries. Hypocenter distributions from SeaJade I and II indicate primary and secondary conjugate faults within the Nootka fault zone. Converted phase analysis and jointly determined seismic tomography with double-difference relocated hypocenters provide evidence to several velocity-contrasting interfaces seaward of the Cascadia subduction front at depths of ~4-6 km, ~6-9 km, ~11-14 km, and ~14-18 km, which have been interpreted as the top of the oceanic crust, upper/lower crust boundary, oceanic Moho, and the base of the highly fractured and seawater/mineral enriched veins within oceanic mantle. During SeaJade II, a M_W 6.4 mainshock and subsequent aftershocks, known as the Nootka Sequence, highlighted a previously unidentified fault within the subducted Explorer plate. This fault reflects the geometry of the subducting plate, showing downward bending of the plate toward the northwest. This plate bend can be attributed to negative buoyancy from margin parallel mantle flow induced by intraslab tearing further northwest. Seismic tomography reinforces the conclusions drawn from the Nootka Sequence hypocenter distribution. Earthquakes from the entire SeaJade II catalogue reveal possible rotated paleo-faults, identifying the former extent of the Nootka fault zone from ~3.5 Ma.

Table of Contents

Abstract ..... *iii*

Table of Contents ..... *iv*

List of Tables ..... *vii*

List of Figures ..... *viii*

Acknowledgements ..... *x*

Dedication ..... *xi*

Chapter 1 Introduction *1*

1.1 Purpose **1**

1.2 Thesis Outline **1**

Chapter 2 Seismic Characteristics of the Nootka Fault Zone: Results from the Seafloor Earthquake Array Japan–Canada Cascadia Experiment (SeaJade) *3*

2.1 Article Information **3**

2.1.1 Author and Coauthor Contributions 3

2.1.2 Citation 3

2.1.3 Author's Names and Affiliations 4

2.1.4 Data and Resources 4

2.2 Abstract **4**

2.3 Introduction **5**

2.4 Data and Methods of Analysis **8**

2.5 Results **18**

2.5.1 Three-Dimensional Distribution of Relocated Seismicity 18

2.5.2 Tomography 23

2.5.3 Converted Phases 30

2.5.4 Focal Mechanisms 39

2.6 Interpretations and Discussion **41**

2.6.1 Fault Distribution Within the Nootka Fault Zone 41

2.6.2 Interface Depths of the Juan de Fuca and Explorer Plates 43

2.6.3 Fracturing and Seawater Infiltration of the Oceanic Mantle 45

2.6.4 Variation of Seismogenic Depth for Major Faults 49

2.6.5 Abutment of the Explorer Plate by the Juan de Fuca Plate 50

2.7 Conclusion **51**

2.8 Supplementary Materials **52**

2.8.1 Hypocenter Uncertainty 52

2.8.2 *b*-value 53

2.8.3 Tomography Resolution 54

2.8.4 Detailed Discussion of Tomographic Velocity Anomalies 55

Chapter 3 Significant geometric variation of the subducted plate beneath the northernmost Cascadia subduction zone and its tectonic implications as revealed by the 2014 M_W 6.4 earthquake sequence 58

3.1 Article Information 58
3.1.1 Author and Coauthor Contributions 58
3.1.2 Citation 58
3.1.3 Author's Names and Affiliations 59
3.1.4 Data and Resources 59

3.2 Abstract 60

3.3 Introduction 60

3.4 Data and Analysis 63

3.5 Results and Implications 67
3.5.1 Rupture Zones of the Nootka Sequence 70
3.5.2 Geometric variation of the oceanic plate across the JdF-ExP boundary 77

3.6 Discussion and Conclusion 82

3.7 Supplementary Materials 84
3.7.1 Estimation of Hypocenter Uncertainty 84
3.7.2 Verification of Source Depths for Two Representative Events 85

Chapter 4 Shallow tomographic imaging and hypocenter distribution of the Nootka fault zone and the subducting Juan de Fuca/Explorer plate in northern Cascadia as revealed by SeaJade II 86

4.1 Article Information 86
4.1.1 Author and Coauthor Contributions 86
4.1.2 Citation 86
4.1.3 Author's Names and Affiliations 87
4.1.4 Data and Resources 87

4.2 Abstract 88

4.3 Introduction 88

4.4 Methods and Data Analysis 91

4.5 Results and Interpretations 96
4.5.1 Hypocenter Distribution 97
4.5.2 Seismic Tomography 101
4.5.3 Focal Mechanism Solutions and Implications 110

4.6 Discussion and Conclusions 113
4.6.1 Northwestward Bending and Deformation of the Shallow Subducted Explorer Plate 113
4.6.2 Evolution of the NFZ 114
4.6.3 Focal Mechanisms and Regional Tectonics 117

Chapter 5 Conclusions 119

References 122

Appendix A Earthquake Datasets 137

Appendix B Focal Mechanism Datasets 138
Appendix C Tomography Datasets 140

List of Tables

Table 2.1. Average hypocenter uncertainties determined by method and subset area. 9
Table 2.2. Gutenberg-Richter parameters as determined by various methods. 12
Table 2.3. Focal mechanism solutions for selected events from the SeaJade earthquake catalogue. 17
Table 2.4. Hypocenter lineations/zones and associated attributes. 20
Table 2.5. Average discontinuity depths determined from converted phases. 37
Table 3.1. Moment-tensor solutions for large Nootka Sequence events.....66
Table 4.1. Hypocenter lineations/zones and associated attributes. 100
Table 4.2. Representative average focal mechanism solutions for selected areas. 112

Appendix Table A.1. Arrival information for the relocated hypocenters for SeaJade I. 137
Appendix Table A.2. Hypocenter information for the relocated events for SeaJade I. 137
Appendix Table A.3. Arrival information for the relocated hypocenters for SeaJade II. 137
Appendix Table A.4. Hypocenter information for the relocated events for SeaJade II. 137
Appendix Table B.1. Focal mechanism information for events from SeaJade I. 138
Appendix Table B.2. Focal mechanism information for events from SeaJade II. 139
Appendix Table C.1. P-wave tomography model for SeaJade I. 143
Appendix Table C.2. S-wave tomography model for SeaJade I. 143
Appendix Table C.3. P-wave tomography model for SeaJade II. 143
Appendix Table C.4. S-wave tomography model for SeaJade II. 144

List of Figures

Figure 2.1. Map of the study region, located off the western coast of British Columbia, Canada. 6
Figure 2.2. Map of initial earthquake hypocenters 10
Figure 2.3. Map of earthquakes relocated using the double-difference method. 11
Figure 2.4. The Gutenberg-Richter distribution 13
Figure 2.5. Maps showing the results of synthetic checkerboard tests 14
Figure 2.6. Representative cross-sections of the synthetic checkerboard test results 15
Figure 2.7. Detailed maps showing seismogenic structures and earthquake source characteristics 19
Figure 2.8. Depth distribution (below sea level) of relocated earthquakes within groups E1-E8 21
Figure 2.9. Maps showing TomoDD tomography inversion results 25
Figure 2.10. Maps showing TomoDD tomography inversion results 26
Figure 2.11. Tomographic profiles of the study area 28
Figure 2.12. Tomographic profiles of the study area 29
Figure 2.13. Additional tomographic profiles to those shown in Figure 2.12 30
Figure 2.14. Example waveforms showing converted phases 32
Figure 2.15. Raypaths corresponding to the waveform examples shown in Figure 2.14 33
Figure 2.16. Histograms of the depth to interfaces 35
Figure 2.17. Histograms of the depth to interfaces 38
Figure 2.18. Focal mechanisms solutions for the A and B-ranked events 40
Figure 2.19. A schematic diagram summarizing the distribution of seismogenic structures 43
Figure 2.20. Left) Strength and temperature profile for the Nootka fault zone 47
Figure 3.1. Map of the study area of the 2014 Nootka Sequence and the Nootka fault zone 61
Figure 3.2. Top) Distribution of the number of earthquakes by day 68
Figure 3.3. Daily distribution of local earthquake magnitude (M_L) of 69
Figure 3.4. Gutenberg-Richter relationships for the Nootka Sequence 70
Figure 3.5. Top) Map focusing on the Nootka Sequence earthquakes and selected focal mechanism solutions 71
Figure 3.6. Profiles of earthquake hypocenters and selected focal mechanisms 73
Figure 3.7. Depth distributions of earthquakes along lines B-B' and C-C' 74
Figure 3.8. Seismograms of two select earthquakes (events no. 74 and 1149) 79
Figure 3.9. Illustrative diagrams of the two proposed plate geometries 81
Figure 4.1. Map of the study area of SeaJade II and the Nootka fault zone 90
Figure 4.2. Maps of checkerboard tomography resolution tests 95
Figure 4.3. Gutenberg-Richter distributions for earthquakes within the Nootka fault zone 97
Figure 4.4. Map of the study area and hypocenters that occurred during the deployment of SeaJade II 98
Figure 4.5. Detailed map of hypocenters focused on the Nootka fault zone 99
Figure 4.6. Depth slices of Vp of seismic tomography 102
Figure 4.7. Detailed V_P seismic tomography depth slices focusing mainly on the region landward of the subduction front 104
Figure 4.8. Depth slices of V_p/V_s seismic tomography 105

Figure 4.9. Cross-section profiles of Vp seismic tomography.....107
Figure 4.10. Cross-section profiles of seismic tomography with raypath density DWS contours 108
Figure 4.11. Maps of focal mechanism solutions 111
Figure 4.12. Illustrative diagram of the presumed evolution of the Nootka fault 115

Acknowledgements

I benefited from discussion with Kelin Wang, Garry Rogers, Michael Bostock, Kristin Rohr, Michael Riedel, John Cassidy, Shuoshuo Han, and Roy Hyndman. Ayodeji Kuponiyi, Lonn Brown, Jess-C Hall, Subbarao Yelisetti, Tian Sun, and Isa Asudeh provided dedication and time for location scouting and the deployment of the SeaJade II land component. Dawei Gao and Lingmin Cao kindly contributed to reviewing earthquake locations for a subset of the data. High resolution bathymetry data from the NEPTUNE (North East Pacific Time-series Underwater Networked Experiments) archive was provided by Michael Riedel and converted to GMT format by Robert Kung. I am grateful to the SeaJade I and II cruise team for their effort in station deployment and data retrieval. I appreciate the Canadian Hazard Information Service for technical assistance in processing CNSN waveforms. This research was partially funded by a University of Victoria Fellowship to JH, a NSERC Discovery grant to HK, and a NSERC Discovery grant to GS. This analysis benefited from the use of the programs Antelope (BRTT), HASH (USGS; Hardebeck and Shearer, 2002), HypoDD (Waldhauser, 2001), TomoDD (Zhang and Thurber, 2003), GMT (Wessel and Smith, 1998), and the Python programming language, including the Obspy library.

Dedication

This dissertation is dedicated to quite a few people, without whom I could not have maintained my sanity or tackled such a large endeavour.

To my family who saw me through childhood until now; Mom, Dad, Joe, and David. You fostered my curiosity and gave me the courage to always strive for more.

To my wife, Lauren, and my two children, Lily and Joshua. Lauren, you are the love of my life and you are my happiness. Lily and Josh, you came to me during my time as a Ph.D. student, and I am more proud of you than anything. My heart has grown immeasurably because of you.

To my friends. Among them, Ayo, Lonn, William, Jess, Jess-C, Romina, Brindley, Tian, and more names than I have room for. And especially to Ryan for putting up with me through long conversations and many lunches at the Fickle Fig.

To my supervisors and mentors. Honn, for your patience and tutelage I cannot express enough gratitude. Jackie, you helped me find passion in geophysics. John, I wouldn't have dreamed of going to UVic without your encouragement. George, you inspire the scientist in me.

Last, I would be remiss to mention the time in which this dissertation was published. The coronavirus known as COVID-19 struck the world this year and has changed life as we know it. Now, more than ever, I appreciate my family, friends, and colleagues. With all my hope, I wish for a bright future.

There are, of course, so many others who have helped me on this journey. Thank you to everyone who lent an ear, a hand, a bow, or an axe.

Chapter 1 Introduction

The northern Cascadia subduction zone is divided into two subducting plates beneath the North America plate; the Juan de Fuca plate which extends from northern California to central Vancouver Island, and the Explorer plate. The transition between these two oceanic plates is known as the Nootka fault zone.

This thesis is an investigation of the northern Cascadia subduction zone and the Nootka fault zone, located off the western coast of Vancouver Island, British Columbia. While much of the Cascadia subduction zone is seismically quiescent, the Nootka fault zone consistently experiences earthquakes, some greater than M_W 6.

Until recently, the exact locations of earthquakes in this region have been difficult to determine because of the strict use of land-based seismometers. With the use of ocean-bottom seismometers (OBS), precise hypocenters can be located, delineating deep fault structures, and contributing to our understanding of northern Cascadia.

1.1 Purpose

This study was conducted over two OBS network deployments. The project, known as the Seafloor Earthquake Array Japan Canada Cascadia Experiment (SeaJade), was developed to study the unusually quiet Cascadia subduction zone. Over the course of two phases, the objective of this thesis was to delineate the distribution of hypocenters within the Explorer and Juan de Fuca plates, as well as within the Nootka fault zone. Further goals were to develop 3-D seismic velocity models, determine focal mechanisms, and to identify key velocity-contrasting interfaces within the oceanic slab in order to describe the geometry of the Explorer and Juan de Fuca plates after subduction.

1.2 Thesis Outline

This thesis is comprised of three separate manuscripts, each related to the SeaJade project. In Chapter 2, the results from the first phase of SeaJade are presented, which delineates the

Nootka fault zone and provides depth constraints to interfaces within the oceanic slab. Chapter 3 focuses on the seismogenic behavior of the 24 April 2014, M_W 6.4 earthquake and the subsequent aftershock sequence during the second phase of SeaJade, which manifests the bending and deformation of the subducted oceanic plates across the Nootka boundary zone. Chapter 4 continues the analysis of the second phase of SeaJade, providing the complete relocated hypocenter catalogue and detailed tomography that further support the findings in Chapter 3.

The final chapter, Chapter 5, is a summary of major findings in this research work. I review the most important topics from the prior chapters and finally provide suggestions for future research.

The Appendices provide much of the data used for my research. Appendix A includes earthquake arrival and relocation data from SeaJade phases I and II. Appendix B includes focal mechanism information from SeaJade I and II. Appendix C includes TomoDD input parameters and results for SeaJade I and II.

Chapter 2 Seismic Characteristics of the Nootka Fault Zone: Results from the Seafloor Earthquake Array Japan–Canada Cascadia Experiment (SeaJade)

Chapter 2 focuses on the delineation of the Nootka fault zone. The main body of this chapter consists of a published journal article (Hutchinson et al., 2019) formatted specifically for this dissertation. By utilizing earthquake hypocenter distributions, seismic tomography, focal mechanisms, and converted seismic phases, this study examines the distribution of faults within the Nootka fault zone as well as the structure of the oceanic plate prior to and immediately after subduction. Section 2.1 provides article information. Subsequent sections (2.2- 2.7) present the article in full. Supplementary material to the article is presented in Section 2.8

2.1 Article Information

2.1.1 Author and Coauthor Contributions

This chapter consists an article that has been reformatted from the journal *Bulletin of the Seismological Society of America*. The author of this dissertation, J. Hutchinson, carried out hypocenter relocations, double-difference tomography, focal mechanism calculations, and converted phase analysis. Coauthor H. Kao and J. Hutchinson jointly designed and wrote most of the study. Coauthor G. Spence advised writing style and background research. Coauthor K. Obana provided initial phase picks and hypocenters for earthquakes. Coauthor K. Wang developed the computer program used for calculating the stress diagram. Coauthors K. Wang and S. Kodaira led the SeaJade project. Coauthors K. Obana and S. Kodaira collected OBS waveform data. All coauthors provided useful feedback and contributions for refinement of the article.

2.1.2 Citation

Hutchinson, J., H. Kao, G. Spence, K. Obana, K. Wang, and S. Kodaira, 2019, Seismic Characteristics of the Nootka Fault Zone: Results from the Seafloor Earthquake Array Japan–Canada Cascadia Experiment (SeaJade), Bull. Seismol. Soc. Am., doi: 10.1785/0120190008.

2.1.3 Author's Names and Affiliations

Jesse Hutchinson[1], Honn Kao[1,2], George Spence[1], Koichiro Obana[3], Kelin Wang[1,2], and Shuichi Kodaira[3]

[1] School of Earth and Ocean Sciences, University of Victoria, Victoria, BC, V8P 5C2

[2] Pacific Geoscience Centre, Geological Survey of Canada, Natural Resources Canada, Sidney, BC, V8L 4B2

[3] Japan Agency for Marine-Earth Science and Technology (JAMSTEC), Yokohama, Japan

2.1.4 Data and Resources

Seismograms used in this study were collected as part of the SeaJade (Seafloor Earthquake Array – Japan Canada Cascadia Experiment) project. Arrival data, relocated hypocenters, P-wave tomography, and S-wave tomography can be found in Tables A.1, A.2, C.1, C.2. Waveform data can be obtained from JAMSTEC upon request.

The Natural Resources Canada - Earthquakes Canada database was searched using http://www.earthquakescanada.nrcan.gc.ca/stndon/NEDB-BNDS/bulletin-en.php (last accessed on January 24, 2017).

Some plots were made using the Generic Mapping Tools version 5.4.2 (http://gmt.soest.hawaii.edu/; Wessel and Smith 1998).

Global Multi-Resolution Topography (GMRT) was used to generate high resolution topography and bathymetry for GMT maps (Ryan et al., 2009).

2.2 Abstract

The Nootka fault zone (NFZ) divides the incoming Explorer and Juan de Fuca plates of the Cascadia subduction zone. Three months of seafloor monitoring using 33 ocean bottom seismometers (OBS) off the west coast of Vancouver Island has allowed us to better understand

the tectonic configuration and seismogenic characteristics of the NFZ. We have learned that the NFZ is comprised of northern and southern primary bounding faults, and several conjugate faults developed sub-perpendicular to the primary faults. Along the primary bounding and conjugate faults, earthquakes typically occur over the depth ranges of 15-20 km and 6-15 km, respectively. Focal mechanisms reveal that the most common modes of failure in this region are left-lateral strike-slip, with normal faulting occurring along the southwestern extent of the NFZ and thrust faulting to the northeast before the subduction front. Seismic tomography suggests that the oceanic Moho is at a depth of 12-14 km below sea level (10-12 km below seafloor) just seaward of the Cascadia deformation front, and that it deepens to 19 km (17 km below seafloor) approximately 20 km landward of the deformation front. Converted phase analysis illuminates 4 velocity-contrasting interfaces with average depths below sea level deepening landward of the subduction front at ~4-6 km, ~6-9 km, ~11-14 km, and ~14-18 km. We interpret them as the sedimentary basement, upper/lower crust boundary, oceanic Moho, and the base of the highly fractured and seawater/mineral enriched veins within mantle, respectively. The emplacement of minerals such as quartz or the formation of talc, which is made possible by the intense degree of fracturing within the NFZ facilitating the infiltration of seawater, may reduce mantle velocities, as well as V_P/V_S ratios. The lack of seismicity observed along the interplate thrust zone in northern Cascadia may suggest that the megathrust fault is completely locked, consistent with prior studies.

2.3 Introduction

The Nootka fault zone is a left-lateral transform boundary zone between the Juan de Fuca plate and the Explorer plate (Hyndman et al., 1979) located near the northern end of the Cascadia subduction zone (Figure 2.1). Although it is widely recognized that the Cascadia subduction zone is capable of producing megathrust earthquakes with M_w as high as 9.0 (e.g. Atwater et al. 1995; Satake et al. 2003; Leonard et al. 2010), exactly how the Nootka fault zone influences seismogenic behaviour in the northern Cascadia subduction zone is unclear, due mainly to its offshore setting without adequate coverage by land-based seismograph networks.

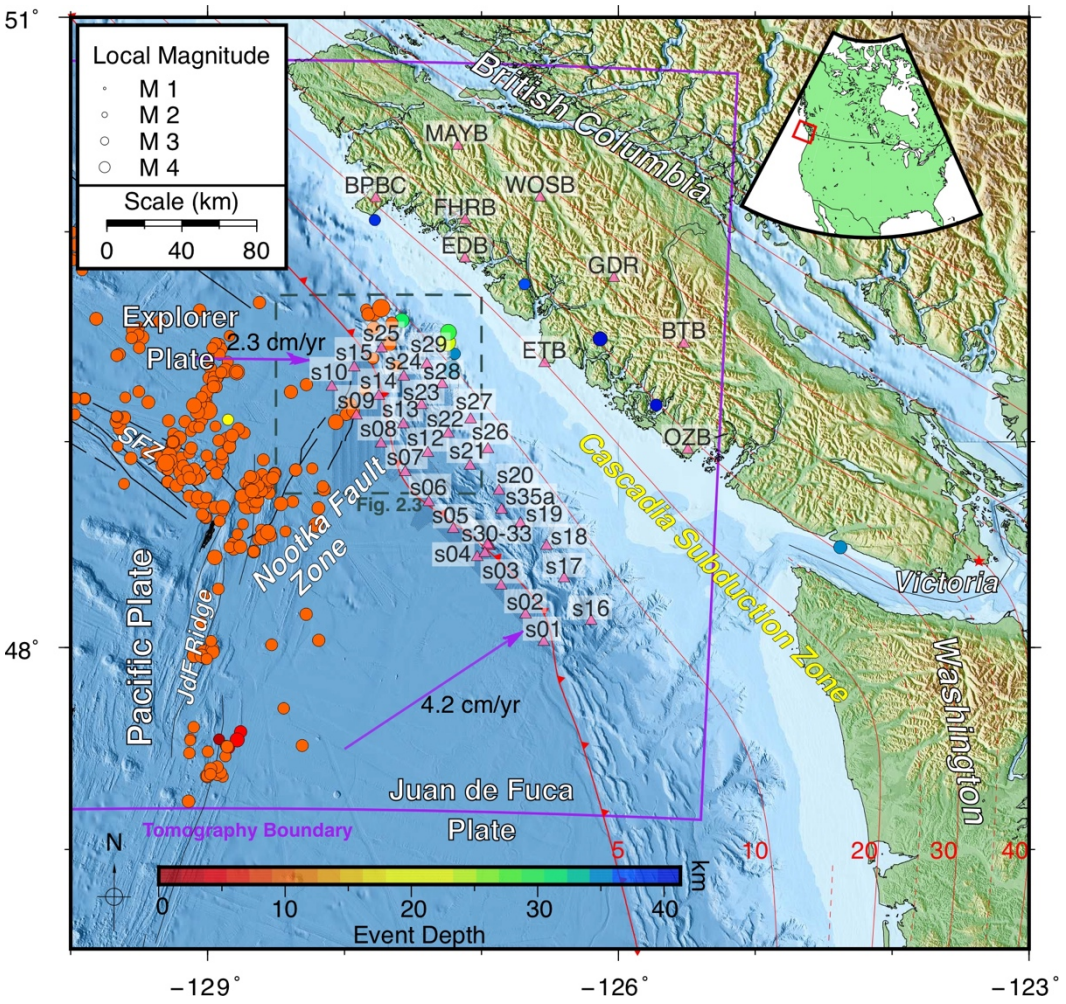

Figure 2.1. Map of the study region, located off the western coast of British Columbia, Canada. Pink triangles indicate the position of ocean-bottom-seismometers (OBS) deployed by the GSC and JAMSTEC for the first phase of SeaJade, as well as regional permanent seismograph stations on Vancouver Island. Submarine faults and mid-ocean ridges are shown with black lines. Red lines indicate the approximate location and depths of the Cascadia subduction zone (Gao et al., 2017; McCrory et al., 2012). Significant earthquakes since 2000 ($M_W \geq 4$) are shown as circles, with colour indicating depth (Natural Resources Canada online database). The bounds for tomographic inversion are shown with the purple box. The study area with respect to the North American continent is shown as a red box in the inset. Plate motions of the Explorer and Juan de Fuca plates with respect to North America are shown with purple arrows (Braunmiller and Nábělek, 2002; DeMets et al., 2010). The dashed grey box shows the bounds of Figure 2.3. The fault map of the Nootka fault zone is derived from Rohr et al., 2018. Quality of the bathymetry varies with the detail of bathymetry surveys. We use the highest resolutions where available. SFZ: Sovanco fracture zone.

The northernmost end of the Cascadia subduction zone is characterized by the subduction of the Explorer plate beneath the North America plate at a rate of 5–20 mm/yr (Braunmiller and Nábělek, 2002; Hyndman and Weichert, 1983; Leonard et al., 2010; Mazzotti et al., 2003; Riddihough, 1977). This rate is in contrast to the 40 mm/yr relative motion between the Juan de

Fuca and North America plates observed to the south of the Nootka fault zone (e.g. Wells and Simpson, 2001; Wang et al., 2003; McCaffrey et al., 2007). The existence and subduction of the Nootka fault zone imply that the physical conditions on the megathrust zone may vary dramatically across the downdip projection of the Juan de Fuca–Explorer plate boundary, as hinted by results of previous studies investigating the geometry of the subducted slab and the thermal regime (e.g. Audet et al. 2010; McCrory et al. 2012; Gao et al. 2017). Since the occurrence of giant megathrust earthquakes requires an extended rupture plane, whether or not the seismic properties of the Nootka fault zone can hinder the propagation of megathrust rupture may have important implications to regional seismic and tsunami hazards.

Seismically, the Nootka fault zone corresponds to a zone of shallow seismicity oriented at a high angle to the deformation front of the Cascadia subduction zone. The width of the fault zone as inferred from distinct multibeam bathymetric signatures and seismic reflection profiles varies slightly from about 15 km near the trench to about 25 km near the Juan de Fuca ridge (Rohr et al., 2018; Figure 2.1). While most of the Cascadia megathrust remains seismically silent, the adjacent Nootka fault zone frequently produces significant earthquakes (e.g., M_w 6.3 on Sept. 9, 2011, M_w 6.6 on Nov. 2, 2004 and M_w 6.3 on Oct. 6, 1996; Earthquakes Canada). However, detailed mapping of the Nootka fault zone subduction and the delineation of seismogenic structures could not be achieved in the past because high-quality seismic data were available only from land-based stations.

The Seafloor Earthquake Array Japan–Canada Cascadia Experiment (SeaJade, Figure 2.1) was an international collaborative project amongst the Japan Agency for Marine-Earth Science and Technology (JAMSTEC), the Geological Survey of Canada (GSC), the University of Victoria, the University of British Columbia, and the Woods Hole Oceanographic Institution (Scherwath et al., 2011). The purpose of its first phase (SeaJade I) is to better understand the seismogenesis near the deformation front of the Cascadia subduction zone, including the Nootka fault zone, by deploying 33 ocean-bottom seismometers (OBS) in the offshore area west of Vancouver Island (Figure 2.1) during 2010. Preliminary results have confirmed the highly active nature of local seismicity in the Nootka fault zone (Obana et al., 2015; Scherwath et al., 2011), but the detailed

distribution and characteristics of individual seismogenic structures within the Nootka fault zone remain unclear.

In this study, we conducted an analysis of the SeaJade I OBS dataset to jointly determine the distribution of local earthquakes using double-difference relocation and the corresponding three-dimensional (3-D) tomography for the Nootka fault zone and its surrounding area. We identified P-to-S and S-to-P converted phases and used them to further constrain the location and geometry of velocity-contrasting interfaces at depth. We also derived as many focal mechanisms as possible to constrain the deformation and kinematics of the Nootka fault zone. Our results suggest that the Nootka fault zone is a complex array of structures that has been highly fractured to depths down to 20 km below sea level (18 km below seafloor) within the uppermost mantle.

2.4 Data and Methods of Analysis

Data from 33 OBS sites and 9 regional stations from the Canadian National Seismograph Network (CNSN) were used to determine earthquake hypocenters. Locations of all seismograph stations used in this study are shown in Figure 2.1. The furthest stations, such as the southern OBS sites, OZB and BTB, yielded few to no arrivals, so more distant seismographs were not accessed for data. The 33 4.5 Hz short-period OBS, provided by JAMSTEC, recorded nearly three months (85 days) of data from early July to late September 2010 at the rate of 100 samples per second. Drift of the internal clock of each OBS was corrected by linear interpolation of the time differences between the OBS internal clock and a GPS-based reference clock. The time differences were measured just before deployment and shortly after recovery of each OBS. Overall, the data had a high signal-to-noise ratio due to the location of the OBS in the deeper ocean away from the continental shelf.

While hypocenters were initially determined by others (Obana et al., 2015; Scherwath et al., 2011), we have increased the number of P and S arrivals from 8,867 to 9,239 and from 16,626 to 17,057, respectively, by visually inspecting waveforms and performing additional manual phase picking. We used the commercial software Antelope with the dbgenloc package (Pavlis et

al., 2004) to determine hypocenters and the dbevproc package to determine local magnitude (M_L). In total, 1,276 earthquakes were located in our study (Figure 2.2). The 1-D velocity model used in our earthquake location process (Figure 2.3) was derived from Spence et al. (1985) and is the same as that used by Obana et al. (2015). Station corrections for individual OBS sites were adopted from the work of Obana et al. (2015). Mean uncertainties for the major, minor, and depth axes of the hypocentral ellipsoid, based on bootstrap resampling, were estimated to be 2.64 km, 1.49 km, and 3.05 km, respectively. Uncertainty estimates based on other methods are listed in Table 2.1 and discussed in Section 2.7.1 for readers who are interested in more technical details.

Table 2.1. Average hypocenter uncertainties determined by method and subset area.

Method	**Average Major Axis of Uncertainty Ellipse (km)**	**Average Minor Axis of Uncertainty Ellipse (km)**	**Average Depth Uncertainty (km)**
GENLOC[1]	0.55	0.09	2.47
GENLOC Subset[2]	0.08	0.04	0.27
Bootstrap[1]	3.96	1.61	3.65
Bootstrap Subset[2]	2.64	1.49	3.05
TomoDD SVD[1,3]	0.42	0.14	0.44
TomoDD SVD Subset[2,3]	0.38	0.12	0.39

[1] Results include the uncertainties for events outside of the study area, near the Sovanco fracture zone (SFZ).

[2] Results exclude uncertainties for events outside of the Nootka fault zone. These uncertainties best represent the events discussed in the study (i.e., within the area bounded by latitudes of 48° 45'N to 49° 42'N and longitudes of 128° 18'°W to 127°W).

[3] Results are derived from performing singular value decomposition (SVD) on a subset of 147 events in group E3 (i.e., within the area bounded by latitudes of 49°N to 49° 7' 30"N and longitudes of 128° 3' 45"W to 127° 54'W). SVD results were then divided by least-squares linearization (LSQR) results in order to derive mean ratios in X, Y, and Z directions that could be extrapolated across the full relocation catalogue to find mean uncertainties.

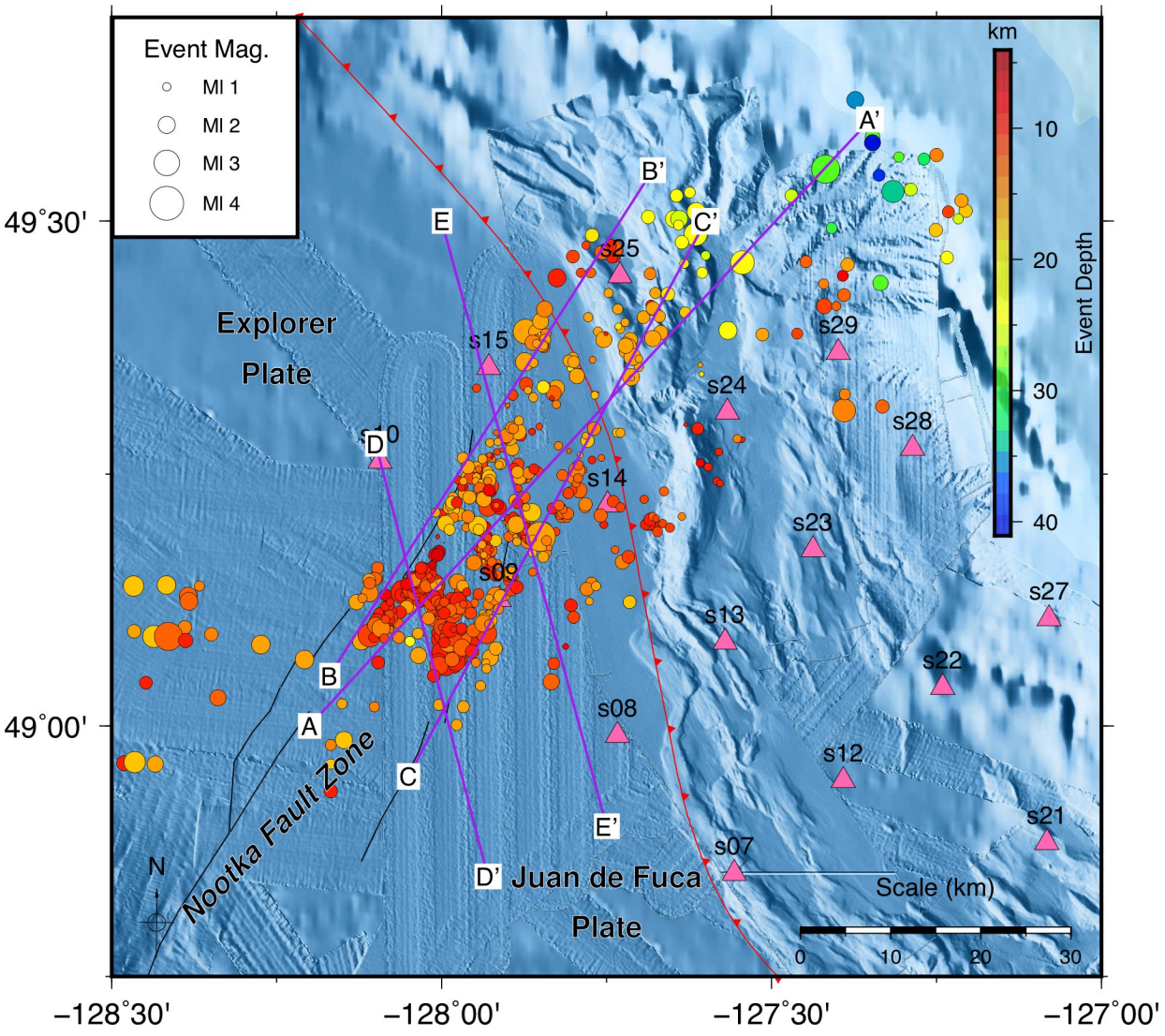

Figure 2.2. Map of initial earthquake hypocenters. One circle corresponds to one event. The size and colour of each circle correspond to its local magnitude (M_L) and focal depth. OBS stations are marked by pink triangles. The purple lines mark the location of cross-section shown in Figures 2.11 and 2.12.

The hypocentral distribution of the earthquakes were further adjusted (Figure 2.3) in our tomographic inversion using the program TomoDD (Zhang, 2003), which simultaneously determines locations, based on the double-difference method (Waldhauser, 2001), and a 3-D velocity model (Thurber and Eberhart-Phillips, 1999). For the initial model of the inversion, we extrapolated the 1-D model over a roughly 300-by-300 km grid (Figure 2.1), centered on 128°W, 49°N. There are 103 nodes in both X and Y directions at 3 km intervals and 28 nodes in the Z-direction mostly at 1 km intervals (with the exception of the first node, which is at a 1.3 km

interval), from an elevation of 1.3 km to a depth of 26 km. The base layer of our model is an approximate mantle half-space of 500 km.

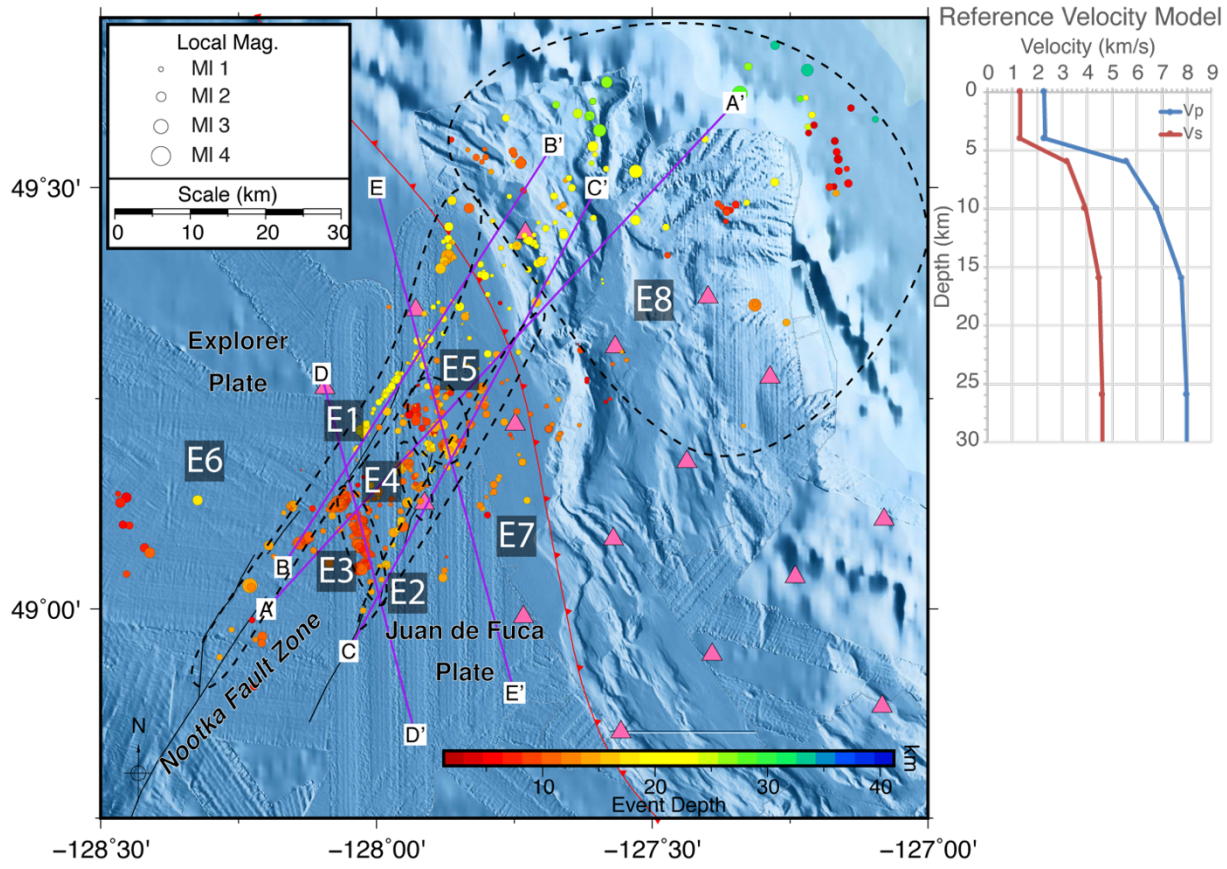

Figure 2.3. Map of earthquakes relocated using the double-difference method. Pink triangles mark the OBS. The purple lines, labelled A(A')-E(E'), are vertical transects shown in Figure 2.11. Earthquakes are indicated by colour-filled circles (colour indicates depth). Seismic features, including lineations of earthquakes and diffuse seismic zones, are outlined with black dashed lines and labelled E1-E8. The reference 1-D velocity model (Obana et al., 2015; Spence et al., 1985) used to locate initial hypocenters is shown to the right of the map.

Forty iterations were performed, initially weighted toward the absolute travel times of the P and S phases, followed by weighting toward travel-time differences between phases. Finally, differential travel times were weighted relative to each other based on the squared coherency of waveform cross-correlation coefficients. Meanwhile, we also increased the relative weighting of the absolute data over the relative data to best constrain absolute locations. Cross-correlation derived differential travel times were determined by calculating the arrival time lag between waveform pairs and applying it to the original differential travel times. The arrivals

used for relocation are included in Appendix Table A.1. The total number of differential travel-times used in our TomoDD inversion was 877,284, comprised of both catalogue and cross-correlation data. By the fortieth iteration, the absolute root-mean-square (RMS) values for the cross-correlation and catalogue travel-time residuals were 0.0843 s and 0.1327 s, respectively, compared to the initial values of 0.2083 s and 0.2520 s, respectively. It was found that the RMS values stabilized by the 28th iteration. Of the original 1,276 hypocenters, 1,052 were relocated by the joint inversion (see Appendix Table A.2). Resultant V_P and V_S tomography models were used to determine large-scale velocity anomalies, as well as perturbations in V_P/V_S ratios (see Appendix Tables C.1 and C.2). The mean hypocenter uncertainty was greatly improved by relocation with the major, minor, and depth axes of the hypocentral ellipsoid being 0.38 km, 0.12 km, and 0.39 km, respectively (Table 2.1 and Section 2.7.1).

Our catalogue of relocated events corresponds to a Gutenberg-Richter distribution with *a* and *b*-values of 3.96±0.12 and 1.07±0.08, respectively. The magnitude of completeness (M_C) is estimated to be 1.20±0.12 (Figure 2.4). The M_C, *b*-value, and *a*-value were determined with the median-based analysis of the segment slope method (MBASS; Amorèse, 2007). We also tested several other methods discussed in Mignan and Woessner (2012). Readers are referred to Table 2.2 and Section 2.8.2 for a detailed discussion of our *b*-value analysis.

Table 2.2. Gutenberg-Richter parameters as determined by various methods.

	MAXC	**GFT**	**MBS**	**EMR**	**MBASS**
Mc	1.04±0.06	1.23±0.15	1.37±0.13	0.94±0.23	1.21±0.13
***a*-value**	3.81±0.05	3.99±0.17	3.90±0.37	3.65±0.22	3.93±0.10
***b*-value**	0.96±0.03	1.07±0.10	1.0±0.23	0.85±0.15	1.05±0.07

The methods and results are discussed in Section 2.8.2. The standard deviations of the results were calculated by bootstrapping over 1,000 iterations.

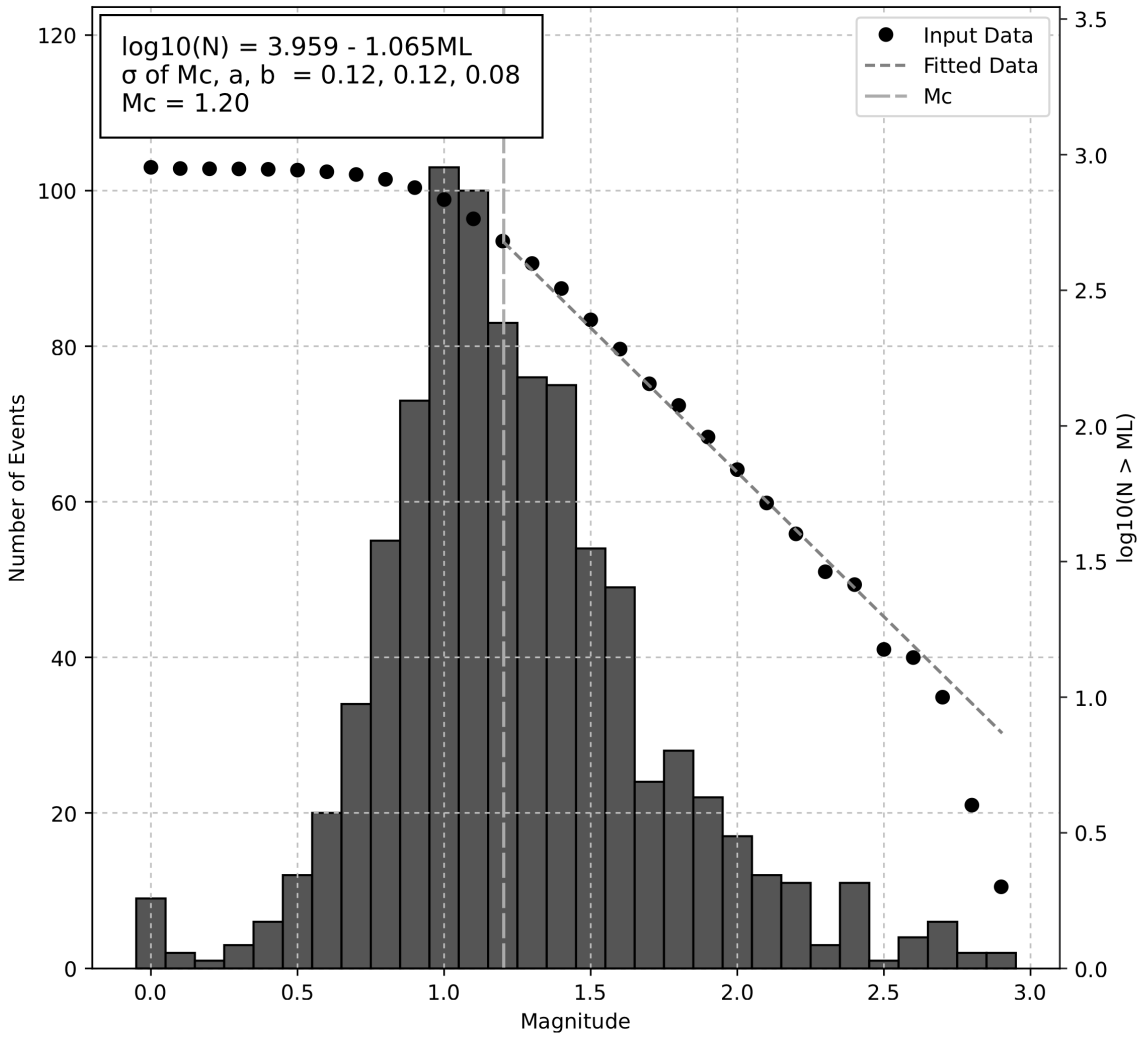

Figure 2.4. The Gutenberg-Richter distribution of the earthquake catalogue determined from the SeaJade dataset. The best-fit is shown with a dashed red line. The a-value, b-value, magnitude of completeness (M_C), and corresponding standard deviations (σ) are given in the upper-left box. σ for each parameter was found by bootstrapping the MBASS method (Amorèse, 2007) over 1,000 iterations.

To determine the resolution of our tomography model, we performed checkerboard tests, which are shown in Figure 2.5 and Figure 2.6 are detailed in Section 2.7.3.

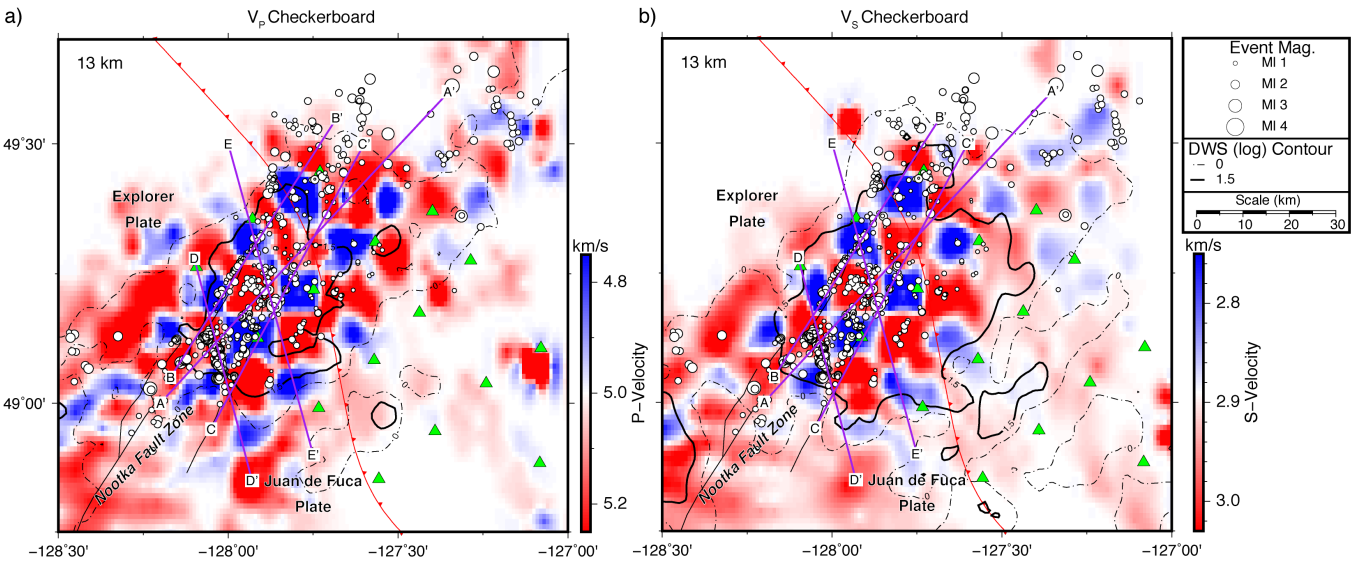

Figure 2.5. Maps showing the results of synthetic checkerboard tests at 10-km resolution for a) V_P, and b) V_S. OBS locations are identical to the SeaJade deployment, as marked by green triangles. Earthquake hypocenters appear as white-filled circles. The checkerboard squares are well-resolved in the Nootka fault zone region, especially where earthquake activity is most concentrated. The log10 solution for DWS value distribution is shown by black contours (thin dashed lines and thick solid lines correspond to the contours of 0 and 1.5, respectively). The best-resolved areas, with higher DWS values, indicate where the seismic tomography model has reasonable results and can be further discussed.

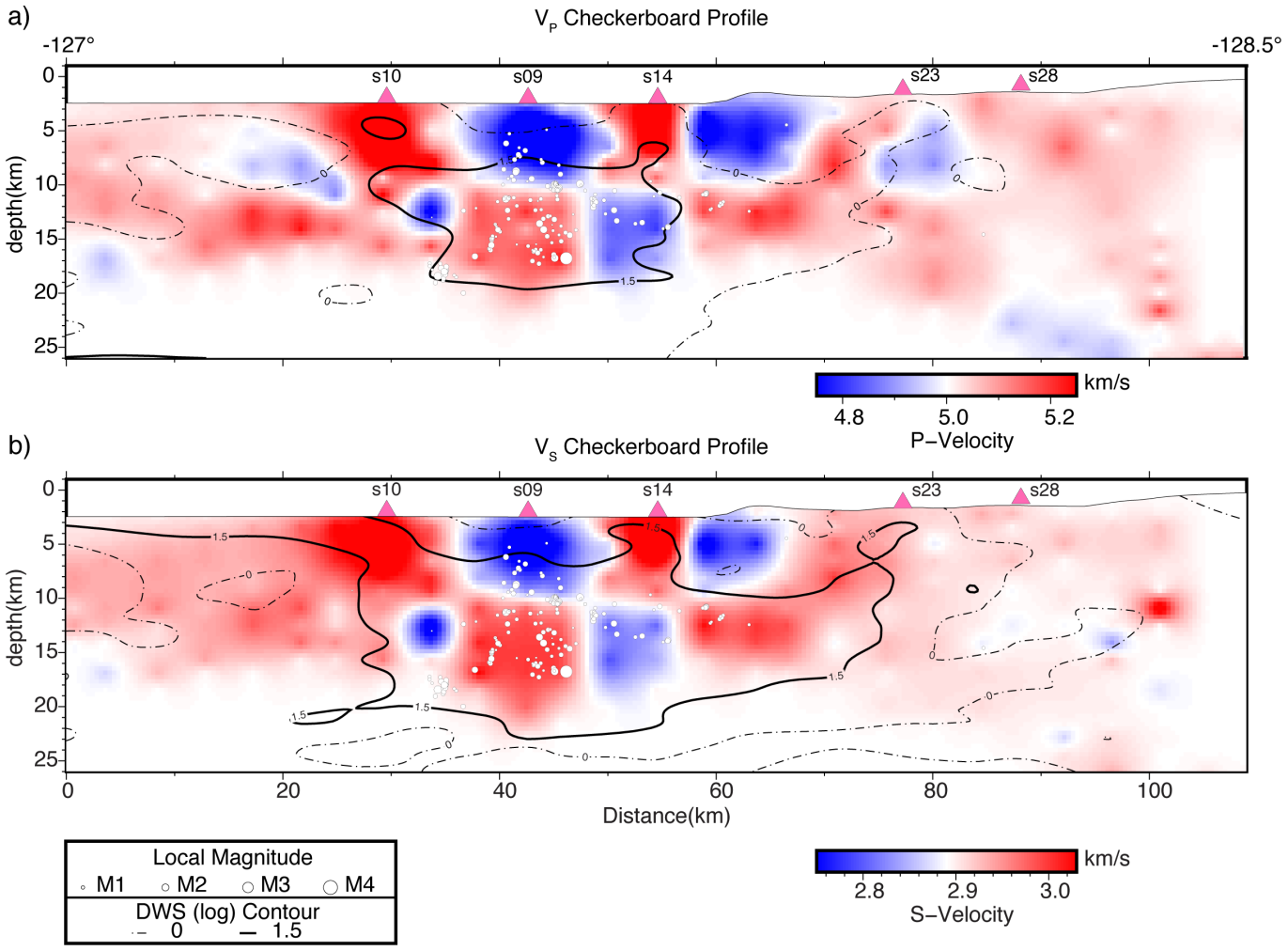

Figure 2.6. Representative cross-sections of the synthetic checkerboard test results shown in Figure 2.5 (at 49° 12'N, running from 128° 30'W to 127°W) for a) V_P, b) V_S. Locations of OBS stations are marked by the pink triangles resting on the seafloor. Earthquake hypocenters within five kilometers to either side of this cross-section appear as filled white circles. The checkerboard grid is best resolved beneath stations s10, s09, and s14, and where the concentration of earthquakes is highest. The log10 solution for DWS value distribution is shown by black contours.

From our initial locations, we systematically examined waveforms with near-vertical incident angles to look for converted phases (Ps or Sp) that could constrain the depths of velocity-contrasting interfaces. To identify Sp phases, we looked for the highest amplitude signals on the vertical channel between the P and S phases; Ps phases were identified by finding the highest amplitude signals on the horizontal channels. For certain events, we were able to identify matching converted phases at more distant stations. In order to account for greater epicentral distances and due to the shift in many event locations by TomoDD, we utilized the TauP package (Buland and Chapman, 1983; Crotwell et al., 1999) to calculate raypaths for the

relevant phases, as adapted for Obspy (Krischer et al., 2015; Megies et al., 2011; Wassermann et al., 2010). A total of 476 converted phases (187 Ps and 289 Sp) were identified with the differential travel times (Ps-P or S-Sp) ranging from 0.1 to 3.3 s. For any phases associated with events not relocated by TomoDD, we used the original catalogue (Figure 2.2). For each converted phase, the depth (Z_{Total}) to the corresponding velocity-contrasting interfaces was determined by mapping the travel-time difference to a distance with the 1-D velocity model derived from 3-D tomography. Specifically, the travel-time difference associated with a given layer (k) was determined as:

$$dt_{(k)} = D_{(k)}/V_{S(k)} - D_{(k)}/V_{P(k)} \qquad (1)$$

where $D_{(k)}$, $V_{P(k)}$ and $V_{s(k)}$ are the distance (given the incident angle of the raypath), velocities of the P and S phases within layer k, respectively.

Then, Z_{Total} was derived as the summation of the vertical components of D_k where θ is the incident angle:

$$Z_{Total} = \sum_{k=0}^{n} sin\theta D_k \qquad (2)$$

such that the number n satisfies the following condition:

$$t1 - t2 = \sum_{k=0}^{n} dt_{(k)} \qquad (3)$$

where $t1$ and $t2$ are the arrival times of the Ps and P phases, respectively (in the case of P-to-S conversion) or S and Sp phases, respectively (in the case of S-to-P conversion). Notice that the thickness of the deepest layer (n) should be the distance between the hypocenter and the nearest velocity interface above.

For each station, the number of interfaces and their average depths were found by analyzing the modal distribution.

Finally, we determined focal mechanisms for earthquakes that had eight or more P arrivals with identifiable first motions (also see Appendix B). The computer program HASH, which computes

the most probable solution from a set of satisfactory mechanisms (Hardebeck and Shearer, 2002), was used to determine the focal mechanisms for 304 events. The best solutions are listed in Table 2.3. Event-station azimuth and takeoff angles were calculated via the 1-D ray-tracing HASH subroutine from the relocated hypocenters with the original 1-D velocity model (Spence et al., 1985). S/P amplitude ratios were used in addition to P arrival first motions in order to further constrain the fault plane solutions (Hardebeck and Shearer, 2003). Unless waveforms were contaminated by strong low frequency noise, we determined first motions from unfiltered data. Amplitudes were measured from waveforms filtered with a 1 Hz high-pass Butterworth filter.

Table 2.3. Focal mechanism solutions for selected events from the SeaJade earthquake catalogue.

Orid	Date	Mag.	Lat.	Lon.	Depth	S.	D.	R.	FP Uncert.	AUX Uncert.	Rank	Prob.	Type
567	2010:7:29:18:20:43.21	3.1	49.03	-128.23	14.03	203	28	-95	20	18	A	98	N
315	2010:7:22:5:44:16.69	2.7	49.12	-128.08	11.43	171	58	173	26	21	A	92	S
281	2010:7:22:3:20:40.73	2.3	49.13	-128.06	10.44	305	70	175	23	24	A	91	S
687	2010:8:8:14:38:27.23	2.8	49.52	-127.53	23.48	197	87	-159	18	25	A	91	S
479	2010:7:23:21:16:27.77	2.1	49.13	-128.06	9.59	280	46	167	11	20	A	100	S
800	2010:8:18:13:1:38.99	3.3	49.10	-128.52	12.95	205	23	-80	26	28	B	79	N
11	2010:7:6:1:59:9.67	2.7	49.08	-128.14	10.34	168	16	-79	28	28	B	77	N
873	2010:8:24:14:7:3.44	3.3	49.61	-127.34	27.53	188	63	-177	20	33	B	76	S
30	2010:7:6:15:10:2.64	2.4	49.05	-128.03	9.81	157	69	178	30	30	B	75	S
155	2010:7:15:3:27:52.42	2.4	49.62	-127.58	27.32	191	32	-164	19	36	B	71	N
362	2010:7:22:7:6:10.78	2.9	49.12	-128.07	11.15	315	63	149	41	25	B	69	S
462	2010:7:23:11:13:50.66	2.6	49.13	-128.06	9.74	134	58	175	37	25	B	69	S
666	2010:8:7:4:13:31.39	1.9	49.45	-127.87	19.18	209	46	64	27	37	B	69	T
375	2010:7:22:7:54:32.88	2.7	49.13	-128.06	10.06	345	80	123	36	31	B	64	T
883	2010:8:25:17:21:51.77	2.3	49.08	-128.03	10.67	185	51	-176	36	27	B	64	S
132	2010:7:12:12:29:57.06	2.4	49.10	-127.95	10.58	117	89	143	27	31	B	61	S
237	2010:7:20:12:24:46.58	2.2	49.05	-128.02	8.07	154	18	118	39	40	C	74	T
278	2010:7:22:2:34:11.85	1.6	49.13	-128.07	11.05	287	64	121	39	33	C	63	T
1259	2010:9:26:19:27:52.1	3.5	49.19	-127.86	16.78	172	74	-175	36	35	C	62	S
80	2010:7:9:16:1:34.74	2.9	49.42	-127.87	15.08	289	85	-163	39	31	C	60	S
1106	2010:9:10:23:54:10.44	2.6	49.64	-127.22	33.17	313	81	106	36	35	C	57	T
156	2010:7:15:4:16:55.77	2.2	49.15	-128.54	16.18	16	51	-69	38	39	C	55	N
653	2010:8:5:10:17:16.14	2.1	49.46	-127.53	22.86	331	89	-180	34	42	C	55	S
1003	2010:9:3:19:28:24.6	1.9	49.05	-128.09	13.05	141	64	-159	35	41	C	55	S

1088	2010:9:10:3:26:5.21	1.8	49.17	-127.96	15.56	36	66	-128	42	36	C	55	N
1137	2010:9:13:6:49:27.38	2.7	49.36	-127.31	13.09	123	66	106	42	33	C	55	T
926	2010:8:30:2:30:3.68	2	49.07	-128.03	10.24	354	63	110	39	33	C	54	T
1230	2010:9:22:15:52:2.21	2	49.22	-127.89	14.13	269	65	163	32	43	C	54	S
822	2010:8:19:23:52:34.52	1.6	49.05	-127.98	15.28	37	39	68	35	42	C	53	T
19	2010:7:6:10:22:48.57	2.7	49.05	-128.03	9.82	168	78	-162	39	38	C	52	S
159	2010:7:15:4:47:28.24	1.7	49.20	-127.86	14.64	318	78	-111	41	37	C	52	N
364	2010:7:22:7:29:40.83	3.2	49.13	-128.06	9.99	321	62	116	39	35	C	52	T
288	2010:7:22:3:27:13.69	2.2	49.12	-128.06	10.51	319	76	-145	39	43	C	51	S
983	2010:9:3:0:14:10.67	2.1	49.08	-128.13	10.24	191	23	-81	40	37	C	51	N
1050	2010:9:7:11:53:13.71	1.7	49.27	-127.96	19.46	105	62	-172	36	39	C	51	S
446	2010:7:22:22:46:26.66	2.4	49.13	-128.06	11.11	329	72	145	44	34	C	50	S
689	2010:8:8:19:23:35.4	2.2	49.55	-127.61	23.68	5	84	148	34	38	C	50	S

The data is organized by event ID (Orid), Date (YR:MN:DY:HR:MN:SC), Magnitude (ML), Latitude (degrees), Longitude (degrees), Depth (km), focal plane Azimuth (degrees), focal plane Dip (degrees), focal plane Rake (degrees), Fault Plane uncertainty (degrees), Auxiliary Plane uncertainty (degrees), Rank, probability of the mechanism being close to the solution (Prob. %), and Type (S – Strike-slip, N – Normal, T – Thrust).

2.5 Results

2.5.1 Three-Dimensional Distribution of Relocated Seismicity

Based on the distribution and geometry of the resultant 1,052 relocated hypocenters, we have identified a number of seismic features of the Nootka fault zone. As discussed in greater detail below, a total of 8 groups are identified (Figures 2.3 and 2.7): the northern primary lineation (E1), southern primary lineation (E2), secondary lineation one (E3), secondary lineation two (E4), secondary lineation three (E5), diffuse Explorer plate earthquakes (E6), diffuse Juan de Fuca plate earthquakes (E7), and diffuse subducted earthquakes (E8). Details for each lineation, including trend, length, width, the number of associated events, range of depths of earthquakes, and the range of magnitudes of earthquakes, are presented in Table 2.4. We provide depths relative to sea level for better accuracy, as the seafloor varies significantly in depth across our study area. Depth distributions for each group are shown in Figure 2.8.

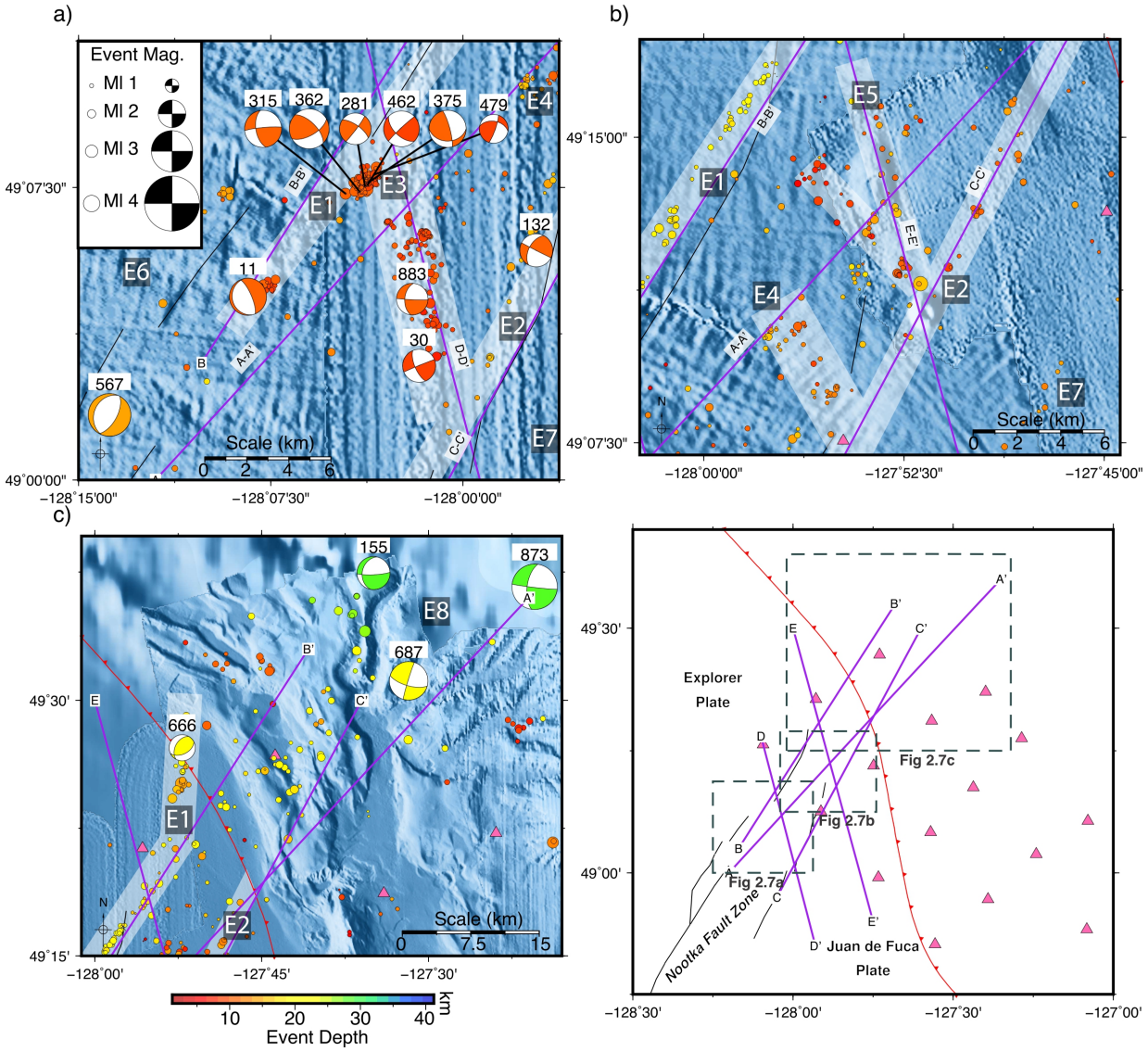

Figure 2.7. Detailed maps showing seismogenic structures and earthquake source characteristics of our study area. Locations of each map are shown in the bottom-right: a) northern primary lineation (E1), southern primary lineation (E2), and secondary lineation one (E3); b) northern primary lineation (E1), southern primary lineation (E2), and secondary lineation three (E5); c) northern primary lineation (E1), southern primary lineation (E2), and events landward of the Cascadia subduction front (E8). Note that each map is at a different scale. Focal depths are indicated by colour and size is indicative of magnitude. The translucent white bands are the approximate areas of the labeled lineations (E1 – E5).

Table 2.4. Hypocenter lineations/zones and associated attributes.

Lineation/Zone	Trend	Dip	Lineation Length (km)	Lineation Width (km)	No. Events[4]	EQ Depth Range (km)	EQ Magnitude Range (M_L)
E1[1]	N28°E±0.3° / N15°E±3°	76°±1° NW/62°±5 NW	55 / 15[1]	1 / 2.5[1]	172	6-22	0.1-3.1
E2	N32°E±1°	78°±5° SE	45	1.5	75	8-17	0.5-3.5
E3	N30°W±1°	42°±2° SW	15	2.5	319	6-14	0.0-3.2
E4	N41°W±4°	45°±3° SW	8	2.5	35	9-16	0.5-2.1
E5 East Splay[2]	N22°W±5°	77°±9° W	18	1.4	53	11-15	0.5-3.5
E5 West Splay[2]	N50°W±4°	46°±6° NE	14	1.5	24	6-11	0.5-3.5
E6[3]	-		-	-	149	6-22	1.2-3.9
E7[3]	-		-	-	33	6-15	0.7-1.9
E8[3]	-		-	-	116	3-34	0.5-3.3

[1] Approximately 10 km landward of the subduction front, E1 appears to change direction. The trend, lineation length, and lineation width are shown in the table after the "/".

[2] E5 splays in two directions from the south. The details are summarized as separate entries.

[3] E6, E7, and E8 are diffuse zones containing seismicity, and are without specific lineation trends, lengths, or widths.

[4] The number of events do not match the total number of earthquakes in the dataset due to the exclusion of certain hypocenters from lineations. Some events may also be associated with more than one lineation (e.g. the cluster of events at the junction of E1 and E3).

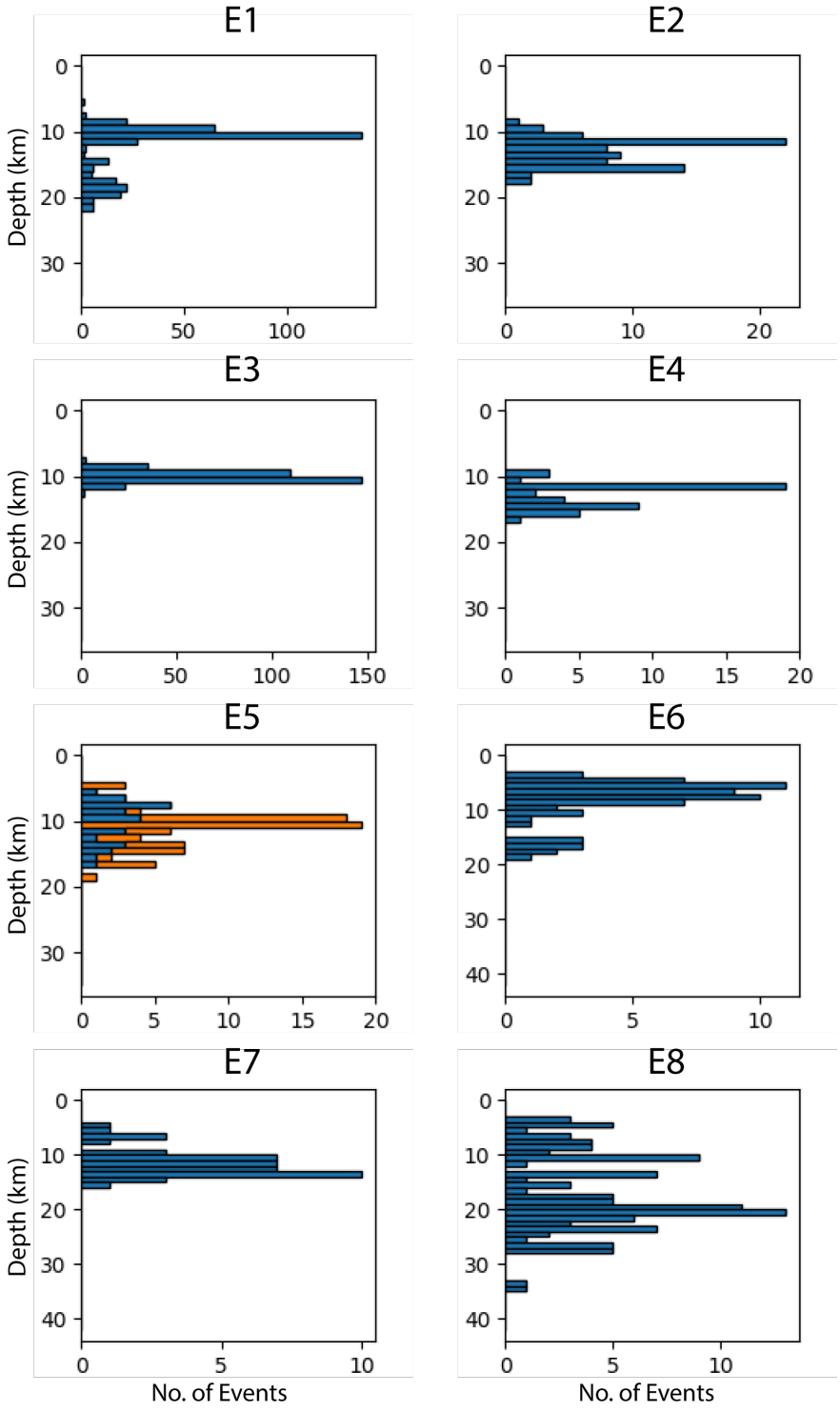

Figure 2.8. Depth distribution (below sea level) of relocated earthquakes within groups E1-E8. For E5, the orange and blue bins correspond to hypocenters belonging to the east and west splays, respectively.

The northern primary lineation (E1) features tightly clustered hypocenters which trend NE with a width of ~1 km. Ten km seaward of the subduction front (Figures 2.3 and 2.7b), the

hypocenters of E1 trend further northward before reaching the front. The southern primary lineation (E2) is less tightly clustered than E1, however, it is still well-defined with a width of ~1.5 km. The highest magnitude event within the Nootka fault zone (M_L 3.5) occurred along E2, 25 km from the southwestern end, on 17 September 2010.

Between the northern and southern primary lineations, there are several secondary lineations subperpendicular to the trend of the Nootka fault zone as defined by E1 and E2. E3 is the best defined of the secondary lineations with a width of ~2.5 km, clearly spanning approximately 15 km between the northern and southern primary lineations (Figures 2.3 and 2.7a). During the study, a seismic swarm on E3 began on 22 July 2010. The swarm had 175 earthquakes during the first day, followed by 29 more earthquakes on the second day. The majority of the events in this swarm were located within a square-kilometer area centered at 128°04'W, 49°07'N with depths ranging from 6 to 14 km. A consistent change in event location over time was not observed. E4 is a less well defined, shorter lineation with a width of ~2.5 km that follows nearly the same azimuthal trend as E3 (Figure 2.7b). E5 begins along the southern primary fault at approximately the same junction as the epicenter of the M_L 3.5 event, and seemingly splays in two directions (Figures 2.3 and 2.7b), each with a width of ~1.5 km.

The earthquake groups E6, E7, and E8 represent areas outside of the Nootka fault zone; respectively, they are within the Explorer plate, within the Juan de Fuca plate, and within the Nootka fault zone landward of the subduction front. Events occurring within E6, west of the Nootka fault zone, were located but are less well-defined as a cluster because they were outside of and far away from the OBS network with large uncertainties (Figure 2.3). Within E7, several events follow a similar trend to E2, but are less tightly clustered. Despite the ample station coverage to the south, no earthquakes were detected within the subducted portion of E7 (Figure 2.3), further corroborating observations of a lack of seismicity along most of the interplate thrust zone (Tréhu et al., 2015; Wang and Tréhu, 2016; Williams et al., 2011). After subduction of the Explorer/Juan de Fuca plates, the lineations and trends made apparent by earthquakes within the Nootka fault zone are less evident (E8, Figures 2.3 and 2.7c). Events along the same trend as the Nootka fault zone continue to deepen away from subduction front,

with few events shallower than 15 km. There are no features correlative to the secondary lineations within the Nootka fault zone (i.e. E3, E4, and E5) within the subducted Explorer/Juan de Fuca plates.

As a whole, the seismic behaviour of the Nootka fault zone can be defined by the *b*-value obtained from the MBASS test (Amorèse, 2007). The *b*-value of 1.07 (Figure 2.4) is quite similar to what has been observed within the creeping segments of San Andreas fault (e.g. 1.1-1.6; Wyss et al., 2004) and at many of the world's mid-ocean ridge segments (e.g. 0.86-1.19; Bayrak et al., 2002). *b*-values higher than 1 indicate atypical tectonic behaviour, with abundant low-magnitude earthquakes. Due to the limited duration of the SeaJade deployment, we cannot compare the *a*-value (an indicator of overall seismic activity) to regions with longer observations.

2.5.2 Tomography

In this section, we present the final 3-D velocity model produced via TomoDD inversion. On the basis of our checkerboard test (Figure 2.5 and Figure 2.6), tomography results for depths shallower than 5 km below sea level should be considered less reliable due to insufficient data resolution, and velocity anomalies smaller than 10 km across are not well resolved. With these limitations in mind, we shall describe the results within slices at several depths (Figure 2.9a) as well as along various profiles (Figure 2.11) crossing areas with the highest resolution. The tomography diagrams present hypocenters within +/- 1 km of the depth of the slice, as well as contours for low and high velocity anomalies. Velocity anomalies were identified as regions where velocities exceeded +/- 2% of the average background velocity for each tomography slice. DWS contours marking areas with the most concentrated raypath coverage are shown for each tomography slice and profile (Figures 2.10, 2.12, and 2.13) and V_P/V_S ratios are shown in Figure 2.9b.

a)

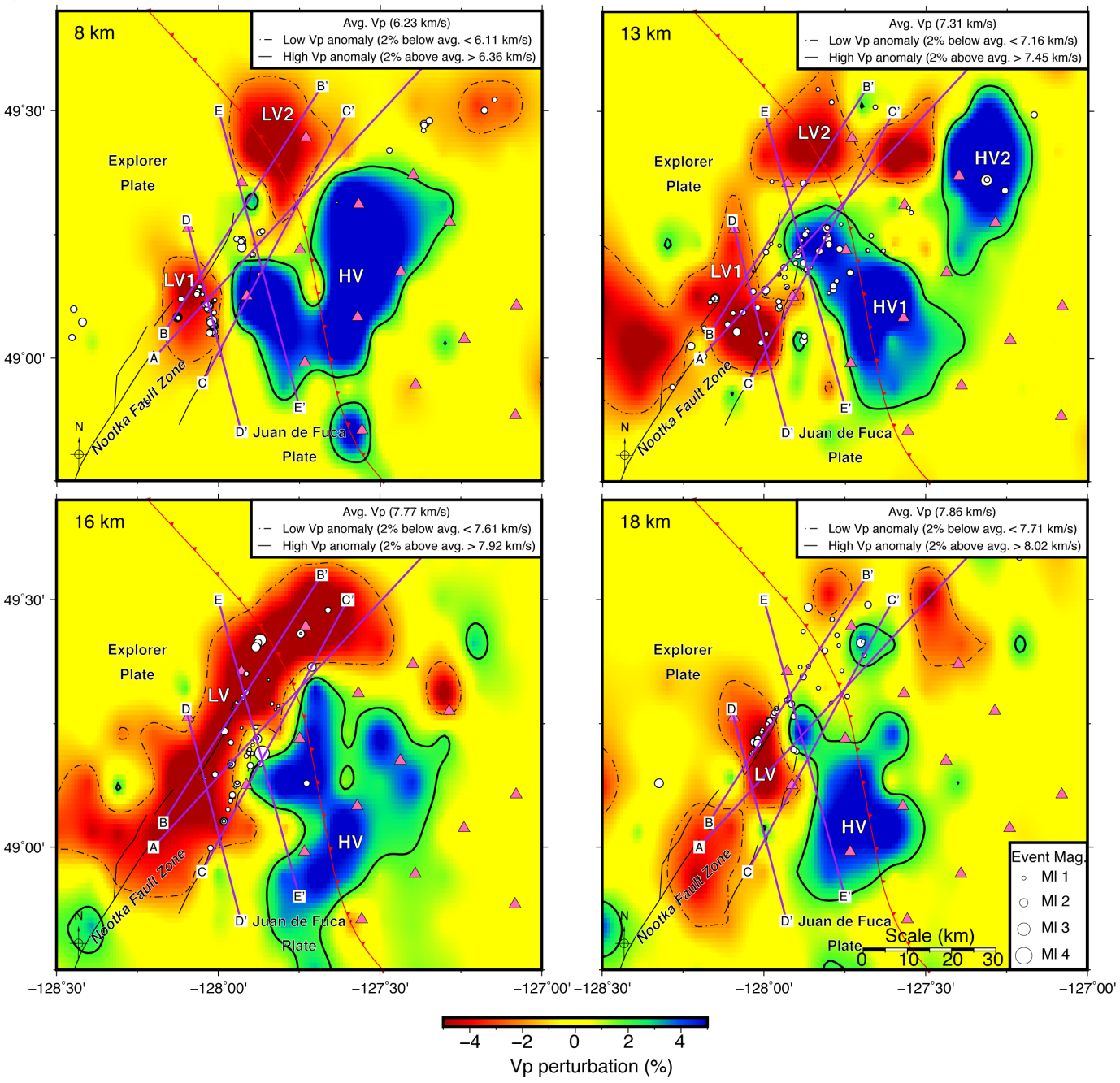
8 km
Avg. Vp (6.23 km/s)
Low Vp anomaly (2% below avg. < 6.11 km/s)
High Vp anomaly (2% above avg. > 6.36 km/s)
LV2
HV
LV1
Explorer Plate
Nootka Fault Zone
Juan de Fuca Plate
13 km
Avg. Vp (7.31 km/s)
Low Vp anomaly (2% below avg. < 7.16 km/s)
High Vp anomaly (2% above avg. > 7.45 km/s)
HV2
HV1
16 km
Avg. Vp (7.77 km/s)
Low Vp anomaly (2% below avg. < 7.61 km/s)
High Vp anomaly (2% above avg. > 7.92 km/s)
LV
18 km
Avg. Vp (7.86 km/s)
Low Vp anomaly (2% below avg. < 7.71 km/s)
High Vp anomaly (2% above avg. > 8.02 km/s)
Event Mag.
Ml 1
Ml 2
Ml 3
Ml 4
Scale (km)
0 10 20 30
49°30'
49°00'
−128°30'
−128°00'
−127°30'
−127°00'
−4 −2 0 2 4
Vp perturbation (%)

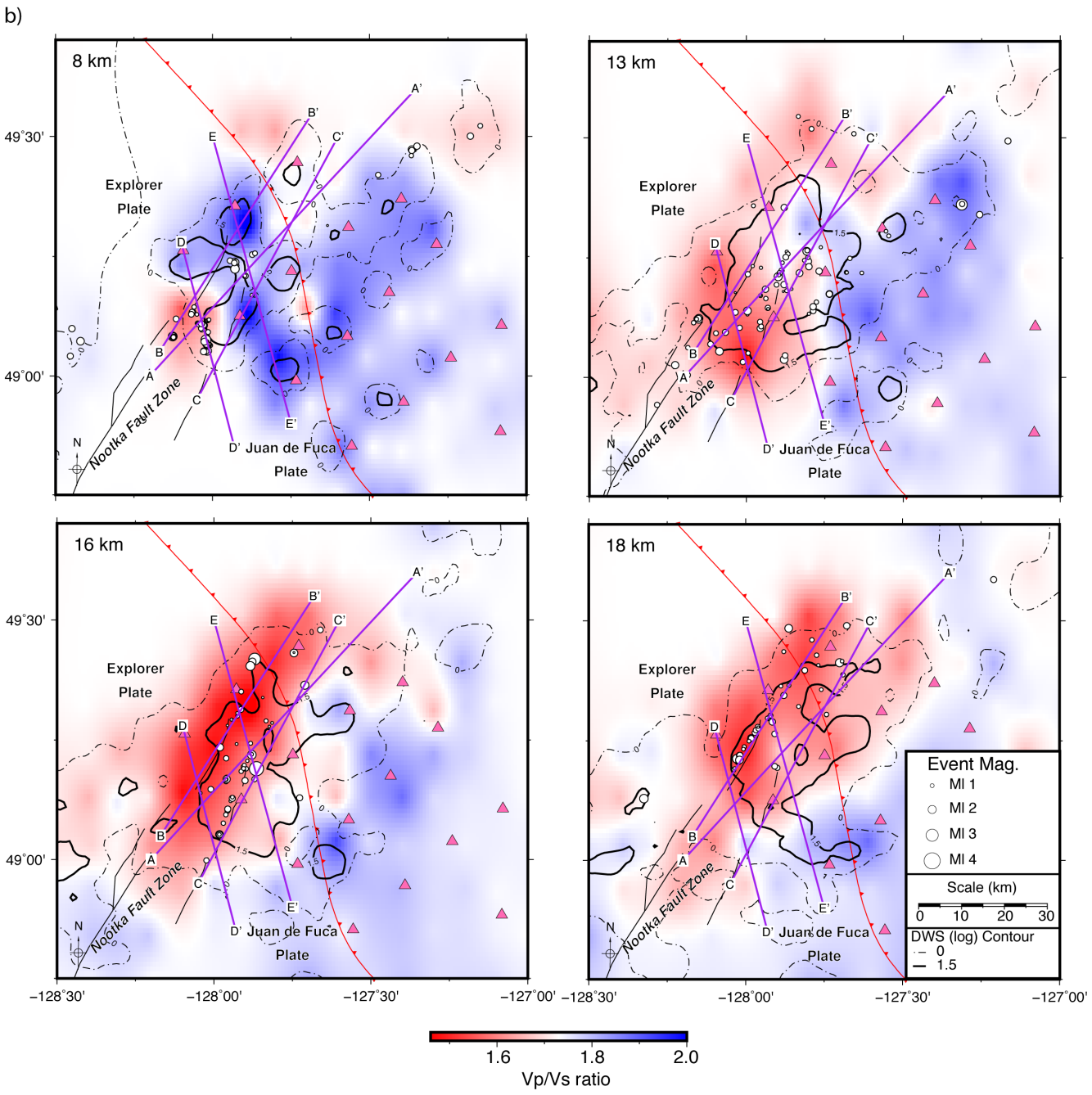

Figure 2.9. Maps showing TomoDD tomography inversion results for a) P-velocity perturbation (%) and b) V_P/V_S ratios at 4 different depths. Earthquakes are marked by white-filled circles. Pink triangles mark the SeaJade OBS locations. The northern and southern trace of the Nootka fault zone are shown as thin black lines and are based on interpretations of bathymetry and active source surveys. The seismic tomography results are horizontal slices through the study area at the depths indicated in the upper-left corner of each map. The earthquakes shown are within 1-km above and below the depth slice. a) P-velocity perturbations from the average velocity for each slice are indicated by colour, with colder colours equivalent to higher velocities. Contours are representative of low and high velocity anomalies, which are 2% greater than or less than the average V_P of the slice (shown in the upper right of each map). High and low velocity anomalies discussed in the text are labelled with HV and LV, respectively. b) V_P/V_S ratios are indicated by colour, with colder colours equivalent to higher V_P/V_S ratios. Raypath densities are represented by DWS contours.

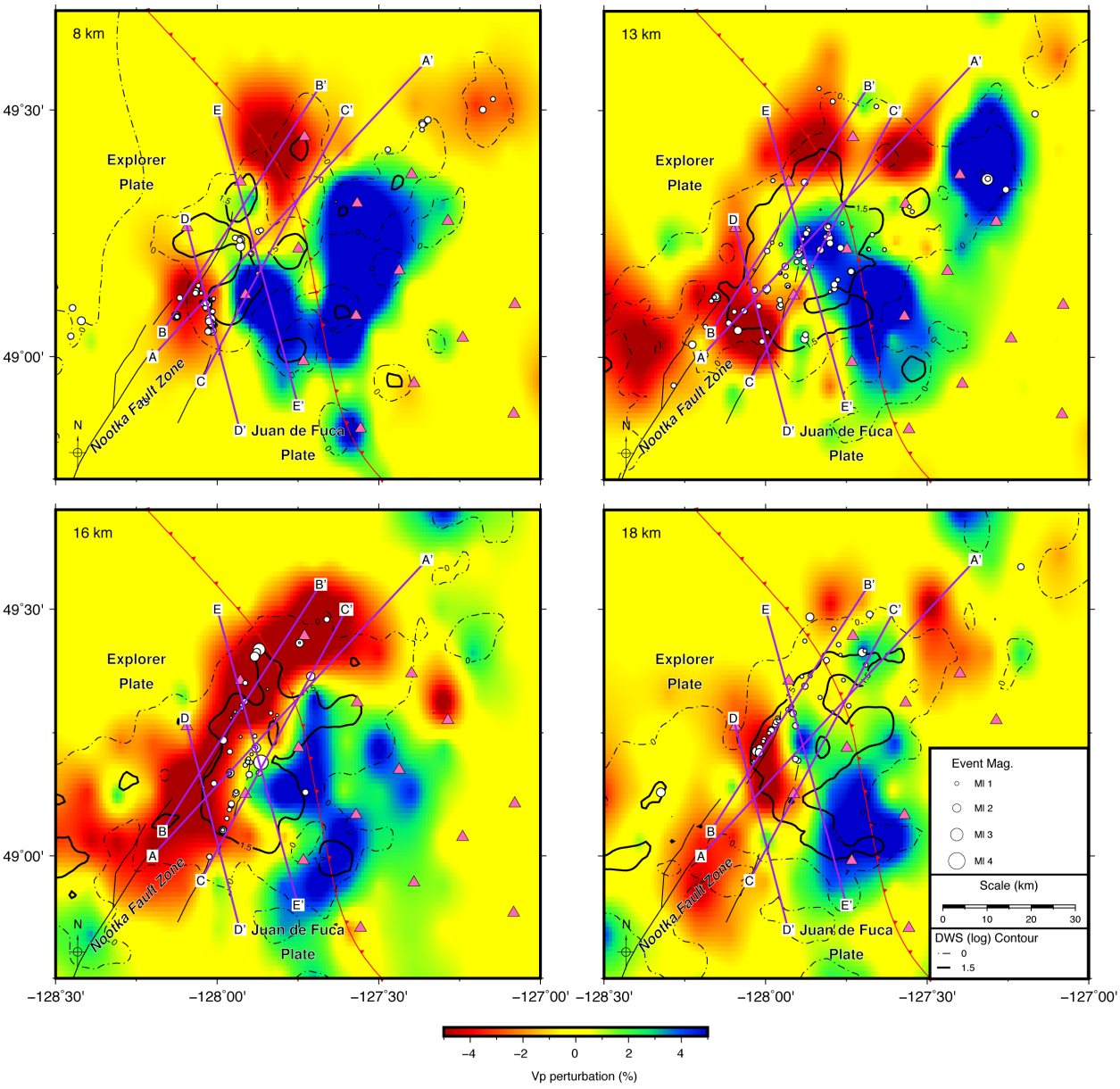

Figure 2.10. Maps showing TomoDD tomography inversion results. Symbols and layout are the same as that in Figure 2.9a, except that the contours represent raypath density.

Tomographic Velocity Anomalies

Within the depths of 8-18 km, low velocity anomalies (labelled as LV, LV1, and LV2 in Figure 2.9a) dominate much of the Nootka fault zone and part of the Explorer plate. In particular, at the depth of 16 km, the Nootka fault zone is almost entirely comprised of LV both landward and seaward of the subduction front. Conversely, the well-resolved portion of the Juan de Fuca plate is mostly comprised of high-velocity anomalies (labelled as HV, HV1, and HV2 in Figure

2.9a). HV appears to intrude into the Nootka fault zone, which is most apparent at the depth of 13 km. Further details regarding the velocity anomalies are provided in Section 2.7.4.

V_P/V_S ratios (Figure 2.9b) show lower than average (1.73) values for much of the Nootka fault zone and the resolvable area of the Explorer plate in the depth range of 13-18 km. At the 8-km depth, the low V_P/V_S ratio is divided by a high V_P/V_S anomaly to the west and east of E-E' for approximately 20 km along the Nootka fault zone. At the depths of 13 km and 16 km, low V_P/V_S ratios extend approximately 15 km south of the Nootka fault zone, west of the subduction front. Without the aforementioned exception, V_P/V_S ratios are consistently higher than average ratios within the Juan de Fuca plate.

Tomography Cross-Sections

Several tomography profiles are shown in Figure 2.11. High and low velocity anomalies are labelled as PHV and PLV1/2/3, respectively. The most prominent anomaly (PHV) is shown on profile A-A', and dips 9-10° toward the northeast from the depth of 12 to 23 km below sea level, at the distance of 30-75 km from point A along the profile. PHV is also visible along profile C-C' and to a lesser extent along profile B-B'. PLV1, located towards the southwestern ends of profile A-A', B-B', and C-C', reaches into higher velocity materials to the depth of nearly 18 km. PLV3, visible in profiles D-D' and E-E', indicates lower velocities to the depth of ~18 km on the Explorer plate side of the Nootka fault zone than on the Juan de Fuca plate side.

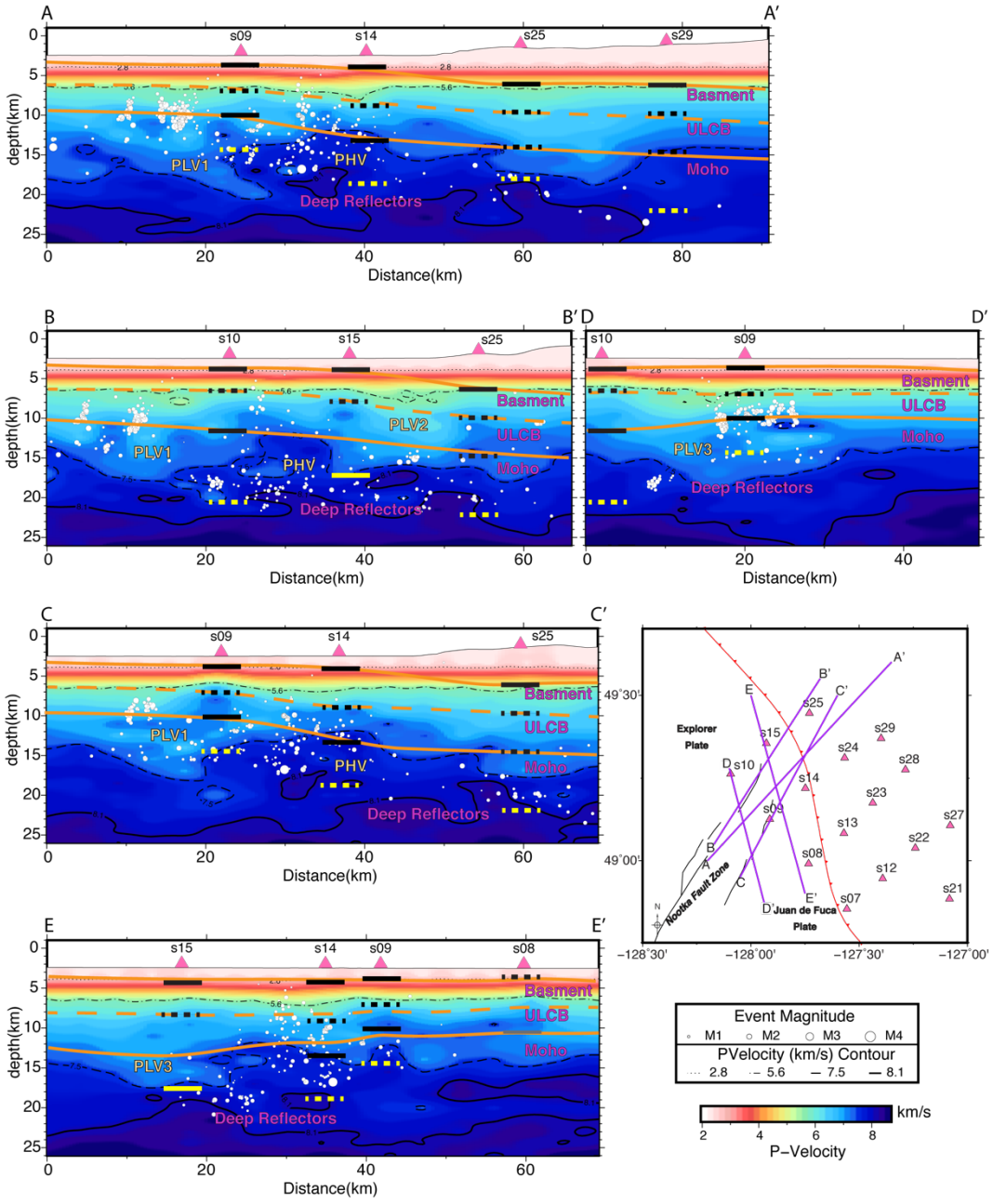

Figure 2.11. Tomographic profiles of the study area. Earthquakes within 5 km to either side of the profiles are projected and marked as white-filled circles, while stations are within 10 km to either side of the profile. Black contours are representative of P velocities for given intervals. The solid and dashed black lines are average depths derived from threshold T2 (high) and threshold T1 (low) converted phase analysis, respectively. Deep reflectors are shown in yellow. Orange lines are representative of our interpreted velocity-contrasting interfaces derived from the converted phase analysis and are labelled with corresponding interpretations. ULCB is short for Upper/Lower Crust Boundary. High and low velocity zones are labelled with PHV and PLV, respectively. A reference map for the study area and the profile lines are shown in the lower right corner.

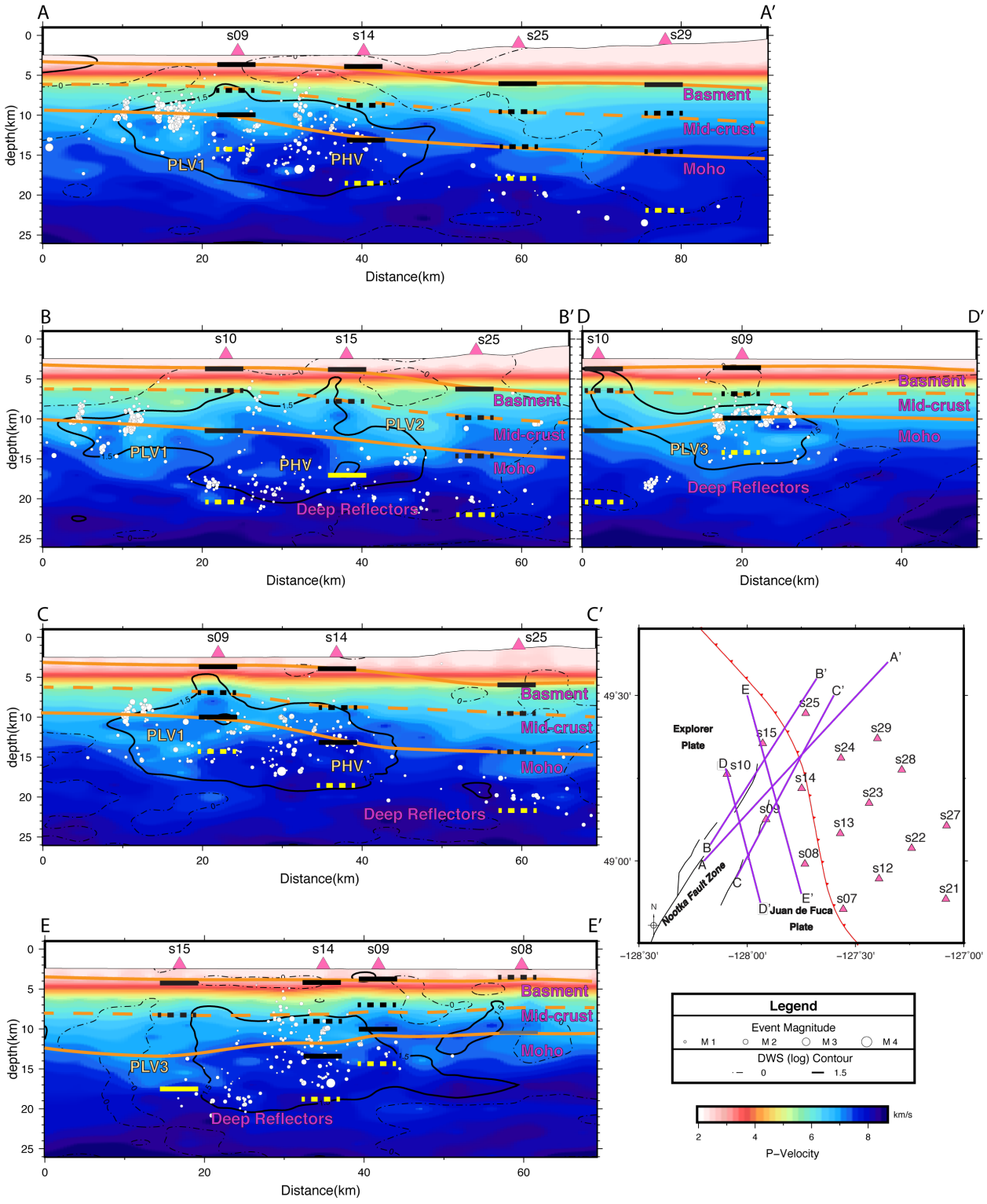

Figure 2.12. Tomographic profiles of the study area. Symbols and layout are the same as that in Figure 2.11 except that the contours represent raypath density.

Additional details of the tomography features in cross-section are provided in Section 2.7.4. We also present three additional profiles perpendicular to the Cascadia margin (F-F') and the Nootka fault zone (H-H' and G-G') in Figure 2.13.

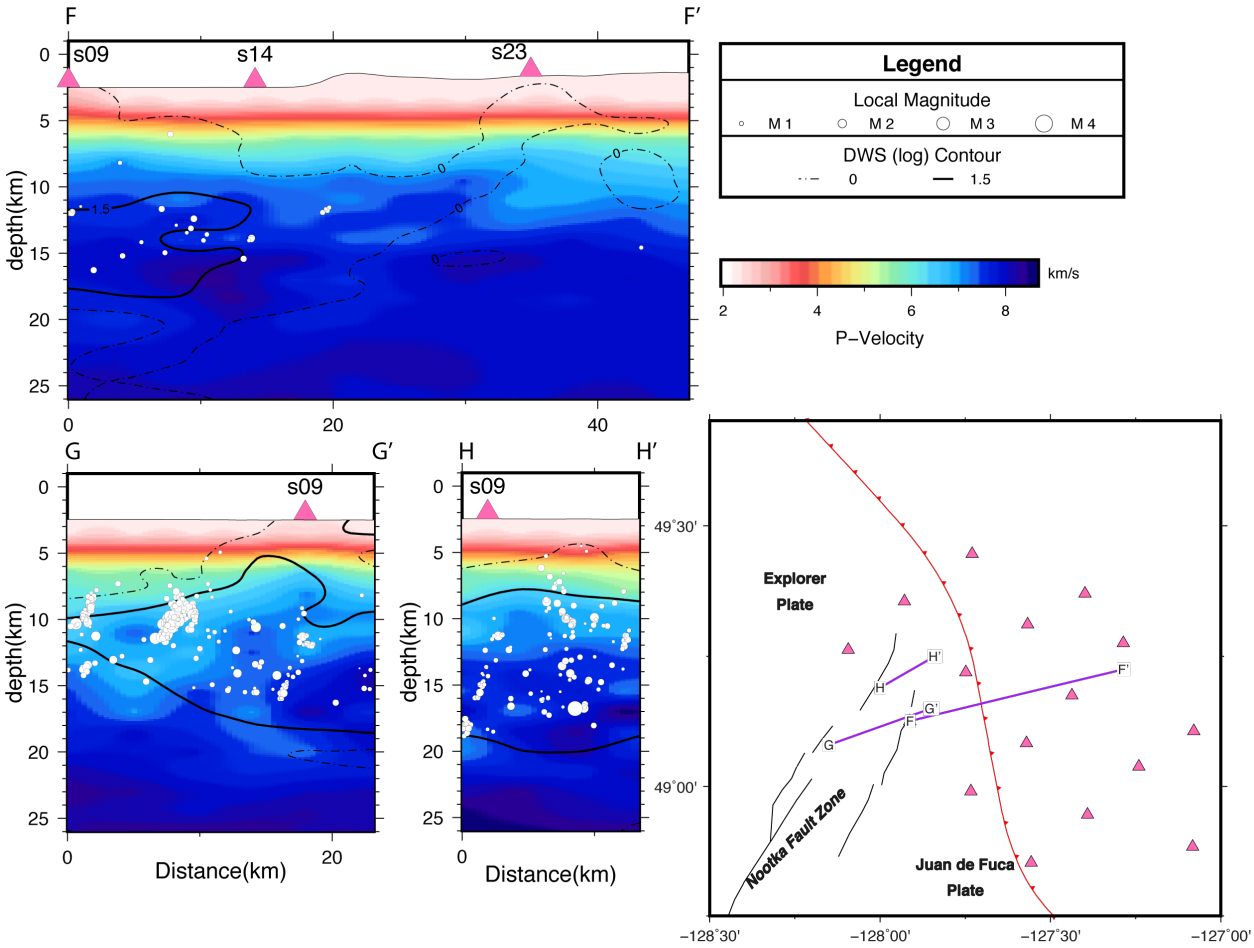

Figure 2.13. Additional tomographic profiles to those shown in Figure 2.12. F-F' runs perpendicular to the Cascadia subduction front within the Juan de Fuca plate. The tomography shows a low-velocity structure (~7 km/s) gradually deepening eastward, analogous to the Moho. It should be noted that raypath density is greatly reduced toward F', although the checkerboard test is still fairly well-resolved. Profile G-G' runs perpendicular to the strike of E3 and E4 and H-H' runs perpendicular to E5. They both provide a better perspective of the dipping fault structures described in the interpretations.

2.5.3 Converted Phases

After detecting converted phases, we utilized the travel-time differences between the converted phases and primary phases (ranging from 0.1 to 3.3 s) to calculate the depths to interfaces with 1-D velocity models derived from the local 3-D seismic tomography. We

compared the results of our local 1-D models to the starting 1-D velocity (Spence et al., 1985) and found an average difference of 1.63 km (ranging from -0.69 to 3.59 km) for a total of 476 converted phases (187 Ps and 289 Sp). Examples of converted phases used for determining the depth to interfaces are shown in Figure 2.14 and their corresponding raypaths are shown in Figure 2.15. Notice that some of the raypaths have a significant horizontal component that may lead to erroneous estimates of the interface depths if nearly vertical paths are assumed. We emphasize that when source-station pairs with comparable epicentral distance and depth must be included in the converted phase analysis (mainly due to the lack of samples such as in our case), contributions from both horizontal and vertical components of the raypaths should be properly accounted for to avoid possible overestimation of the interface depths.

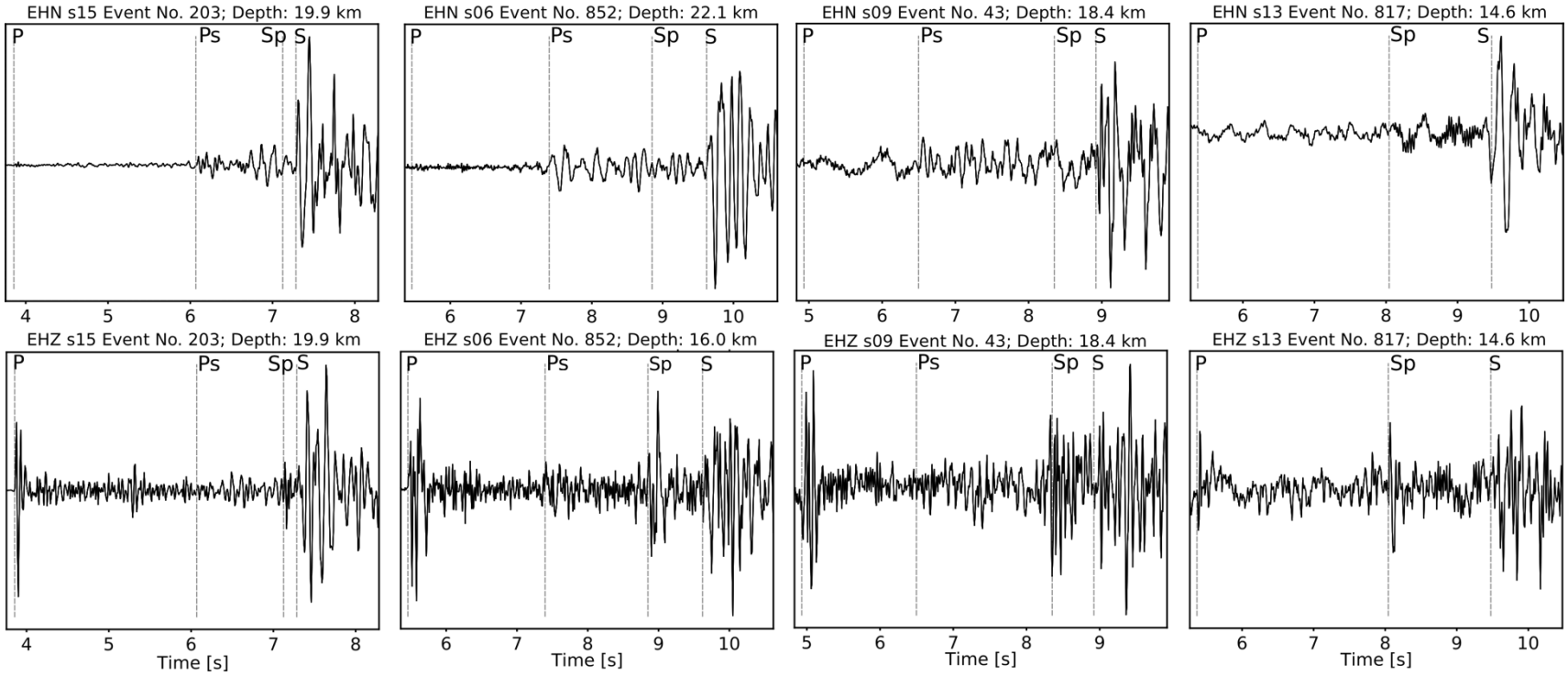

Figure 2.14. Example waveforms showing converted phases used for velocity-contrasting interface calculations. From left to right, the waveforms are organized by the station at which the converted phases were observed, with horizontal channels shown in the top row and vertical channels shown in the bottom row. In order of the stations, depths calculated for each example phase are listed: s15) Sp – 3.0 km, Ps – 15.6 km; s06) Sp – 4.3 km, Ps – 10.0 km; s09) Sp – 4.4 km, Ps – 11.9 km; s13) Sp – 7.7 km.

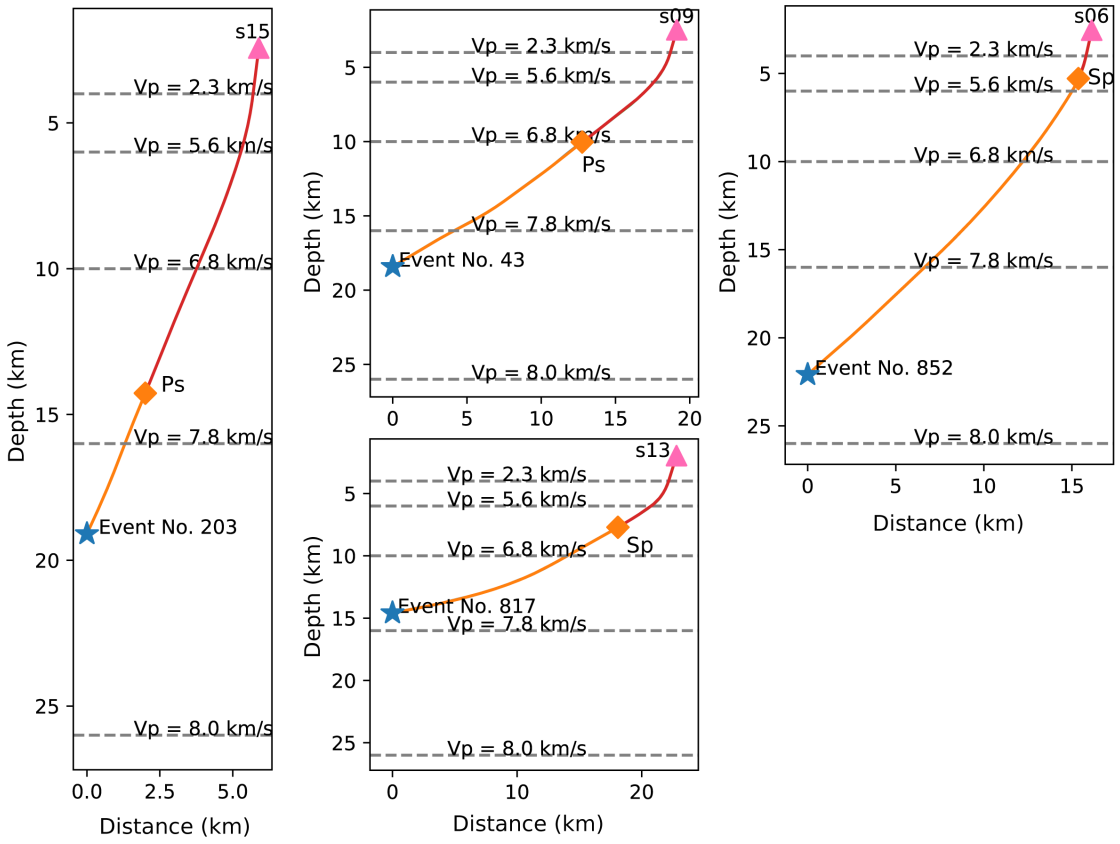

Figure 2.15. Raypaths corresponding to the waveform examples shown in Figure 2.14, as calculated using the ObsPy TauP package. P-wave velocities at the depths of 4, 6, 10, 16, and 26 km (dashed lines) are given for reference. Note that converted phase depths were calculated along the horizontal and vertical components of the raypaths.

We have plotted histograms for the converted phases at each station (Figure 2.16) in order to determine the depth range of each interface throughout the Nootka fault zone region. Stations are organized according to their relative locations shown in Figure 2.1. The derived depths are relative to sea level and are grouped into bins of 1 km intervals. They are classified by whether the number of observations exceeds given thresholds (T1 and T2). Isolated bins with only one count (threshold T1 in Figure 2.16) are not considered in our interpretation. A second threshold of 4 counts per bin (T2) is set to indicate better resolved interfaces (solid lines in Figure 2.16). For stations with many counts per bin, this method allows us to distinguish potential interfaces. Bins with counts fewer than the T2 threshold should still be considered open for discussion, but there are not enough detections to draw any significant conclusions.

For the stacked histograms of the westernmost transect of stations (s10, s09, s08, s06, and s05), several important features were observed. Three high threshold interfaces were detected, with the possibility of a fourth additional interface at a deeper depth. Average depths to these interfaces relative to sea level are 3.7 km, 6.6 km, and 11.1 km. The fourth interface is easier to distinguish on the histogram for s09 at an averaged depth of 14.2 km (Figure 2.16), but is buried by the broad distribution of converted phase depths at s10 in the stacked histogram. The first and third interfaces are, by far, the most pronounced.

The second transect consists of stations s15, s14, and s13. Four interfaces were detected amongst the stacked histograms, at average depths of 4.2 km, 9.0 km, 13.7 km, 17.7. Depending on interpretation, the third and fourth interfaces are difficult to distinguish from one another. We think that the third and fourth interfaces can be differentiated by the decreased number of detections at the 16-17 km depth. The difficulty in distinguishing these interfaces may be in part due to the complex velocity structure described earlier and because this transect of stations crosses the subduction front (Figure 2.11).

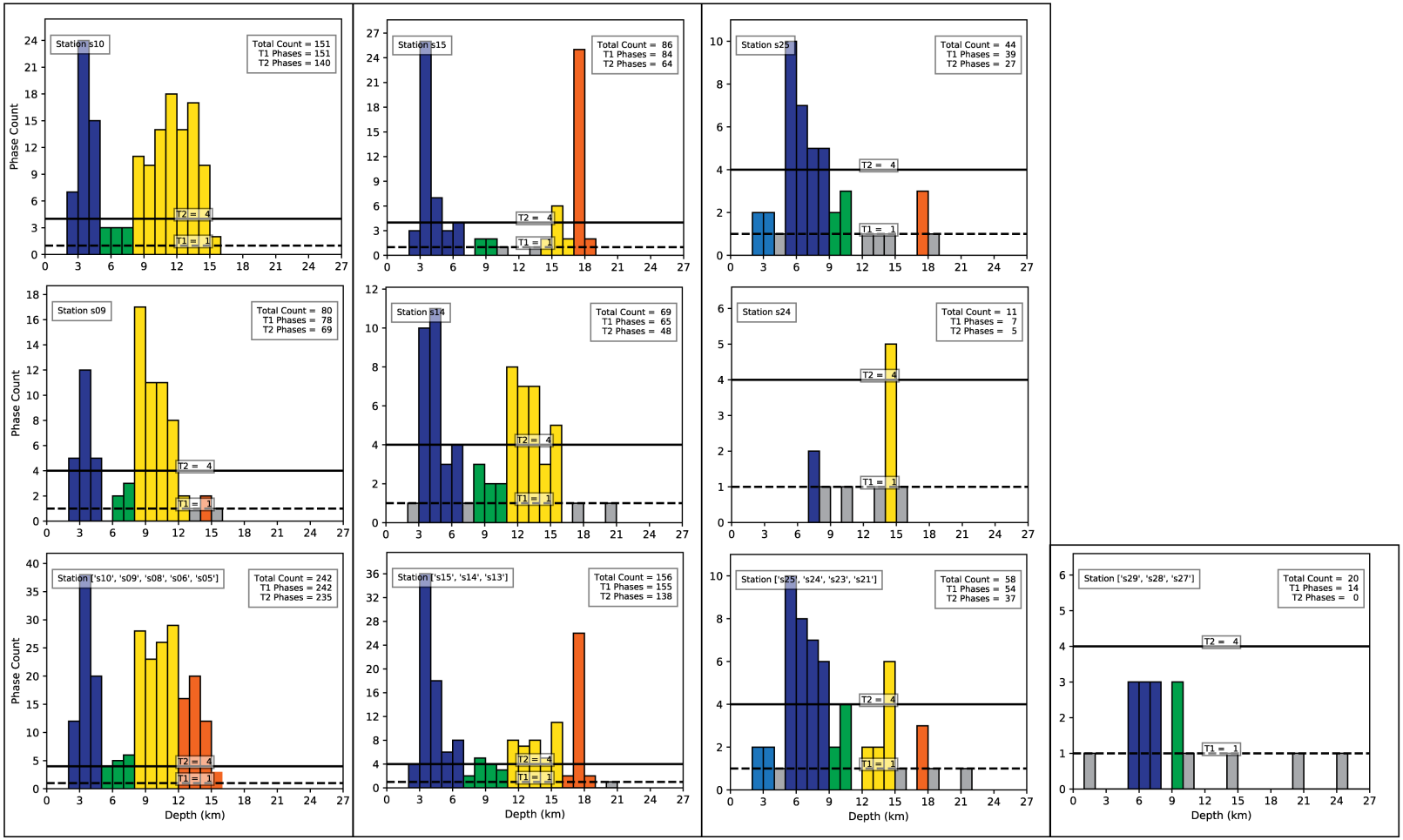

Figure 2.16. Histograms of the depth to interfaces below sea-level detected by converted phase analysis. Histograms are organized by north-south transects of stations, beginning with the westernmost and ending with the easternmost. Only the best results are shown, with the final row representing the cumulative results for each transect. The colour of the histogram bars indicate the associated discontinuities, consistent with those in Table 2.5. Depth is relative to sea level and bins are given in 1 km increments. Stations not shown in this figure are presented in Figure 2.17.

The third transect is comprised of stations s25, s24, s23, and s21. From the stacked histograms for this transect, we have delineated four interfaces. The first interface has an averaged depth of 6.7 km. We have determined the second and third interfaces at the average depths of 10.1 km and 14.0 km although the second is difficult to distinguish from the first. A fourth (lower threshold) interface is found at 17.7 km. We also note that there is an additional shallow interface that seems to appear above the expected depth for the first interface at 3.0 km.

Only the depth to the base of the sedimentary rocks, with an averaged depth of 6.3 km, could be clearly resolved for the easternmost transect, comprised of stations s29, s28, and s27. The second interface is possibly located at an averaged depth of 10.2 km. The amount of converted phase detections at this transect were much lower due to fewer events occurring landward of the subduction front. It should also be noted that converted phases were identified for other depths, which are compiled in Table 2.5 and are shown in Figure 2.17.

Table 2.5. Average discontinuity depths determined from converted phases.

Stations[1]	Discontinuities[2]			
	Sedimentary Basement (km) (Blue)	Upper/Lower Crust Boundary (km) (Green)	Oceanic Moho (km) (Yellow	Altered Mantle (km) (Orange)
s10	3.7 (46)	6.4 (9)	11.7 (96)	-
s09	3.6 (22)	7.2 (5)	9.8 (49)	14.2 (4)
s08	3.6 (2)	-	10.5 (6)	-
s06[3]	-	-	-	-
s05[3]	-	-	-	-
s15	3.9 (43)	9.1 (4)	15.3 (11)	17.8 (27)
s14	4.5 (29)	9.3 (7)	13.2 (30)	-
s13[3]	-	-	-	-
s25	3.0 (4) or 6.6 (27)	10.1 (5)	13.6 (3)	17.7 (4)
s24	7.8 (3)	-	14.3 (7)	-
s23[3]	-	-	-	-
s21[3]	-	-	-	-
s29	6.1 (5)	9.6 (2)	-	-
s28	7.1 (4)	-	-	-
s27[3]	-	-	-	-

[1] Stations are arranged according to transects from north to south, separated by colour on the table (alternating gray and white), and then from seaward to landward.

[2] Interface depths calculated from Ps and Sp converted phases and averaged for each station are listed in km. The number of converted phases used for averaging are provided in parentheses. Discontinuities are labelled with colours corresponding to bins in Figure 2.16.

[3] Stations s05, s06, s13, s21, s23, and s27 only provide up to 1 phase count per bin. No statistics are available for these stations, but the values were used to generate the stacked histograms shown in Figure 2.16.

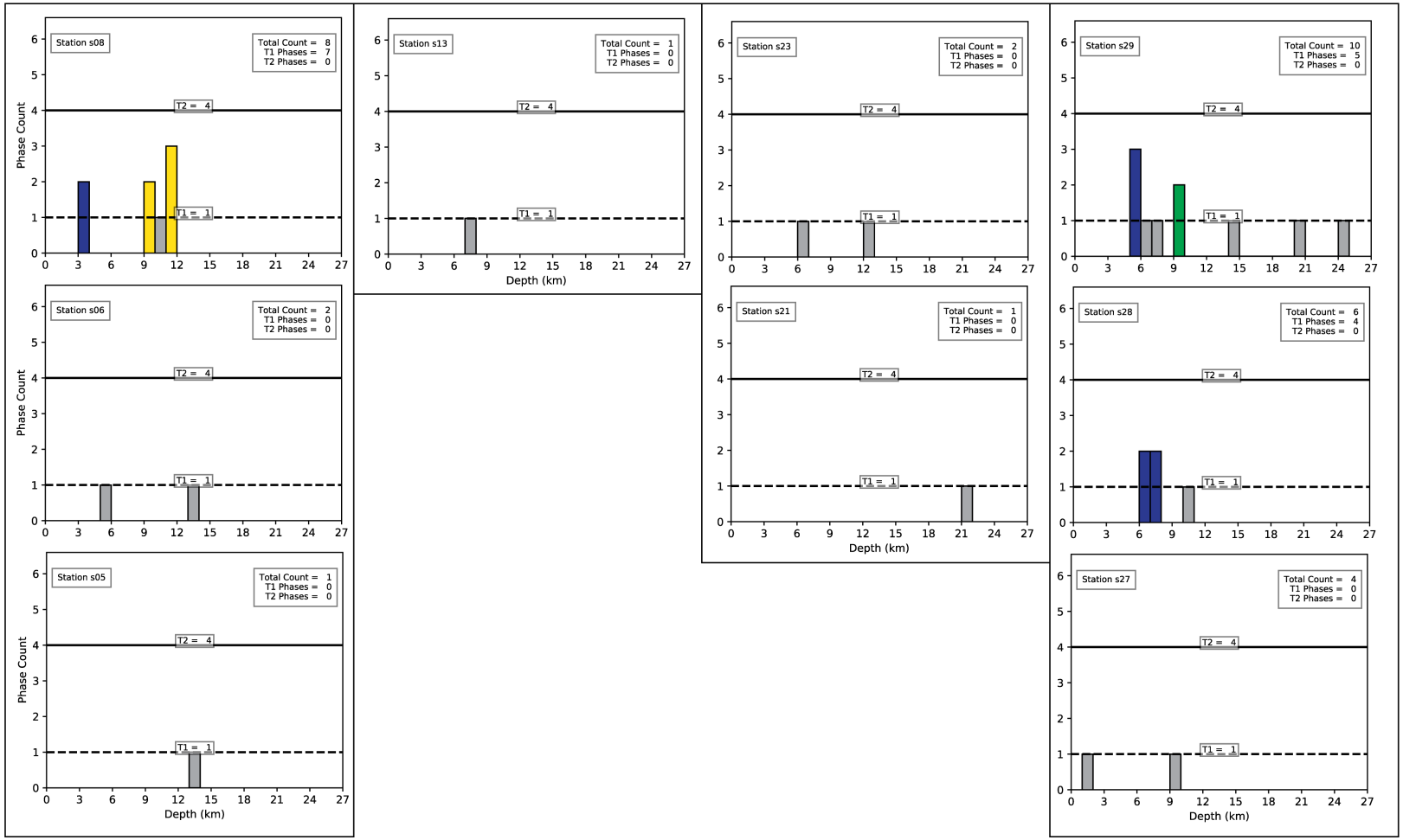

Figure 2.17. Histograms of the depth to interfaces detected by converted phase analysis for stations with the fewest number of detections. Symbols and layout are the same as that in Figure 2.15.

2.5.4 Focal Mechanisms

Of the relocated earthquakes, 304 events had 8 or more P arrival first motions that could be clearly identified and were used in addition to S/P amplitude ratios to generate focal mechanisms. Of those focal mechanisms, 6 were A-ranked, 12 were B-ranked, 22 were C-ranked, and 264 were D-ranked. Two of the mechanisms (1 A-ranked and 1 B-ranked) occurred within the Sovanco fracture zone (SFZ) and are excluded from the discussion. Focal mechanisms using S/P amplitude ratios provided a marked improvement over those calculated purely based on first motion polarity. Before implementation there were no A or B-ranked focal mechanisms, and only 12 C-ranked mechanisms. In this section, we outline the results for the highest-ranked strike-slip, normal, and thrust events to compare with the trend of the hypocenter lineations (Table 2.4). Source parameters of individual events are listed in Table 2.3. Focal mechanisms of A and B-ranked events with first motion polarities are provided in Figure 2.18.

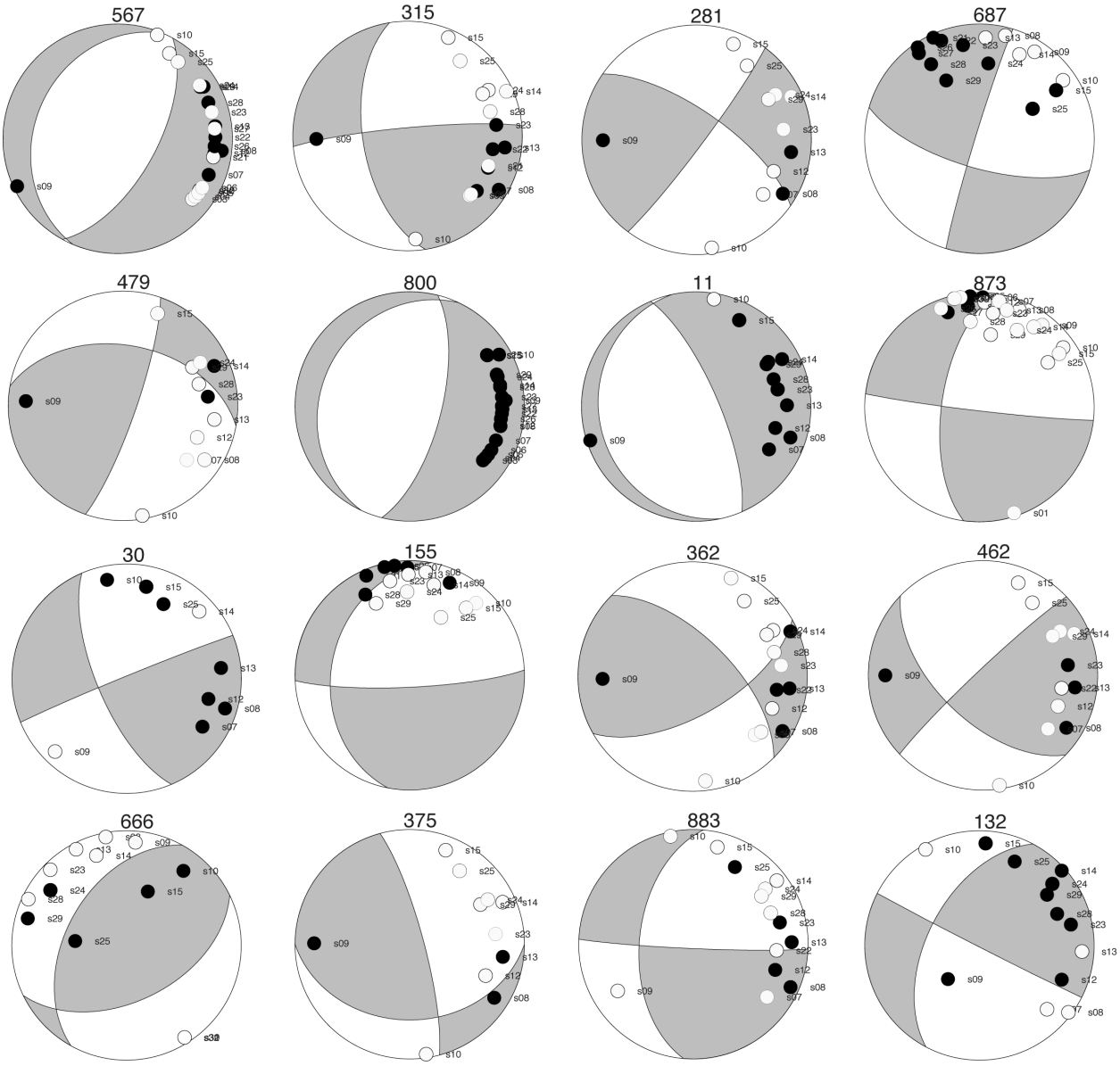

Figure 2.18. Focal mechanisms solutions for the A and B-ranked events shown in Figure 2.7 and Table 2.3. First motion polarities are indicated by filled black (up) and white (down) circles. These solutions are constrained by a combined dataset of P-polarity and S/P amplitude ratios. The amplitude ratio information is not included in the plots.

E1 and E3 can clearly be delineated by their hypocenter distribution, yet the junction between the two (Figure 2.7a) exhibits a complicated behaviour that is difficult to attribute to one lineation or the other. Of the three A-ranked strike-slip events (events No. 315, 281, 479) that occurred in the vicinity of the seismic swarm located near the junction of E1 and E3, we place the greatest confidence in attributing event No. 281 with E1. The fault plane solution of the

left-lateral event No. 281 is best aligned with the trend of the E1 hypocenters (Table 2.4). Two of the B-ranked events (No. 362 and 462) at the E1/E3 junction follow the trend of E1 with left-lateral slip. Past the southwestern extent of E1, event No. 567 has a normal-faulting mechanism (Figure 2.7a). The normal-faulting solution for event No. 11, located within E1, is located 10 km to the northeast of event No. 567. The strike of this solution is 35° from that of event No. 567. Toward the northeastern portion of E1, a thrust event (No. 666) is located within a patch of hypocenters that have a more northerly trend (Figure 2.7c). The corresponding fault plane solution strikes nearly parallel to the trend of the main segment of E1.

Although event No. 315 could be interpreted as part of E1 due to its location, it has an orientation most consistent with the trend of E3 (Table 2.4). Two additional events are attributed with group E3, exhibiting right-lateral motion (events No. 883 and 30, and Figure 2.7a). An oblique slip event (No. 375) was located within the E1/E3 seismic swarm with the strike nearly parallel to the trend of E3 (Figure 2.7a).

Along the lineation of E2, located 8 km east of E3, event No. 132 exhibited left-lateral motion and a strike similar to the trend of E2 (Table 2.4, Figure 2.7a).

Within the subducted segment (E8), several focal mechanisms were observed (Figure 2.7c). An A-ranked strike-slip event within the subducted slab (event No. 687) aligns the compressional axis (P-axis) with the Juan de Fuca plate motion relative to North America. Similarly, the P-axis of the B-ranked event No. 873 is parallel to the Juan de Fuca plate motion with respect to North America. An oblique strike-slip event (No. 155) occurred within the subducted portion of the Nootka fault zone, approximately 10 km northeast of the end of profile B-B'.

2.6 Interpretations and Discussion

2.6.1 Fault Distribution Within the Nootka Fault Zone

We interpret the northern and southern primary lineations (E1 and E2) as steeply dipping major faults that define the northern and southern margins of the Nootka fault zone. The faults are clearly delineated by their hypocenter distribution and can be seen in both map view (Figure

2.7) and in cross-section (D–D', Figure 2.11). Dips were measured from profiles perpendicular to the strike of the faults. Strike/dip error was calculated based on the standard deviation of the least squares fit to each lineation. The strike and dip for each lineation is provided in Table 2.4. Our observations are further supported by a broad agreement with the highest quality focal mechanism solutions.

As expected, the strike-slip focal mechanisms associated with these two primary faults are left-lateral (events No. 281, 362, 462, and 132), indicating a lower convergence rate of the Explorer plate than the Juan de Fuca plate with respect to stable North America. Our interpretations of steeply dipping faults agree closely with those of Rohr et al. (2018), who observed co-incident surface expressions with E1 and E2. There are cases of normal faulting within the Nootka fault zone (events No. 11 and 567; Figure 2.7a), which agrees with the relative plate motion (Braunmiller and Nábělek, 2002).

Based on the linear trend of tightly clustered hypocenters and consistent right-lateral strike-slip focal mechanisms (including C-ranked events for E4 and E5; Table 2.3) for the secondary lineations (E3, E4, and E5; Figure 2.7a and Figure 2.7b), we propose that they are conjugate faults related to the internal fracturing of the Nootka fault zone.

In association with E3, the occurrence of left and right-lateral strike slip faulting during the seismic swarm (on 22 and 23 of July) at the junction of E1 and E3, as well as normal-faulting to the southwest (event No. 11), probably suggests a localized stressed/brittle portion of the Nootka fault zone undergoing oblique extension. The rest of E3 shows primarily right-lateral strike-slip motion. E4 is less well defined than E3 and E5 (Figure 2.7b and Figure 2.16) because it falls short of the northern boundary fault by approximately 8 km and has fewer associated events. E5 consists of two faults that diverge from the southern boundary fault (E2; Figures 2.7b and 2.16). The divergence of E5 correlates with a mud volcano whose bathymetric signature can be easily seen at (49.18° N, 127.87° W) in Figure 2.7b.

Outside of these faults, earthquakes within the Juan de Fuca and Explorer plates are more scattered and therefore less likely to be directly associated with the Nootka fault zone. From

our observations and the regional plate motion model (Braunmiller and Nábělek, 2002), we summarize our seismotectonic interpretations with a schematic diagram in Figure 2.19.

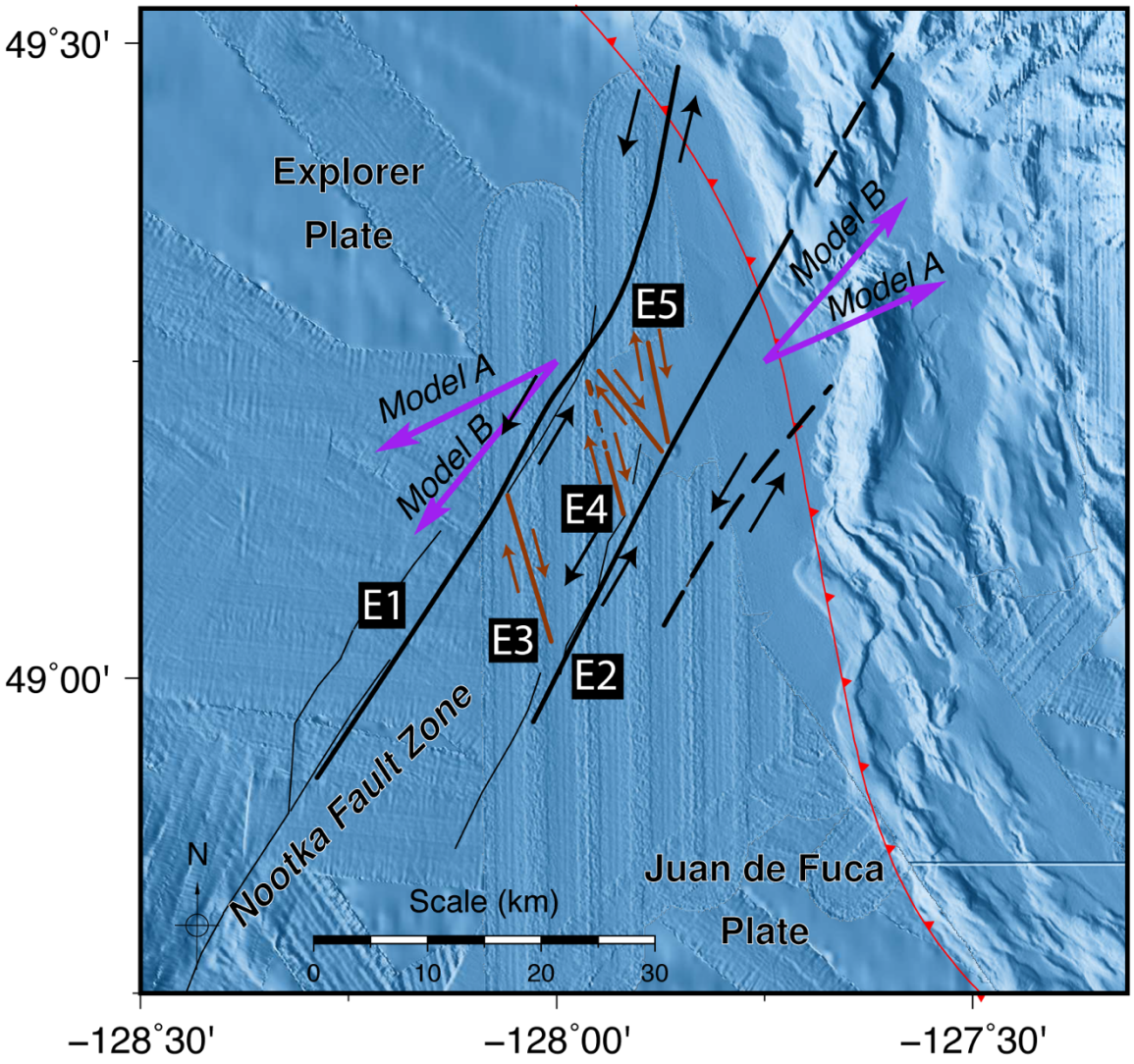

Figure 2.19. A schematic diagram summarizing the distribution of seismogenic structures based on the interpretations of our results. Primary and secondary faults are illustrated in black and orange, respectively. Black arrows indicate relative fault motion. Solid fault lines are well-determined, while dashed fault lines are less certain. The purple arrows show the relative plate motions between the Explorer and Juan de Fuca plates determined by Braunmiller and Nábělek (2002) for models A and B. The left-lateral motion on the primary faults correlate better with model B.

2.6.2 Interface Depths of the Juan de Fuca and Explorer Plates

Based on the distribution and depths of the interfaces delineated from the timing of converted phases, we have inferred their rheological implications and summarized our interpretations in

Table 2.5. Three major velocity discontinuities could be clearly identified while another was observed within the crust with fewer samples. In order of increasing depth, we have determined the velocity discontinuities to be 1) sedimentary basement, 2) upper/lower crust boundary, 3) oceanic Moho, and 4) the lower boundary of possibly SiO_2 enriched mantle and fracturing, discussed in detail in the next section.

The depth of the sediment/oceanic crust interface at the depth of ~4 km seaward of the subduction front (~2 km below the ocean floor) is well constrained by a large number of observations and can be found beneath other OBS stations as well, particularly s09, s10, s14, s15, and s25 (Table 2.5 and Figures 2.10, 2.11, and 2.15). However, it is not well-delineated by our tomography inversion.

A second, weakly resolved interface, is found at the depth of ~6.5 km (~4.5 km below the ocean floor). Landward of the subduction front, the upper/lower crust boundary deepens to ~10 km beneath stations s25 and s28. The inferred geometry and dip are remarkably consistent with that of the oceanic Moho (labelled ULCB in Figure 2.11). It may be representative of the seismic discontinuity between the upper and lower oceanic crust (a.k.a. seismic layers 2 and 3, Christensen and Salisbury, 1975). Conventionally, this discontinuity has been interpreted as a transition within the sheeted dike complex due to porosity changes and alteration that are expected to occur at depths greater than ~1.5 km below the sediment/crust interface (Detrick et al., 1994). This interpreted depth is shallower than the depth difference inferred from our observations (~2.5 km, Table 2.5 and Figure 2.11a). Instead, our results seem to support the interpretation that the converted phases originate at the transition from the basaltic sheeted dike complex to gabbro (White et al., 1992). Because the layer 2/3 boundary is gradational in nature, other unknown factors may contribute to a strong impedance contrast, which cannot be determined without further study.

The third interface is found at the depth of ~10 km seaward of the subduction front (~8 km below the sea floor). It correlates well with the observations beneath stations s09, s10, s14, s15, s24, s25, and s29, which we have interpreted to be the oceanic Moho discontinuity. It is worth noting that the Moho is most visible beneath stations s10 and s09, which have 96 and 49

converted phase observations, respectively. Due to the lack of station coverage landward of the subduction front, it is difficult to determine the precise geometry of the Moho at depths >15 km, but the converted-phase results closely match those of the tomography model (profile A–A', Figure 2.11). This interface also correlates well with the interpretations of Clowes et al. (1997), who found the depth of the oceanic mantle to be ~11-12 km within the Juan de Fuca plate seaward of the subduction front to the south of the Nootka fault zone, and a comparable oceanic Moho depth within the Explorer plate.

Profile A–A' in Figure 2.11 best shows the oceanic Moho, which dips at approximately 9-10° toward the northeastern end of the profile, with a sub-Moho velocity of ~7.5 km/s at the depth of ~20 km (~18 km below the sea floor). This dip is generally comparable to the subduction interface models proposed by Audet et al. (2010) and McCrory et al. (2012), which have approximate dips of 7.1° and 8.7°, respectively. Landward of the subduction front, the majority of observed seismicity deepens to 20-34 km, providing evidence for slab subduction. The low-velocity anomaly between the depths of 13 and 16 km landward of the subduction front (~60 km from the beginning of the profiles in Figure 2.11a–c) can be interpreted as the downgoing oceanic crust. Seaward of the subduction front, we observed a parallel high-velocity anomaly at a similar range of depths (HV; Figure 2.9a), which we interpret as unaltered uppermost mantle within the Juan de Fuca plate.

2.6.3 Fracturing and Seawater Infiltration of the Oceanic Mantle

The well-resolved part of the tomography model within the Explorer plate is indicative of an overall low-velocity structure between the depths of 8-18 km (Figures 2.9 and Figure 2.11; profiles D-D' and E–E'). This phenomenon can be explained by either thickening of the oceanic crust, alteration of the upper mantle to serpentinite, or fracturing and enrichment of pore spaces with SiO_2. Clowes and Malecek (1976) and Malecek and Clowes (1978) observed a similar result and attributed the phenomenon to thickening of the Explorer plate crust due to a potential folding with compression against the North American plate. However, this interpretation seems to be somewhat incompatible with our observation of normal-faulting earthquakes in this region (events No. 11 and 567).

While it is unlikely that the observed velocity lows are solely caused by serpentinization of the lower crust and upper mantle, fracturing of the Explorer plate may be enough to facilitate the infiltration of seawater into the uppermost mantle. Further, Rohr et al. (2018) found evidence for fluid flow in their observations of abundant deep reflectors within the Nootka fault zone. The net effect of slower mantle Vp would appear similar to a thickened crust. Unlike most areas examined in previous studies, the Explorer plate is very young and warm. Our 1-D thermal model for a cooling oceanic lithosphere with sediment accumulation (Figure 2.20), constructed using the method and code of Wang and Davis (1992), indicates temperatures exceeding 500°C by depths of ~12 km below sea level. At most, a narrow depth range of 1 km of the topmost mantle would be suitable for the stable presence of the hydrous mineral antigorite (the most stable form of serpentine high temperatures; Evans, 2004). The environment is unlike what has been observed for many outer rise settings where the subducting plate is older and colder (Van Avendonk et al., 2011; Fujie et al., 2013; Grevemeyer et al., 2007; Han et al., 2016; Ranero et al., 2003; Tilmann et al., 2008) . Although H_2O may infiltrate to this depth through fractures, the bulk permeability of the upper mantle is unlikely to allow the fluid to circulate at a high enough rate to have a significant cooling effect to preserve serpentinite.

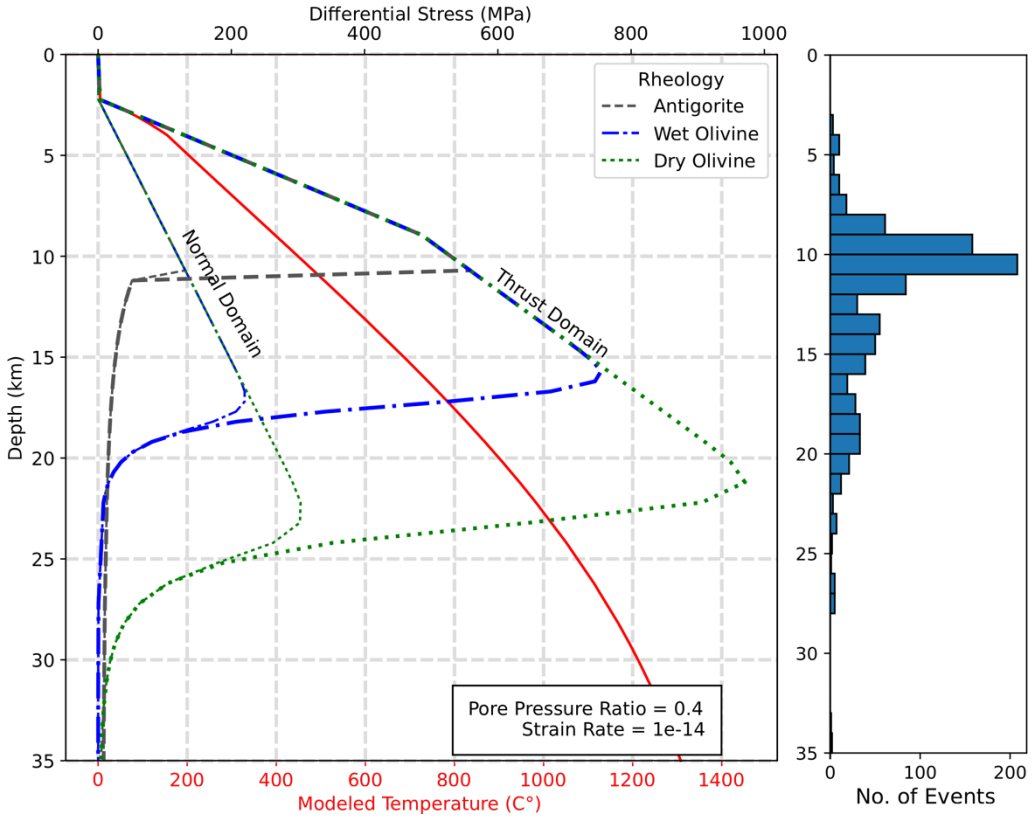

Figure 2.20. Left) Strength and temperature profile for the Nootka fault zone. Temperature increases with depth from 0° C at sea level to 1450° C at a depth of 60 km. Strength profiles for antigorite (a form of serpentine; dissolution creep; *Hilairet et al. 2007*), wet olivine (diffusion creep; *Karato and Wu 1993*), and dry olivine (diffusion creep; *Karato and Wu 1993*) rheologies are shown for both thrust and normal faulting domains. Normal domain rheologies are much weaker than the thrust domain, and since the Nootka fault zone is dominated primarily by strike-slip, the lithospheric strength falls somewhere between the two domains. The transition from brittle to ductile behaviour occurs at ~11 km, ~15 km, ~20 km for antigorite, wet olivine, and dry olivine, respectively. The smoothed profiles were produced based on equation (1) of Shimamoto and Noda (2014). All strength profiles shown assume a pore pressure ratio of 0.4 (nearly hydrostatic) and a strain rate of 1e-14 s^{-1}. Right) Binned (1 km) earthquake distribution by depth for the Nootka fault zone including events landward of the subduction front.

The low V_P/V_S ratios (< 1.73) dominating much of the Nootka fault zone (Figure 2.9b) is opposite of what would usually be expected of mafic rocks, which have V_P/V_S ratios that commonly exceed 1.82 (Brocher, 2005). Hydrously altered mantle, in particular, can have ratios as high as 2.21 (Christensen, 2004). However, in laboratory settings V_P/V_S ratios for serpentine have been observed to be dependent on the orientation of anisotropic mineral grains (Bezacier et al., 2010), varying from 1.2-3.4.

We observed high V_P/V_S at depths shallower than 11 km within the Nootka fault zone (Figure 2.11b). High V_P/V_S ratios were also observed east of the Nootka fault zone within the slightly

older and presumably colder Juan de Fuca plate down to as deep as 20 km. For both cases, the high ratios may indicate serpentinization or another phenomenon.

For the presence of both low seismic velocities and low V_P/V_S ratios within the Nootka fault zone, we propose two possible interpretations.

1) The degree of fracturing within the Nootka fault zone has led to decreased seismic velocities. Saroglou and Kallimogiannis (2017) found that wave velocities in samples of granite decrease exponentially with the increase of fracture density in the rock.

2) Because of the anisotropic variability of serpentine and the aforementioned high temperatures of the Explorer plate, it is unlikely that serpentinization is the sole explanation for the observed low V_P/V_S ratios. Alternatively, the in-filling of narrow pore spaces with SiO_2 or $CaCO_3$-enriched seawater, followed by the formation of talc or deposition of quartz or calcite, could lead to low V_P/V_S ratios. Quartz and calcite from within the sediment cover overlying the Nootka fault zone could dissolve in seawater, subsequently flushing into and precipitating as minerals in void spaces. This interpretation is compatible with previous studies that established low V_P/V_S ratios within mantle rocks could be accomplished by isolated, needle-shaped pores of fluid and by the precipitation of quartz in veins and pore spaces (e.g., Sato and Ito 2002; Zheng and Lay 2006). The composite elastic properties of quartz and peridotite lead to slight decreases in both V_P and V_S. But the decrease in V_P is more significant, resulting in a lower V_P/V_S ratio. As an alternative, SiO_2 in solution could drive the reaction with peridotite to form short-lived, unstable serpentinite; subsequently breaking down to produce the minerals talc and forsterite, and water. Talc has a characteristically low V_P (6.59 km/s) and V_P/V_S ratio (1.59) relative to typical mantle materials (Mainprice et al., 2008). It is a common product of hydrous alteration that can be found from mid-ocean ridges (e.g. Cannat, 1993; Mével, 2003) to the mantle wedge (Kim et al., 2013; Peacock and Hyndman, 1999). Talc is stable to temperatures exceeding 700 °C (Ewell et al., 1935; Pawley and Wood, 1995), meaning that it could feasibly form to depths of ~20 km (Figure 2.20), the downward limit of the large low-velocity anomalies identified within the Nootka fault zone.

The deepest interface is observed across several of the OBS stations (s09, s15, s25, and as single-phase depths at others). Depths to this interface range from ~14-18 km, while single reflections were calculated up to the depth of ~24 km (e.g. s29), which implies that either the depth resolution is not optimal, or the depth of fracturing and water infiltration is variable across the subducting plate. When observed in conjunction with the seismic tomography model (Figure 2.11), the interfaces often coincide with lenses of low-velocity anomalies (< 7.5 km/s) that probably are the manifestation of the above phenomena.

2.6.4 Variation of Seismogenic Depth for Major Faults

In Figure 2.20, we show the expected strength profiles for a 6.4 Ma old oceanic lithosphere together with the model temperature profile and the depth distribution of events within E1-E8. The depth distribution histograms for individual groups are provided in Figure 2.8. Because the values of the principal stresses causing the predominantly strike-slip regime are unknown, we show the strength profiles for normal-faulting and thrust faulting regimes as the lower and upper bounds. Based on the distribution of the low-velocity lenses (Figure 2.9a and Figure 2.11), we infer that the secondary conjugate faults and the surrounding rock mass may be less mature and, therefore, more diffusely fractured than the primary faults. Conversely, the primary faults extend to depths of ~20 km and cluster together tightly, as exhibited by the earthquake distribution (Figures 2.3 and 2.8), signifying that they are mature faults with concentrated fracturing (Goebel et al., 2017).

Almost all earthquakes delineating E3 occurred within the shallow oceanic crust, ranging from 6 to 14 km deep, with the majority occurring above the depth of 12 km. We suspect that E3 is representative of a series of immature faults in a body of highly fractured rock, and as a result, does not reach the depths observed for the primary faults.

Contrary to E3, the majority of E4 hypocenters are located within the lower crust/uppermost mantle at depths from 9 to 16 km. Another unique feature of E4 is that it seems to penetrate through the Moho discontinuity into the uppermost mantle. This feature is most evident from the distribution of hypocenters, located ~5 km west of station s14 on the C–C’ profile (Figure

2.11), extending into the high V_P (~ 8 km/s) region. This observation implies that the temperature condition in the uppermost mantle is still favorable for brittle rather than ductile deformation, further corroborating our stress diagram (Figure 2.20).

The majority of events from the western and eastern splays of E5 are located at the depths of 6-11 km and 11-15 km, respectively, which implies that the western splay exists within the upper crust, while the eastern splay exists within the lower crust. The largest event that occurred within the Nootka fault zone (M_L 3.5; Figure 2.7b) occurred less than one km north of a second mud volcano. These features mark the juncture between E5 and the southern boundary fault as an area with particularly high stress that is capable of relatively large moment release, and even of expelling sea water trapped in the fault system.

2.6.5 Abutment of the Explorer Plate by the Juan de Fuca Plate

From the well-resolved tomography results along the Juan de Fuca plate side of the Nootka fault zone, we observed a high-velocity anomaly at the depth range of 8–18 km (labels HV, HV1, and PHV; Figures 2.9 and 2.11). This anomaly may indicate a thinner Juan de Fuca plate crust toward its northern extent as compared to the model reported by Spence et al. (1985) (Figure 2.3). In relation to the Nootka fault zone, HV appears to abut the Explorer plate just seaward of the subduction front where the northern boundary fault seems to change its strike from 28° to 15° (Figure 2.9a). Although left-lateral strike-slip behaviour is still exhibited among the C-ranked focal mechanisms (Table 2.3), some thrust faulting appears toward the northern terminus of the northern segment (event No. 666). This change in strike and fault behaviour coincides with HV from the Juan de Fuca plate side of the Nootka fault zone indenting the low-velocity zone comprising much of the Nootka fault zone and what can be resolved of the Explorer plate (LV1 and LV2; Figure 2.9a, especially at the depths of 8 and 13 km). Additionally, seismicity within the southern primary fault appears to cease approximately 10 km west of the deformation front. We have determined that much of the Nootka fault zone exhibits a low-velocity anomaly across a wide range of depths (8-18 km) because it is inherently fractured and damaged due to compression in relation to North America. Speculatively, HV could be explained by the incorporation of mantle materials from the Juan de Fuca plate, effectively ploughing into the

trenchward end of the Nootka fault zone and altering the course of the northern boundary fault, particularly at the depth of ~13 km.

2.7 Conclusion

The Nootka fault zone is a transform boundary zone between the Juan de Fuca and Explorer plates located near the northern end of the Cascadia subduction zone (Figure 2.1 and Figure 2.19). From our analysis of hypocenter distributions and focal mechanisms, we have determined the orientation and sense of motion of the primary and secondary conjugate faults comprising the Nootka fault zone (Figure 2.19). Our results suggest that the Nootka fault zone is dominated by complex internal deformation with strike-slip. Its *b*-value of 1.07 is comparable to those calculated for the San Andreas fault and mid-ocean ridge/trench environments, but the limited duration of our study cannot provide a complete picture of the seismogenesis of the Nootka fault zone. The maturity of faults within the uppermost mantle may determine the maximum depth of the observed seismogenic layer (Figure 2.20), with a shallower base (~12-14 km) for much of the immature conjugate faults vs. the deeper primary faults (~20 km) (Goebel et al., 2017).

Within the Nootka fault zone, we identified velocity discontinuities from 3-D tomography (Figures 2.9 and 2.11) and converted phase analyses (Figure 2.16) and interpreted them as the sedimentary basement, upper/lower crust boundary, oceanic Moho, and the depth limit of hydrously altered mantle (Table 2.5). Our tomography results suggest that the low-velocity anomalies can reach the depth of ~20 km (LV and PLV1; Figure 2.9a and 2.11), well into the oceanic mantle. The low-velocity anomalies are most likely the product of a high degree of fracturing (Saroglou and Kallimogiannis, 2017). Further, low V_P/V_S ratios are indicative of mineral emplacement by silica or calcite-enriched seawater (Zheng and Lay, 2006), or of the formation of talc by the breakdown of short-lived serpentinite (Mainprice et al., 2008). Deep hydration is enabled by the infiltration of seawater into faults in the highly fractured Nootka fault zone and may have led to stable serpentinization within the top 1 km of the uppermost mantle.

Outside of the Nootka fault zone, few earthquakes were detected despite a dense seismic network to the south. In particular, we found no events that may have occurred along the interface of the Cascadia subduction zone. While the subduction interface could not be resolved with seismicity, we determined its dip to be 9-10° based on our tomography and converted-phase observations of the oceanic Moho discontinuity, which is comparable to the models proposed by Audet et al. (2010) and McCrory et al. (2012).

To the northeastern extent of the Nootka fault zone we observed reverse faulting (event No. 666). Reverse faulting, as well as the extinction of earthquakes along the southern primary fault near the subduction front and the abutment of a high-velocity anomaly (HV and HV1) into the Nootka fault zone in the depth range of 8–18 km (Figure 2.11a), has led us to conclude that the Juan de Fuca plate may be locally compressing against the Explorer plate in this region.

2.8 Supplementary Materials

2.8.1 Hypocenter Uncertainty

Hypocentral uncertainty ellipses were calculated for each event using the confidence scaling method of the Antelope GENLOC (GENeralized LOCation) package (Pavlis et al., 2004) and HYPOELLIPSE (Lahr, 1999). We present the average uncertainties determined by the GENLOC method in Table 2.1. Mean uncertainties for the 1,007 events in the vicinity of the Nootka fault zone are greatly improved in comparison to the complete SeaJade catalogue of 1,276 events (Table 2.1). For example, the mean major axis of uncertainty was reduced from 0.55 km to 0.08 km. These values vastly underestimate the true hypocenter uncertainty.

In order to better estimate location uncertainty, we performed a bootstrap analysis of our initial catalogue of 1,276 events. We randomly selected 80% of the associations with events and repeated the location process 1,000 times. For each event, we took the values of three standard deviations (equivalent to a confidence level of 99.7% in 3-D space) of the epicentral and depth distributions as the realistic uncertainties. This method is more rigorous than the confidence interval used in GENLOC in uncertainty estimation, which is 68.3%. Average major and minor axes of the uncertainty ellipses and the average depth uncertainty are given in Table

2.1. For the subset data containing only events in the Nootka fault zone region, the mean major axis and depth uncertainties from the bootstrap method are a factor ~33 (2.64 km vs 0.08 km) and ~11 (3.05 km vs 0.27 km) times that of the GENLOC estimates, respectively.

For the data relocated with TomoDD, we were unable to accurately determine uncertainties for the entire dataset due to the use of the least-squares linearization method (LSQR). In general, LSQR grossly underestimates location error (Waldhauser and Ellsworth, 2000). Instead, hypocenter uncertainties were first calculated for 147 events within the E3 group with the singular-value decomposition method (SVD). The mean ratio of the SVD to LSQR uncertainties for X, Y, and Z directions were extrapolated across the complete dataset in order to determine hypocentral uncertainties for the complete TomoDD derived catalogue. The averaged results are provided in Table 2.1, and show an improvement from the original catalogue by approximately 90%, such as reducing the mean depth uncertainty from 3.05 km to 0.39 km.

2.8.2 *b*-value

We utilize several methods outlined in Mignan and Woessner (2012) to determine the most accurate results for the magnitude of completeness (M_C), *b*-value, and *a*-value. Standard deviations for each method were ascertained by bootstrapping over 1,000 iterations. The methods utilized were maximum curvature (MAXC; Wyss et al., 1999), the goodness-of-fit test (GFT; Wiemer and Wyss, 2000), M_C by b-value stability (MBS; Cao and Gao, 2002), entire magnitude range (EMR; Woessner and Wiemer, 2005), and the median-based analysis of the segment slope (MBASS; Amorèse, 2007). Parameters determined from each method are listed in Table 2.2. The tests were performed with M_L bin sizes of 0.1, and exclude events from the SFZ (i.e., within the area bounded by latitudes of 49°N to 49° 7' 30"N and longitudes of 128° 3' 45"W to 127° 54'W). Due to the limited period of deployment, any events with M_L higher than 3.0 were excluded from b-value determination.

The best result of the *b*-value tests is shown in Figure 2.4. By visually analyzing the results and considering the standard deviations produced by the bootstrapping method, we have determined the best methods for the SeaJade dataset to be either MAXC or MBASS. The GFT

method also produced results very similar to the MBASS method, but has a slightly higher M_C, *a*-value, and *b*-value standard deviations of 0.15, 0.17, and 0.10, respectively, in comparison to 0.13, 0.10, and 0.07. The MAXC method has an M_C of 1.04, a *b*-value of 0.96, and an *a*-value of 3.81. The MBASS method has an M_C of 1.20, a *b*-value of 1.07, and an *a*-value of 3.96. When comparing the fitted data to input data, the MBASS method appears to have a better fit with high magnitude events, however, the magnitude range may not be complete at M_L 3.0, which can affect the result. Ultimately, we have determined that the MBASS method produced the best result. The MBS method overestimates M_C at 1.37, while the EMR method underestimates the M_C at 0.94.

2.8.3 Tomography Resolution

The resolution of our tomography model was determined with checkerboard tests at square sizes of 50, 10, and 6 kilometers in X, Y, and Z directions. Synthetic travel time for each phase arrival associated with an earthquake was calculated using a finite-difference scheme (Hole and Zelt, 1995). The checkerboard squares alternated between +/- 5% of 5 km/s. The synthetic travel-times were used in TomoDD to invert for the input velocity model. We found that tomographic features ≥10 km in size could be resolved for much of the study area (Figure 2.5 and Figure 2.6). V_P tomography, when compared to V_S tomography, better captures the velocity perturbations toward the outer fringes of the resolvable area. In general, the synthetic test results show some distortion at depths less than 5 km, and completely lose resolution below 20 km. The well-resolved checkerboards cover a large swath of area surrounding the Nootka fault zone where event hypocenters were most highly concentrated.

For further verification of the resolution of our seismic tomography model, we used the TomoDD output of average derivative-weight sum (DWS) values as a proxy for the density of rays travelling through each cell in the 3-D velocity model. The base-10 logarithm was taken for each DWS value, and is contoured on Figure 2.5 and Figure 2.6. It is apparent that raypath coverage is fairly low at both very shallow (<5 km) and deeper (>20 km) depths. These results are consistent with the checkerboard test results, as both show a similar range of depths and areas that can be resolved with confidence.

We also evaluated the variation of V_P/V_S ratio based on the results of our checkerboard test within the area bounded by latitudes 49°N to 49°15'N and longitudes of 128°7'30"W to 127°45' W, which can be used as a proxy for the possible V_P/V_S uncertainty. We found that the standard deviation of V_P/V_S is 0.06.

2.8.4 Detailed Discussion of Tomographic Velocity Anomalies

The below discussion provides further detail for the tomography provided in our Results section. Note that the sizes of the velocity anomalies were calculated via ellipses encompassing the anomalies.

At the depth of 8 km, a large high velocity anomaly (indicated by the label HV on Figure 2.9a) with an area of ~ 6,100 km^2 extends across the subduction front to the south of the Nootka fault zone, within the Juan de Fuca plate (Figure 2.9a). The background, 1-D velocity is 6.24 km/s, while the high velocity anomaly exceeds 6.36 km/s. Two prominent low velocities at this depth (< 6.11 km/s) are smaller; the first (LV1) is located near the intersection of profiles A-A' and D-D' with an area of ~1,100 km^2, and the second (LV2) is located along the subduction front extending from within the Nootka fault zone to the Explorer side with an area of ~2,200 km^2.

At the depth of 13 km, HV appears to have split into two (> 7.45 km/s; Figure 2.9a). The first and larger, HV1 (~3,800 km^2), is nearly parallel to the subduction front on the Juan de Fuca plate side but appears to extend past the southern hypocentral lineation of the Nootka fault zone. The second, HV2, is located ~20 km east of the subduction front, with an area ~2,400 km^2. LV1 and LV2 (< 7.16 km/s) continue to 13 km. LV1 appears larger, with an area of ~1,500 km^2, nearly connecting to LV2 toward the north. LV2, with an area of ~3,000 km^2, extends from west of the subduction front within the Explorer plate to east of the subduction front, where it abuts HV1.

By the depth of 16 km, a single high-velocity anomaly (HV; ≥ 7.92 km/s) with an area of ~5,900 km^2 spans from within the Juan de Fuca plate across the subduction front, but no longer appears to underlie the Nootka fault zone (Figure 2.9a). The low-velocity anomaly, LV (≤ 7.61

km/s), at this depth appears to be continuous and comprises much of the Nootka fault zone. It seems to extend east past the subduction front, with an area of ~8,800 km^2.

The velocity anomalies at the depth of 18 km are less discernible from the background velocity, and overall the tomography appears more homogeneous (Figure 2.9a). HV (≥ 8.02 km/s) has an area of ~2,900 km^2. LV (≤ 7.71 km/s), with an area of ~1,800 km^2, stays within the Nootka fault zone, away from the subduction front. Several smaller velocity anomalies, high and low, appear east of the subduction front, but the tomography resolution of ~10 km and raypath density (Figure 2.5 and Figure 2.10) rule them out for discussion.

Profile A–A' (Figure 2.11) follows the direction perpendicular to the strike of the subduction front through the Nootka fault zone. Near A', the seismic tomography model loses its resolution, and the original 1-D velocity model becomes apparent. The most prominent anomaly is a dipping (9-10°) high-velocity anomaly (indicated by the label PHV on Figure 2.11; ~7.5- 8 km/s) beginning at depths as shallow as 12 km below sea level at a distance of 30 km from point A along the profile and continuing down to 23 km at 75 km along the profile. The transition from ~6.5 km/s to ~8 km/s is less gradual than the initial 1-D velocity model, distinguishing higher velocity materials from lower velocity materials. Many of the relocated hypocenters occur within structures with velocities exceeding 7.5 km/s, presumably delineating the subducted plate. From point A to 25 km along the profile, low velocities (labeled as PLV1 in Figure 2.11) extend to depths of nearly 20 km. PLV1 dips toward the NE, underthrusting higher velocity structures.

Profile B-B' (Figure 2.11) follows the trend of the northern lineation (E1). The dip of PHV can be seen at a distance along the profile greater than 50 km. Seaward of the subduction front, some mixing of high velocity structures (~8 km/s) is observed within the surrounding lower velocity material (~6.5-7 km/s), particularly at 30 km along the profile at the depth of ~13 km. Two low-velocity anomalies (~5 km/s) extend below the depth of 6 km into the upper crust of higher velocity material at the distances of ~18 km (PLV1) and ~45 km (PLV2) along this profile. PLV2 lies above a larger low-velocity structure (6.8 km/s) extending to the depth of 18 km, where velocities increase by nearly 1 km/s over a depth range of just a few km to V_P > 8 km/s.

Along profile C-C’ (Figure 2.11), which follows the trend of the southern lineation (E2), the dipping structure PHV can be observed. PHV starts at the depth of 12 km at 25 km NE of point C, dipping at an angle of 7° to the depth of 18 km at a distance of 60 km along the profile. Just to the southwest of PHV (~17 km along profile C), PLV1 (6.5-7 km/s) extends to the depth of ~21 km.

Profile D-D’ (Figure 2.11) follows the trend of the secondary lineation E3. From north to south, a ~6.5-7 km/s low-velocity anomaly (PLV3), which may be analogous to PLV1, reaches the depth of 19 km at the distance of ~15 km from point D, becoming as shallow as 13 km at the distance of 30 km. A cluster of earthquakes located 8 km along this profile at the depth of ~18 km coincides with higher velocity (≥7.5 km/s) materials.

Profile E-E’ (Figure 2.11) follows the trend of the secondary lineation E5, crossing from the low-velocity anomalies seen in the Explorer plate (LV in Figure 2.9a), through the Nootka fault zone, to the high-velocity anomalies observed within the Juan de Fuca (HV in Figure 2.9a). Similar to profile D, we observe PLV3 extending to the depth of 18 km at ~20 km from the northern end of this profile. At ~30 km from point E, however, the low-velocities extend only to the depth of ~13 km, and continue across the rest of the profile at this depth (Figure 2.11). Contrary to profile D, many of the event hypocenters are located within the higher velocity (≥ 8 km/s) materials, especially on the northern segment.

Chapter 3 Significant geometric variation of the subducted plate beneath the northernmost Cascadia subduction zone and its tectonic implications as revealed by the 2014 M_W 6.4 earthquake sequence

Chapter 3 focuses on the geometric variation of the southern extent of the Explorer plate after subduction. The main body of this chapter consists of a manuscript submitted to a peer-reviewed journal formatted specifically for this dissertation. By utilizing earthquake hypocenter distributions and focal mechanisms, this study examines the complex deformation of the subducted Explorer plate perpendicular to the direction of convergence. In particular, a sequence of aftershocks following the rupture of a M_W 6.4 earthquake reveal bending and significant deformation of the subducting plate. Section 3.1 provides article information. Subsequent sections (3.2-3.6) present the article in full. Supplementary material to the article is presented in Section 3.7.

3.1 Article Information

3.1.1 Author and Coauthor Contributions

This chapter consists of a manuscript submitted to a peer-reviewed journal. The author of this dissertation, J. Hutchinson, carried out hypocenter relocations, statistical analysis, and focal mechanism calculations. Coauthor H. Kao and J. Hutchinson jointly designed and wrote most of the study. Coauthor M. Riedel was the Chief Scientist collecting OBS data for SeaJade II. Coauthor K. Obana provided initial phase picks and hypocenters for earthquakes. Coauthors K. Wang and S. Kodaira led the SeaJade project. Coauthors T. Tsutomo and Y. Yamamoto acquired data for SeaJade II. All coauthors provided useful feedback and contributions for refinement of the article.

3.1.2 Citation

Hutchinson, J., H. Kao, M. Riedel, K. Obana, K. Wang, S. Kodaira, T. Takahashi, and Y. Yamamoto, Significant geometric variation of the subducted plate beneath the northernmost Cascadia

subduction zone and its tectonic implications as revealed by the 2014 M_W 6.4 earthquake sequence, *Earth and Planetary Science Letters*, submitted.

3.1.3 Author's Names and Affiliations

Jesse Hutchinson[1], Honn Kao[1,2], Michael Riedel[3], Koichiro Obana[4], Kelin Wang[1,2], Shuichi Kodaira[4], Tsutomo Takahashi[4], and Yojiro Yamamoto[4]

[1] School of Earth and Ocean Sciences, University of Victoria, Victoria, BC, V8P 5C2, Canada

[2] Pacific Geoscience Centre, Geological Survey of Canada, Natural Resources Canada, Sidney, BC, V8L 4B2, Canada

[3] GEOMAR Helmholtz-Centre for Ocean Research Kiel, Kiel, Germany

[4] Japan Agency for Marine-Earth Science and Technology (JAMSTEC), Yokohama, Japan

3.1.4 Data and Resources

Seismograms used in this study were collected as part of the SeaJade II (Seafloor Earthquake Array – Japan Canada Cascadia Experiment) project. Arrival data, relocated hypocenters, and focal mechanism solutions can be found in Appendix Tables A.3, A.4, and B.2. Waveform data can be obtained from JAMSTEC upon request.

The Natural Resources Canada - Earthquakes Canada database was searched using http://www.earthquakescanada.nrcan.gc.ca/stndon/NEDB-BNDS/bulletin-en.php.

Some plots were made using the Generic Mapping Tools version 5.4.2 (http://gmt.soest.hawaii.edu/; Wessel and Smith 1998).

Global Multi-Resolution Topography (GMRT) was used to generate high resolution topography and bathymetry for GMT maps (Ryan et al., 2009).

3.2 Abstract

At the northernmost extent of the Cascadia subduction zone, the Explorer plate subducts at approximately 2 cm/yr, less than half the rate of the Juan de Fuca plate to the south. The transition boundary between these two plates is known as the Nootka fault zone, which is one of the focuses of the Seafloor Earthquake Array Japan-Canada Cascadia Experiment (SeaJade). During this survey, an M_W 6.4 earthquake occurred on 24 April 2014. This event and the subsequent aftershocks (referred to as the Nootka Sequence) reveal an approximately 40-km-long subducted fault within the Explorer Plate to the north of the Nootka fault zone. We infer that the fault is a subducted conjugate fault because of its nearly identical orientation to those seaward of the subduction front within the Nootka fault zone. The depth distribution and focal mechanisms of the aftershocks indicate significant margin-parallel deformation of the subducting plate. The subduction interface at the Nootka Sequence fault has been deflected downward to the northwest from a depth of approximately 15 – 25 km over a distance of 25 km. We propose two possible scenarios that are modified from previously suggested slab-tear model with induced margin-parallel mantle flow to explain the significant deformation of the young, warm subducting Explorer plate. To the northwest of this change in slab geometry, a lack of seismic activity above the plate interface indicates that the Explorer plate has partially decoupled from the overriding North America plate. We conclude that the geometric variation separating the southern Explorer plate from the north, along with decoupling and a possible intraslab tear, may be a significant combination to resist the propagation of a megathrust rupture across this boundary.

3.3 Introduction

The Cascadia margin is characterized by convergence of the subducting oceanic Explorer (ExP) and Juan de Fuca (JdF) plates with the North America (NAm) plate (Figure 3.1). The interplate thrust zone along the Cascadia subduction zone (CSZ) is capable of generating devastating earthquakes in exceedance of M_W 9, known as megathrust earthquakes.

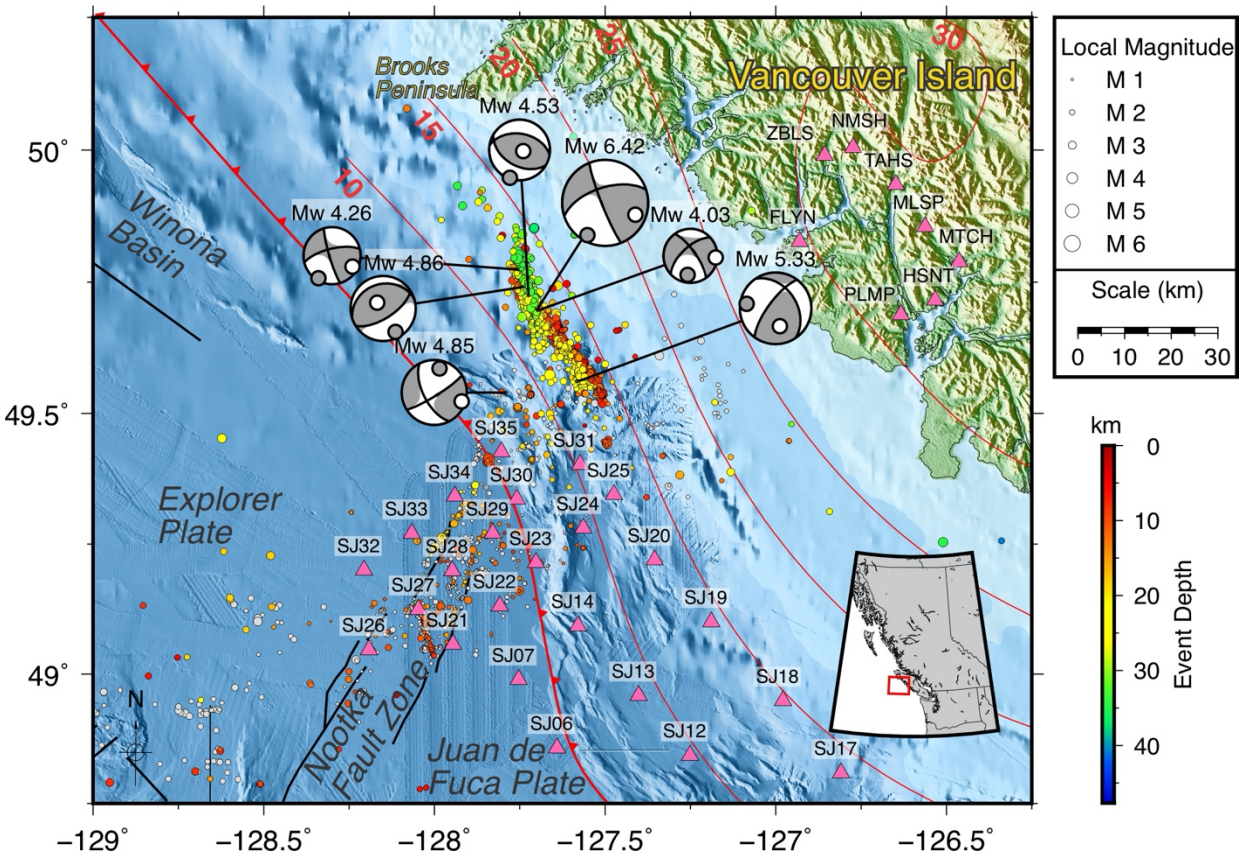

Figure 3.1. Map of the study area of the 2014 Nootka Sequence and the Nootka fault zone. The inset shows northwestern North America including British Columbia and Washington state, with the study area indicated by the red rectangle. Locations of earthquakes from the previous SeaJade I study are shown as filled gray circles. Earthquakes from this study are shown as circles filled with colour, which is dependent on depth. Circle sizes are indicative of earthquake magnitude. Seven moment-tensor solutions are labelled with their corresponding moment magnitude. The best-fit double couple solutions for the moment-tensors are shown as black curving lines. P- and T-axes are shown on the moment-tensor solutions with gray and white circles, respectively. Stations from both the ocean-bottom and land components of SeaJade II are shown as pink triangles. The subduction front of the Cascadia subduction zone is indicated by the curving red line running from northwest to southeast with triangular teeth pointing in the direction of subduction. The thinner red lines are 5 km contours, which deepen toward the northeast.

Paleoseismological studies have indicated that the physical dimension of a Cascadia megathrust event can vary significantly, from shorter (~200 km) ruptures along the southern margin to 1,350 km over the entire CSZ (Goldfinger et al., 2008; Goldfinger et al., 2012; Gao, 2016). One specific concern is whether the rupture of a megathrust earthquake can propagate across the boundary between the JdF and ExP, known as the Nootka fault zone (NFZ). If megathrust events were confined to the rupture area south of the NFZ, the maximum length would be ~1,100 km. Otherwise, the ExP can extend the Cascadia megathrust rupture by another 100–150 km.

The NFZ marks the division between the subducting ExP and JdF at the northern end of the CSZ (Figure 3.1). To the south of the NFZ, the JdF subducts at a rate of ~40 mm/yr (e.g. Wells and Simpson, 2001; Wang et al., 2003; McCaffrey et al., 2007), while to the north the ExP subducts at a rate of only 5-20 mm/yr (Braunmiller and Nábělek, 2002; Hyndman and Weichert, 1983; Riddihough, 1977). The ExP can be further subdivided, with a segment at the northernmost end known as the Winona Basin (Figure 3.1). The Winona Basin was formed as an independent tectonic block since ~4 Ma as the Pacific-America-Explorer triple junction migrated from the Brooks Peninsula westward to the Dellwood Knolls (Davis and Riddihough, 1982). While the Winona block may be cold enough to subduct (Gao et al., 2017), there is no evidence for a locked subduction interface north of the Brooks Peninsula (Dragert and Hyndman, 1995; Hyndman and Wang, 1995; Kao et al., 2009; Riddihough, 1984).

Delineation of the NFZ was made possible by the ocean-bottom seismometer (OBS) data collected from the first phase of the Seafloor Earthquake Array Japan-Canada Cascadia Experiment (SeaJade I). Thirty-three short-period OBS were deployed that recorded 1,276 earthquakes over a three-month period from July to September 2010. By comparison, only 85 events were recorded by land-based seismometers during the same period of time. Hutchinson et al. (2019) report that the NFZ is characterized by two primary bounding faults along with several conjugate faults between the two. These results agree with observations of shallow structures identified in several bathymetric and seismic reflection studies (Rohr et al., 2018).

Building on the success of SeaJade I, a second phase (SeaJade II) was conducted to monitor the trenchward segment of CSZ for any earthquakes along the subduction interface. One additional goal of the project is to further investigate the tectonic characteristics of the NFZ and the ExP. With a nine-month deployment, as opposed to the three-month deployment of SeaJade I, SeaJade II also provides an unprecedented opportunity to delineate the detailed geometry of the ExP through the distribution of local seismicity.

During the SeaJade II deployment, an M_W 6.4 earthquake occurred on 24 April 2014 landward of the NFZ. In the last two decades, there were two additional M_W 6+ earthquakes in the same area: one M_W 6.4 event on 2 November 2004 and another M_W 6.3 on 9 September 2011

(according to the online earthquake catalogue compiled by Natural Resources Canada). Although both 2004 and 2011 events were determined to have strike-slip mechanisms (Kao et al., 2012), their tectonic significance in the context of plate convergence along the northern Cascadia margin is largely unknown. In this study, we focus on the delineation of source characteristics of the 2014 earthquake and its aftershock sequence (referred to hereafter as the Nootka Sequence). Our observations depict, for the first time, how the geometry of the subducted oceanic plate varies across the JdF-ExP boundary. Our results also provide new insights into the geodynamics beneath the northern Cascadia margin. The possible role of the subducted NFZ acting as a barrier to the along-strike propagation of the Cascadia megathrust rupture is also discussed.

3.4 Data and Analysis

In the OBS layout for SeaJade II, we increased the station density relative to SeaJade I around the NFZ to better constrain hypocenters and to locate nearby earthquakes within the north adjacent ExP. A total of 35 short-period OBS were deployed in December 2013, and recorded data for 9 months (January-September 2014) (Riedel et al., 2014).

One additional component of the SeaJade II deployment is a complementary land-based array of broadband seismometers in the Nootka Sound region of Vancouver Island to enhance data resolution for the forearc region. Eight stations were deployed from October 2013 to mid-November 2014. Both the land and ocean seismometers deployed for SeaJade II recorded the 24 April, M_W 6.4 earthquake and its aftershocks.

We used the commercial software package *Antelope* to locate hypocenters. We first performed an automated search for *P*-phases on vertical seismograms with an STA/LTA threshold of 5.0. To better identify *S*-phases, we utilized the polarity filter as proposed by Ross and Ben-Zion (2014). Initial locations were determined with a grid search that required a minimum of 8 phase picks per event. We then reviewed all phases and locations to ensure the quality of picks, identified additional picks, and relocated the events with the dbgenloc module (Pavlis et al., 2004). In total, 45,352 *P*-phases and 49,636 *S*-phases were used to locate 3,170 earthquakes.

We applied the double-difference method (HypoDD) to refine our earthquake locations (Waldhauser and Ellsworth, 2000). For input, we calculated the squared coherency of cross-correlated waveforms between event pairs for each station. Any values with a squared coherency higher than 0.7 were implemented into a cross-correlation catalogue. We also calculated arrival travel-time differences between event pairs to form a differential travel-time catalogue.

We further improved the hypocenter distribution by applying the TomoDD method (Zhang, 2003) which jointly determines 3-D velocity tomography and earthquake hypocenters. A total of 2,867 events from the entire catalogue were relocated. The relative locations between HypoDD and TomoDD are similar; however, the locations calculated by TomoDD are generally deeper and should be considered more reliable due to TomoDD's adherence to absolute location data, as opposed to relative locations via HypoDD. We used the newly derived 3-D velocity model to relocate 1,557 events from 17 April to 30 May in the 2014 Nootka Sequence (Appendix Table A.4). Uncertainty estimates of epicenter and focal depth are given in Section 3.7.1 for readers interested in more technical details. The velocity model is included in Appendix C. The results and implications of the TomoDD tomography inversion are included in Chapter 4.

We determined focal mechanisms for events with 8 or more *P*-phases and $M_L \geq 2.0$. *P*-phase first motions were determined visually (also see Appendix B). We also calculated the *S*/*P* amplitude ratios to accompany the first motions for focal mechanism inversions using the program HASH (Hardebeck and Shearer, 2002, 2003). Only A-ranked focal mechanisms were kept for discussion in our results. To better visualize the overall characteristics, focal mechanisms associated with various tectonic structures are grouped using the classification system proposed by Alvarez-Gomez (2009). Appendix Table B.2 includes source parameters for all 502 A-rank events in addition to focal mechanisms from before and after the Nootka Sequence.

For events with $M_L \geq 4.5$, we performed moment-tensor inversions from broadband waveforms recorded at local and regional distances following the setup of Kao et al. (2012). A total of 7

events, including the mainshock, have high-quality waveforms suitable for moment-tensor inversion. Their source parameters are listed in Table 3.1.

Table 3.1. Moment-tensor solutions for large Nootka Sequence events. Moment-tensor solutions were calculated following the setup of Kao et al. (2012).

ID	Date	Latitude	Longitude	Depth	Magnitude (Mw)	mrr	mtt	mff	mrt	mrf	mtf	Class	CLVD (%)	Iso (%)	Avg. Misfit
812	2014-04-24 3:10:10	49.6983	-127.6991	20	6.42	70906.6667	-325023.33	254116.667	5.94E+04	-2.49E+05	355930	A1	8.2	9.1	0.276
2411	2014-04-24 3:23:34	49.5611	-127.5802	6	5.33	5336.66667	4963.56667	-10300.233	-6767.4	-5024.5	-322.57	B1	5.4	12.3	0.465
Not in SJII Catalogue	2014-04-24 3:40:57	49.54	-127.79	7	4.85	-491.64673	-1484.9766	1976.62337	-888.4001	-393.24	1068.6001	B2	22.6	-11.8	0.364
820	2014-04-24 3:44:17	49.7408	-127.74	8	4.86	1629.26347	-1533.4368	-95.826633	1255.6001	877.74	-913.0101	B3	25.5	-2.2	0.447
855	2014-04-24 5:16:18	49.7242	-127.7238	11	4.53	757.436	-688.384	-69.052	-23.146	-134.23	250.13	B1	1.1	6.6	0.417
1029	2014-04-24 8:09:56	49.6963	-127.697	7	4.03	-6.1637333	-102.67313	108.836867	81.257	-19.786	25.371	B4	52.1	0.6	0.355
1069	2014-04-24 12:06:47	49.7738	-127.7558	14	4.26	63.74	-172.145	108.405	13.371	-94.4417	245.88	A3	28.4	9.5	0.298

The depth parameter is measured in km. The magnitude parameter is measured in moment magnitude (M_W). The moment-tensor components; mrr, mtt, mff, mrt, mrf, and mtf are provided in the Harvard CMT convention. The class parameter is a measure of the quality of the CMT solution, with A1 being the highest quality possible. CLVD and Iso. are percentage measurements of the compensated linear vector dipole (CLVD) and isotropic (Iso.) components of the CMT solution.

3.5 Results and Implications

The Nootka Sequence began with an M_w 6.4 mainshock at 3:10 GMT on 24 April 2014. Several M_W 4+ aftershocks occurred within hours of the mainshock. The largest aftershock (an M_W 5.3 event) occurred ~13 minutes later with an epicenter nearly 20 km southeast of the mainshock (Figure 3.1).

During the entirety of the Nootka Sequence, nearly all portions of the rupture area were active. Within the first day, 268 events occurred, followed by 153 and 120 events during the second and third days, respectively. By 30 May 2014, there were only 8 events per day. The decreasing rate of earthquakes per day is best fit by the modified Omori law with a *p*-value of 0.9 (Omori, 1894; Utsu, 1961) (Figure 3.2). No earthquakes were observed in the Nootka Sequence area prior to the mainshock but the seismicity continued until the completion of SeaJade II. There were 14 aftershocks with $M_L \geq 4$, while the vast majority of the Nootka Sequence have M_L less than 3 (Figure 3.3). During the aftershock sequence, all portions of the rupture area appear to have been active with no apparent spatio-temporal patterns (Figure 3.2).

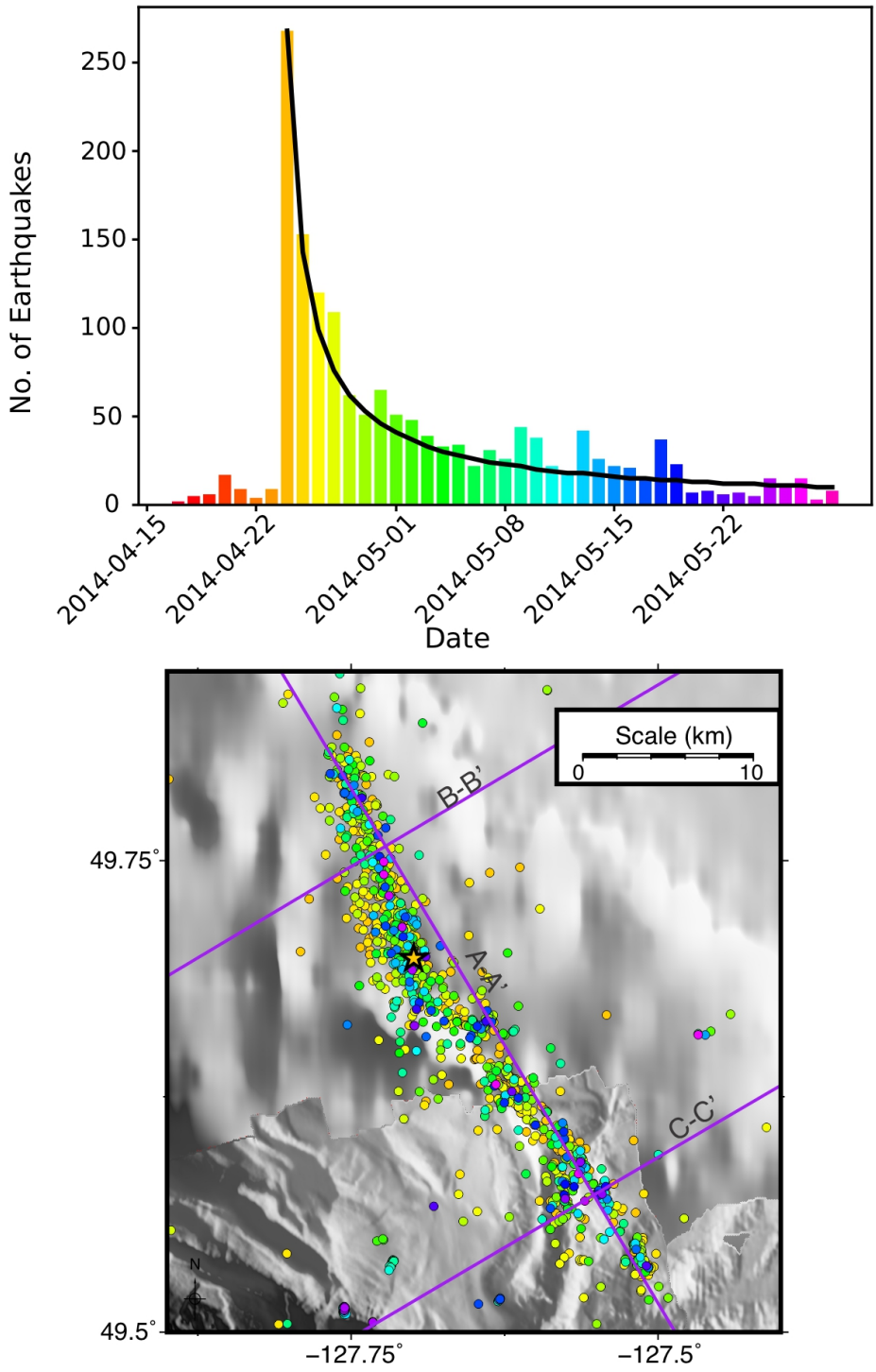

Figure 3.2. Top) Distribution of the number of earthquakes by day. The dates range from 17 April – 29 May 2014. The Nootka Sequence began on 24 April 2014, which is clearly indicated by the peak number of events. The number of earthquakes per day decay following the modified Omori Law (Omori, 1894; Utsu, 1961) with a *p*-value of 0.9, which is indicated by the curving black line. Bars are coloured based on date. Bottom) Map of the Nootka Sequence showing the spatio-temporal distribution of events. Earthquakes are shown as equal sized circles. Colour corresponds with the dates shown in the histogram above. The M_W 6.4 Nootka earthquake is shown as a star.

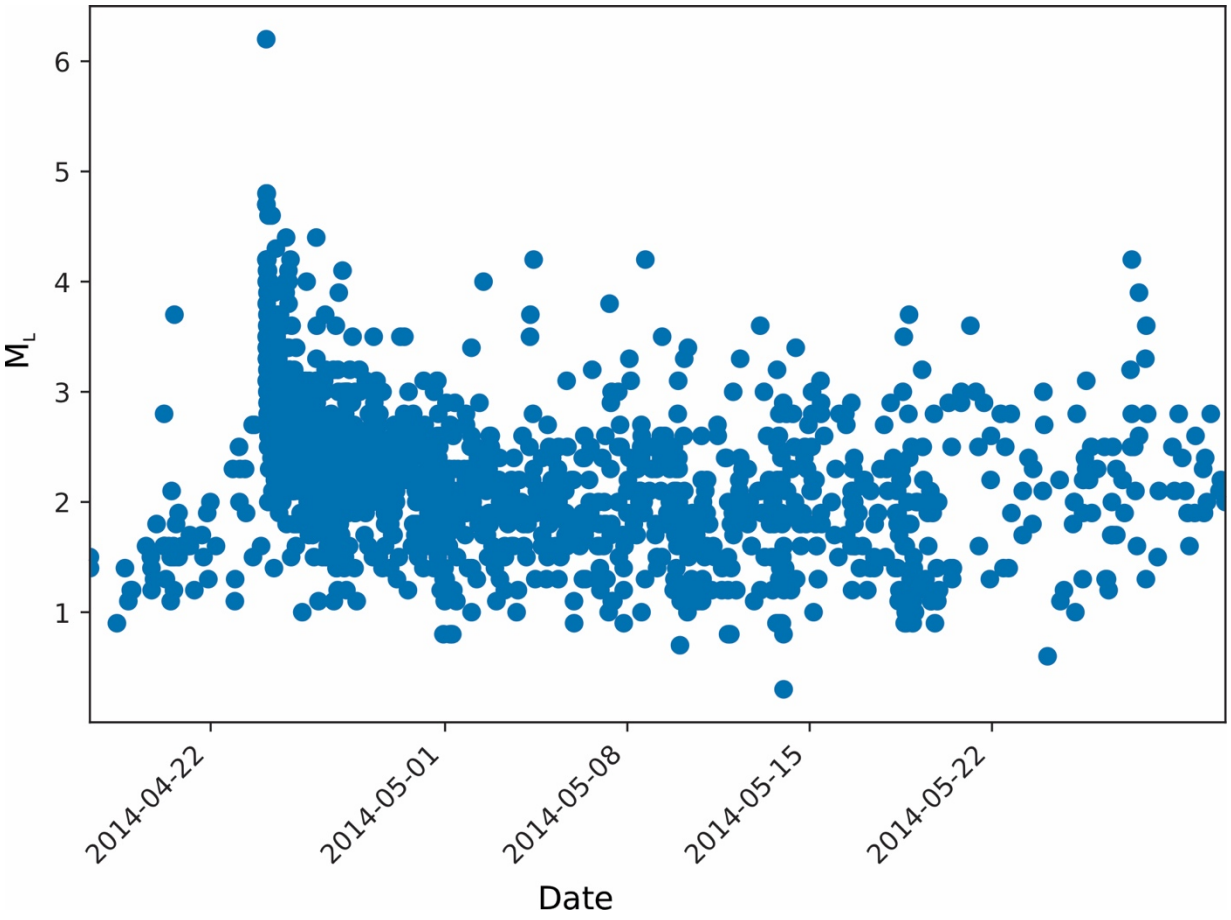

Figure 3.3. Daily distribution of local earthquake magnitude (M_L) of the Nootka Sequence. The dates range from 17 April – 29 May 2014.

We take two different approaches to determine the Gutenberg-Richter (G-R) distribution of the observed Nootka Sequence seismicity: the goodness-of-fit method (GFT; Wiemer and Wyss, 2000) and the maximum curvature method (MAXC; Wiemer and Wyss, 2000). The standard deviations of the G-R parameters are derived from bootstrapping over 1,000 samples per test. With the GFT method the *a*- and *b*-values are 4.86±0.26 and 0.86 ± 0.08, respectively, with a magnitude of completeness (M_C) of 2.43 ± 0.23. In comparison, with the MAXC method the *a*- and *b*-values are 4.44 ± 0.22 and 0.72 ± 0.08, respectively, with an M_C of 2.12 ± 0.21. The difference in *b*-value between the two methods is probably due to the irregular slope, which changes around M_L 3. Ultimately, we favour the GFT results due to the overall better fit of the slope to the data (Figure 3.4). The b-values in these results vary significantly from the 1.07

calculated from the SeaJade I data (Hutchinson et al., 2019), exhibiting temporary variation stimulated by the mainshock.

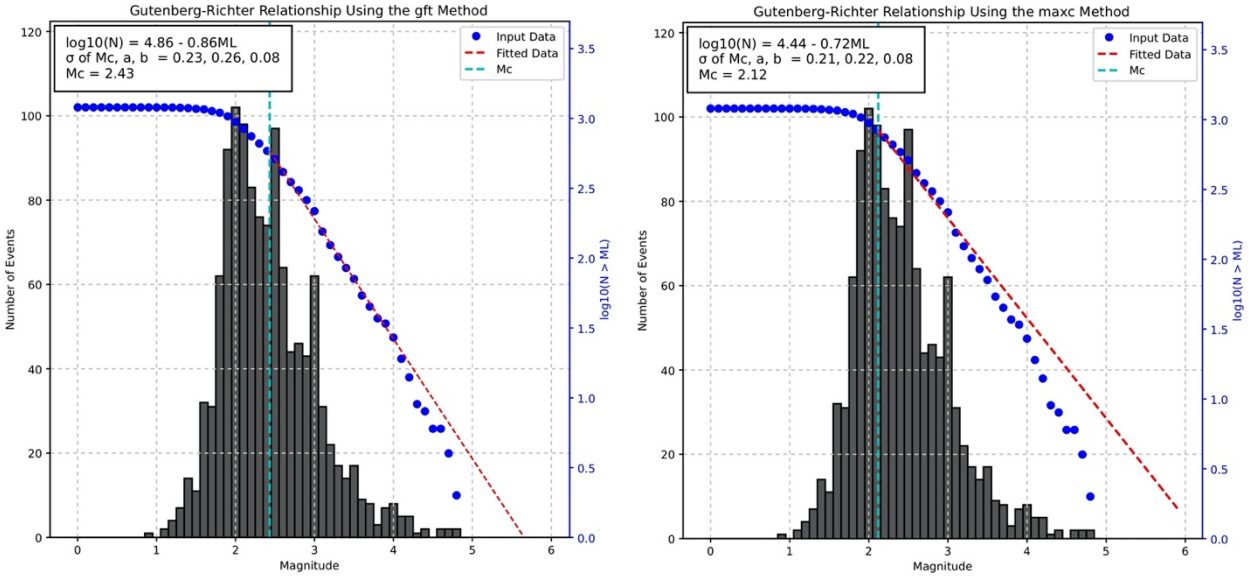

Figure 3.4. Gutenberg-Richter relationships for the Nootka Sequence determined via the GFT and MAXC methods (Wiemer and Wyss, 2000). For the GFT method, the b-value is 0.86 ± 0.08, the a-value is 4.86 ± 0.26, and the magnitude of completeness (M_C) is 2.43 ± 0.23. For the MAXC method, the b-value is 0.72 ± 0.08, the a-value is 4.44 ± 0.22, and the magnitude of completeness (M_C) is 2.12 ± 0.21.

3.5.1 Rupture Zones of the Nootka Sequence

Epicenters of the Nootka Sequence form a linear feature landward of the subduction front that extends nearly 50 km in length (Figure 3.5). This linear feature presumably is the fault system that ruptured in the wake of the M_W 6.4 mainshock. Given the proximity and similarity to the orientation of the conjugate faults within the NFZ (Hutchinson et al., 2019), we infer that it is a conjugate fault that either 1) continued to enlarge after subduction, or 2) was larger before subduction, perhaps because the NFZ was less mature. While the NFZ appears to narrow toward the subduction front (Rohr et al., 2018), we cannot distinguish between the two hypotheses without additional evidence.

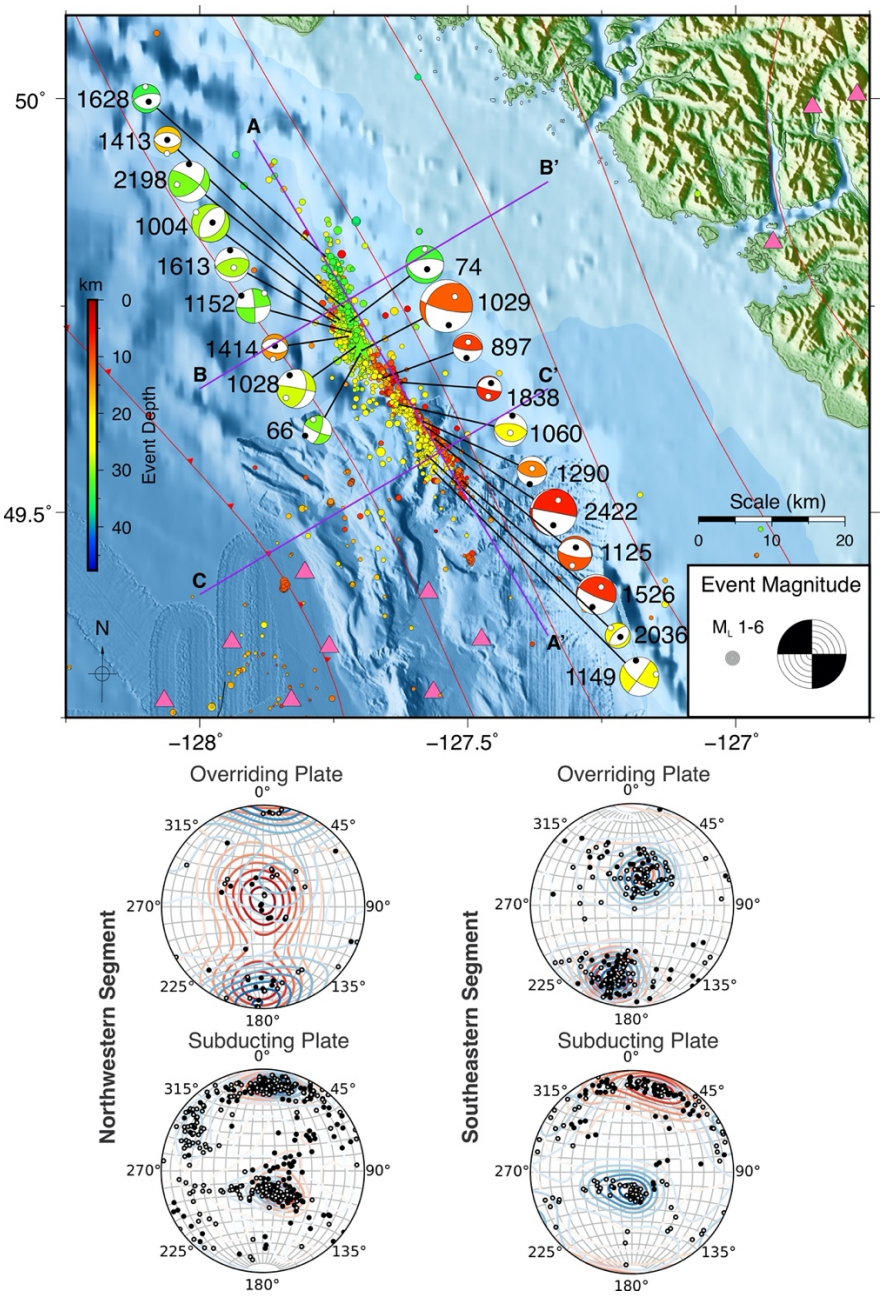

Figure 3.5. Top) Map focusing on the Nootka Sequence earthquakes and selected focal mechanism solutions. P- and T-axes are indicated on the focal mechanism solutions as black and white circles, respectively. Red lines indicate the estimated subduction interface depth, increasing in 5 km intervals towards the east, derived from Audet et al. (2010). The fault trace of the northern Nootka fault from Rohr et al. (2018) is shown as a black line in the lower left of the map near -128°. Earthquake depths are indicated by colour, and local magnitude (M_L) is indicated by size. The purple lines are representative of cross-section profiles, which are shown in Figure 3.6. Pink triangles represent SeaJade II seismometers. Focal mechanisms are labelled with their event IDs. Bottom) P- and T-axes directions for all focal mechanisms are shown on the stereonets. The diagrams are subdivided by which segment of the Nootka Sequence they were located in, and whether they were in the overriding plate or the subducting plate. The P-axis orientations are black, while the T-axis orientations are shown in white. Contours representing the greatest concentrations of P- and T-axes are shown in red and blue, respectively.

On average, the distribution of seismicity of the Nootka Sequence strikes ~324.4 ± 0.3° with a nearly vertical dip (Figures 3.5 and 3.6). Its width ranges from ~4 km on the southeast and northwest ends to ~6 km toward the center. In Figure 3.6, vertical profiles along the Nootka Sequence are shown with profile A-A' running parallel to the Nootka Sequence and profiles B-B' and C-C' running perpendicular. For the region southeast of profile C-C', the estimated depths to the oceanic basement and Moho were based on results from SeaJade I (Hutchinson et al., 2019) and receiver function analysis from land measurements (Audet et al., 2010). The depth to the interface northwest of profile C-C' is based on the distribution of hypocenters derived in this study.

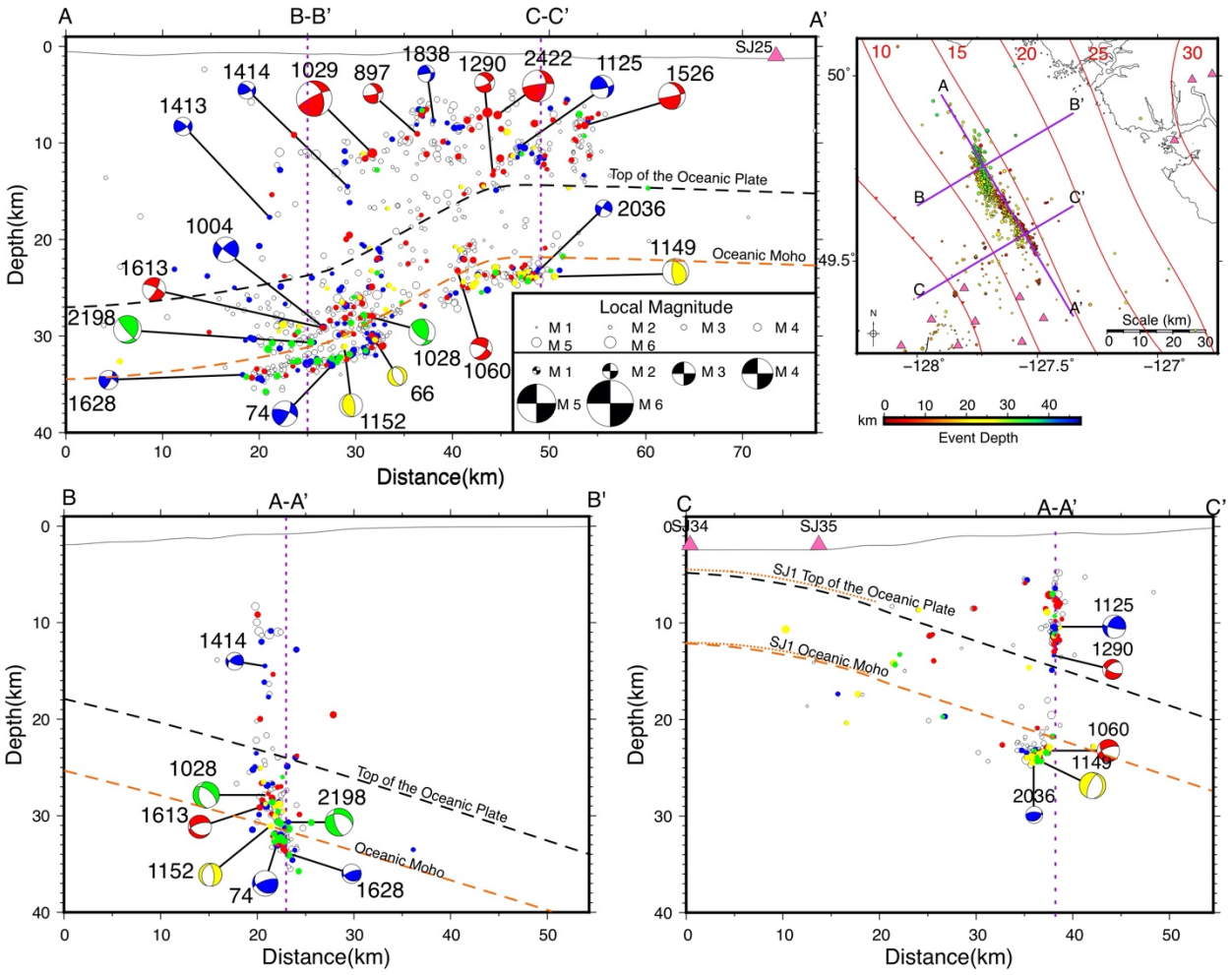

Figure 3.6. Profiles of earthquake hypocenters and selected focal mechanisms. The locations of lines A-A', B-B', and C-C' are shown in the upper-right map and in Figure 3.5. Earthquake hypocenters from ± 5 km of the profiles are shown as open circles. Hypocenter and focal mechanism size are indicative of magnitude. The black dashed lines represent the subduction interface as derived from Audet et al. (2010), and have been further modified based on the distribution of hypocenters from this study. Profile A-A' is along-strike of the Nootka Sequence. Profile B-B' is perpendicular to profile A-A' along the northwestern segment of the Nootka Sequence, while profile C-C' is perpendicular to profile A-A' along the southeastern segment. Estimated depths to the top of the oceanic plate and the oceanic Moho are indicated by dotted orange lines in profile C-C' and were derived from Hutchinson et al. (2019). Focal mechanism colour is representative of the mode of failure: red – reverse, blue – normal, yellow – strike-slip, green – strike-slip oblique reverse. Unlabelled, coloured circles are associated with the listed focal mechanism types. A simplified map of the Nootka Sequence and the profile lines is shown in the upper-right. Red lines indicate the estimated subduction interface depth, increasing in 5 km intervals towards the east, derived from Audet et al. (2010). The fault trace of the northern Nootka fault from Rohr et al. (2018) is shown as a black line in the lower left of the map near -128°.

The nearly vertical geometry of the Nootka Sequence fault is indicated by tightly clustered seismicity within both the subducting oceanic plate and the overriding continental plate, best

visible on profiles B-B’ and C–C’ (Figure 3.6). In general, shallower events tend to occur more toward the southeast than northwest (Figure 3.7).

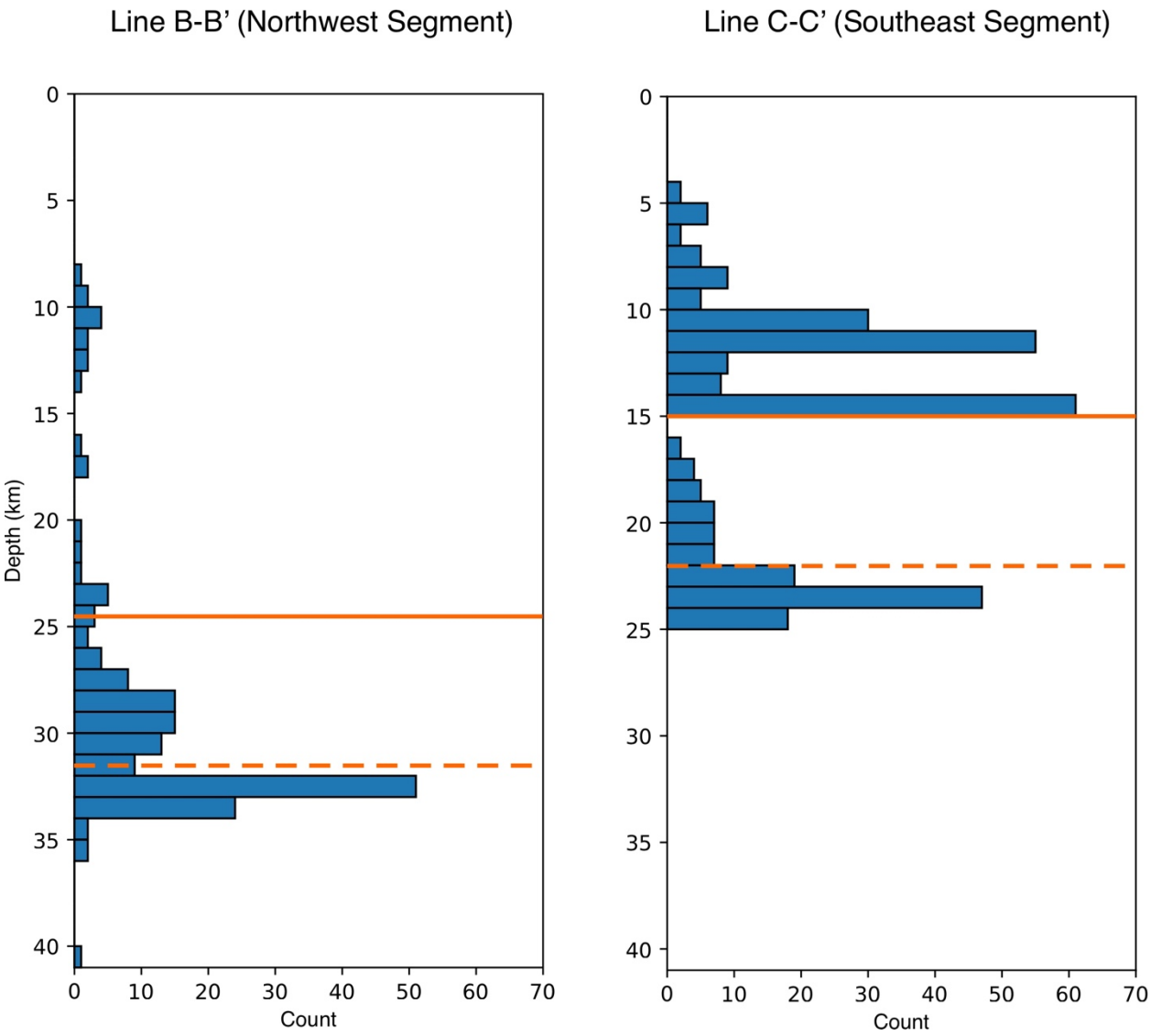

Figure 3.7. Depth distributions of earthquakes along lines B-B’ and C-C’. Events within ± 3 km of the profile lines were included in the calculation of the number of earthquakes per kilometer. Lines B-B’ and C-C’ are within the northwestern and southeastern segments of the Nootka sequence, respectively. Estimated depths to the top of the oceanic plate are shown as solid orange lines, while the oceanic Moho is indicated by dashed orange lines.

We roughly divide the Nootka Sequence fault into two segments, southeast and northwest, based on the distinctive seismogenic behaviors on either side of the middle point (at the distance of ~40 km along profile A-A’). Specifically, hypocenters are 5–10 km deeper in the northwest segment compared to the southeast segment (Figures 3.6 and 3.7).

Characteristics of the southeastern segment

On the map view, the distribution of seismicity in the northwestern segment has a strike of ~321° (Figure 3.5), with a nearly vertical dip in profile view (Figure 3.6). Seismicity in the southeastern segment of the Nootka Sequence shows a clear bimodal distribution in depth (profile A–A' in Figure 3.6; southeastern segment in Figure 3.7), which coincides with the depths of overriding and subducting plates determined by previous studies (Audet et al., 2008; Hutchinson et al., 2019; McCrory et al., 2012). Within the overriding plate, the majority of events occurred between depths of 5 and 15 km. Within the subducting plate, most events occurred below the oceanic Moho between depths of 19 and 26 km.

The presence of aftershocks within the overriding plate suggests that the M_W 6.4 event is large enough to cause fault failures above the plate interface. The focal mechanism pattern appears to be very complicated, as normal (e.g., event no. 1125), reverse (e.g., events no. 1290, 1526 and 2422), and strike-slip-faulting (e.g., event no. 1149, Figures 3.5 and 3.6) are all observed. The distribution of P- and T-axes form two clusters in the NNE–SSW direction (azimuths of 10-20° and 190-200°, Figure 3.5). One of the deepest events in this group (event no. 1290) shows low-angle thrust-faulting consistent with the geometry of the plate interface (profile C–C', Figure 3.6). It may represent a small stress perturbation along the interface thrust zone in response to the Nootka earthquake rupture.

The focal mechanism pattern within the subducting plate is equally complicated. Statistically, the orientations of P- and T-axes are different from those in the overriding plate. One particular event (no. 2036) shows normal-faulting with its T-axis parallel to the strike of the Nootka Sequence fault (Figures 3.5 and 3.6). It is probably a manifestation of along-strike extension within the subducting slab in association with lateral plate bending. A group of reverse-faulting events are observed near the boundary between the northwestern and southeastern segments (e.g. event no. 1060). They probably reflect the compression associated with the dramatic structural distortion of the Nootka Sequence fault within the subducted plate.

Strike-slip events occurred primarily just below the oceanic Moho (e.g. event no. 1149). Most of them have strikes roughly consistent with the Nootka Sequence fault, similar to the mainshock. Our results indicate that the topmost oceanic mantle has a seismogenic thickness of ~5–7 km (Figure 3.6).

Characteristics of the northwestern segment

On the map view, the distribution of seismicity in the northwestern segment appears to be slightly broader with a strike of ~335°. This orientation is about 24° more than the southeastern segment (Figure 3.5). Similar to the southeastern segment, hypocenters are distinctly separated in the overriding and down-going plates (Figure 3.7). However, the vast majority of events occurred within the down-going plate between depths of 20 and 36 km. This depth range is ~10 km deeper than the southeastern segment. Within the overriding plate, the number of hypocenters peaks at ~12 km with a general trend of deepening toward the northwest. However, the level of seismic activity within the overriding plate is significantly lower compared to the southeastern segment, while within the subducting plate the numbers of events are comparable (Figure 3.7).

We observe dominantly normal-faulting focal mechanisms within the overriding plate with T-axes approximately in the N–S direction (e.g., events no. 1413, 1414 and 1838, Figure 3.5). However, a few reverse-faulting events also exist in this group (e.g., events no. 897 and 1029). The co-existence of different focal mechanisms again demonstrates the complex deformation at the local scale associated with the 3D geometric variation of the subducted plate.

T-axes of normal- and strike-slip-faulting events within the subducting plate show two dominant orientations, namely, NNE–SSW and WNW–ESE (Figure 3.5). The NNE–SSW T-axes (e.g., events no. 74, 1028, 1152, 1413, 1414, and 1628) are compatible with the direction of downdip extension, and probably manifest the slab-pull effect.

The group of events showing NWW–SEE T-axes, on the other hand, are more compatible with lateral extension within the down-going plate (events no. 66, 1004, and 2198; Figure 3.5). Additionally, we delineate a number of reverse-faulting events at the distance of ~30 km along

profile A-A’ in the depth range of 25–32 km (e.g., event no. 1613). These compressional events generally occur above the normal and strike-slip events with lateral T-axes, indicating compression and extension at the upper and lower portions of the seismogenic layer, respectively. Such a contrasting state of strain is typical of plate unbending, except in this case the unbending happens laterally rather than along the downdip direction.

Overall, there is an approximate 20° rotation in the average P- and T-axes directions between the southeastern and northwestern segments (Figure 3.5). This difference corresponds well to the change in strike of the subduction front, which rotates counter-clockwise from approximately 350° in the south to 330° in the north (Figure 3.1).

3.5.2 Geometric variation of the oceanic plate across the JdF-ExP boundary

If we extrapolate the plate interface and oceanic Moho from the southeastern end of the Nootka Sequence fault toward the northwest following the two-layered distribution of seismicity, we can deduce the approximate locations where the Nootka Sequence fault intersects the plate interface (referred to as the fault-interface intersection) and the oceanic Moho (i.e., the fault-Moho intersection). The inferred plate interface and oceanic Moho are delineated by the dashed black and orange lines, respectively, in Figure 3.6. We further constrain the depth to the Moho with depth distributions along profiles B-B’ and C-C’. With this approach, the seismicity distribution of the Nootka Sequence effectively illuminates the geometry of the subducting oceanic plate.

Assuming that the oceanic crustal thickness is the same over the source area of the Nootka Sequence (~7–8 km), the generally deeper seismicity in the northwestern segment implies that the fault-interface and fault-Moho intersections plunge toward the northwest. The largest plunge is observed near the middle of the source area (at the distance of ~35 km on profile A–A’, Figure 3.6), resulting in an overall drop of approximately 5–10 km in the depth of the plate interface over the dimension of the Nootka Sequence fault.

To further confirm our observation of increasing hypocenter depths (and thus a deeper plate interface and oceanic Moho) toward the northwest, we conduct additional tests on the

accuracy of focal depths for two representative events located separately within the northwestern and southeastern segments. Specifically, we want to verify that the SeaJade II OBS network has sufficient resolution for the hypocenter locations along the Nootka Sequence fault such that the focal depth difference between the two segments cannot be an artifact due to location uncertainties or picking errors.

As presented in Figure 3.8 (with technical details in Section 3.7.2), the *P*- and *S*-arrival times of event no. 1149 (which is located near the southeastern terminus of the Nootka Sequence fault; Figures 3.5 and 3.6) can be explained by a source depth of 23.8 km, whereas event no. 74 (located near the middle of the northwestern segment) has a depth of 33.1 km. A deeper solution at 33.1 km (and therefore a slightly earlier origin time to ensure the same arrival time of the *P*-phase at the closest station) for event no. 1149 would lead to *S*-phase arrivals consistently later than those predicted at close distances (SJ31 and SJ25, Figure 3.8) and earlier *P*- and *S*-arrivals at farther distances (SJ28 and SJ07). The exact opposite pattern can be obtained if a shallower depth of 23.8 km is assumed for event no. 74.

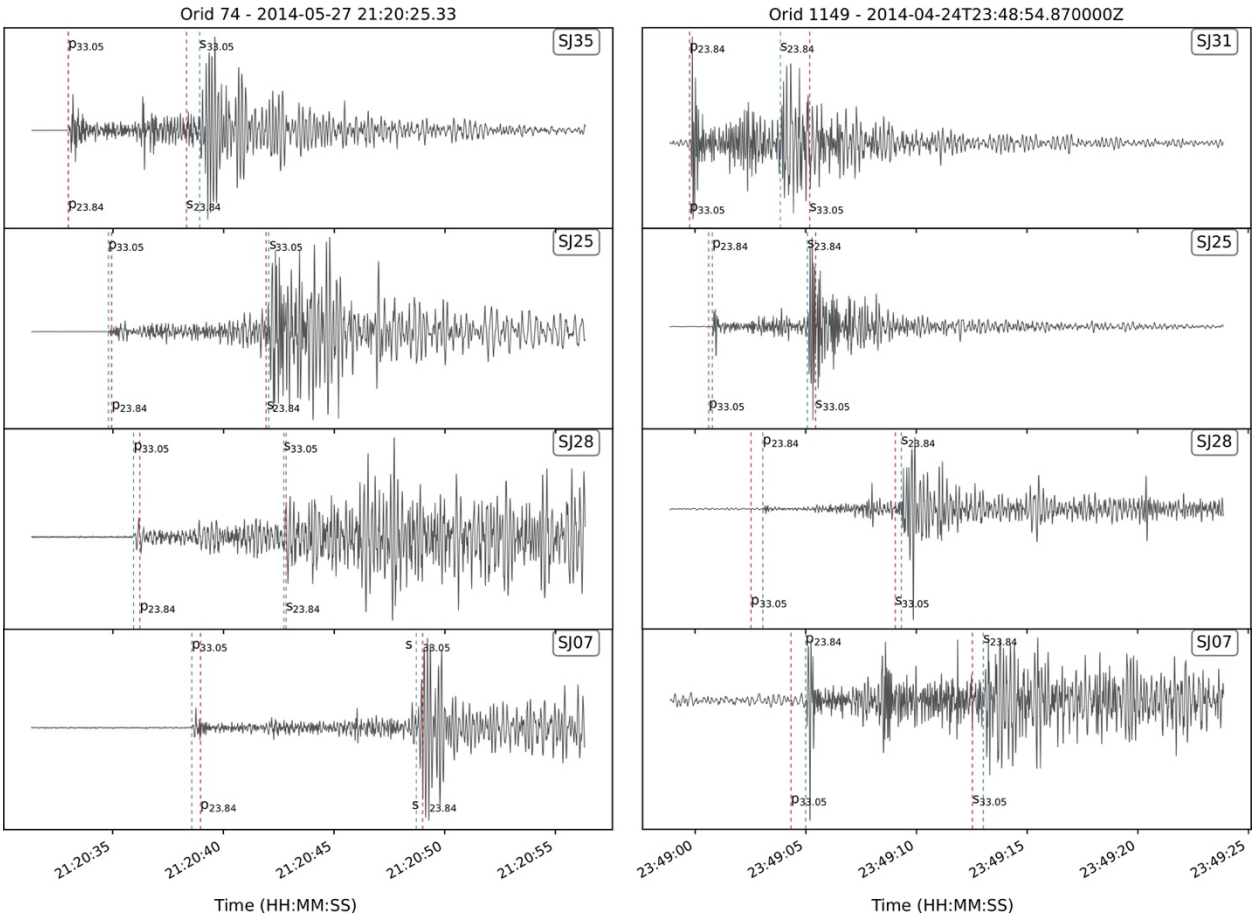

Figure 3.8. Seismograms of two select earthquakes (events no. 74 and 1149) at various stations. The stations are organized from the top by increasing distance from the events. With the exception of the nearest stations, the stations shown for each event are identical. Predicted P and S arrivals at calculated hypocentral depths are indicated by dashed blue lines. Predicted arrivals from synthetic depths are indicated by dashed red lines. All arrivals have been time-corrected. Events no. 74 and 1149 are located in the northwestern and southeastern segments, respectively.

We infer that the ExP bends downward immediately northwestward of the JdF–ExP boundary (Figure 3.6). Such geometry would result in a slightly steeper subducted slab on the ExP side of the NFZ, which is contradictory to existing slab geometry models (e.g., Audet et al., 2010; McCrory et al., 2012) that all show a shallower dipping ExP with respect to JdF. The unusually shallow ExP slab near the northernmost edge of the CSZ was first reported by Audet et al. (2008) based on receiver function analysis and seismic *P*-wave tomography. They proposed that the ExP has undergone stretching (i.e., thermomechanical erosion) due to a margin-parallel mantle flow around the northwestern edge of the ExP. This thermomechanical effect probably leads to increasing buoyancy and, in turn a shallower dipping slab with a slower subduction

rate. This model is consistent with shear-wave splitting measurements on northern Vancouver Island where the fast polarization directions systematically turn counter-clockwise from margin-normal in the south to sub margin-parallel in the north (Mosher et al., 2014).

By studying the arc-parallel gradients in trace element abundances (Ni, Cr, and Mg/Mg+Fe) and isotope ratios, Mullen and Weis (2015) also infer the existence of a margin-parallel mantle flow around the slab edge in the northern Cascadia arc. However, their model considers the downdip trajectory of the NFZ as an interplate tear boundary where the tearing offset between the shallower ExP and the deeper JdF slabs facilitates the trench-parallel southerly flow.

Our observation of a slightly deeper subducted ExP slab immediately across the JdF–ExP boundary adds one more degree of complexity to the already puzzling scenario of subduction dynamics in northern Cascadia (Long, 2016). While our results do not bear direct evidence for the existence of a margin-parallel mantle flow, we are confident that the subducted NFZ remains intact until at least 30–40 km depth. Given the hypocenter distribution of the Nootka Sequence, an interplate tear boundary as proposed in the Mullen and Weis (2015) model is unlikely. Instead, the tear, if it exists, could be an intraplate structure located further to the north of the terminus of the Nootka Sequence fault (Figure 3.9a). This intraplate slab tear, together with the lateral shortening of the subducted ExP slab as depicted by the geometry of the Nootka Sequence fault, probably manifests the internal deformation between the northern and southern segments of the subducted ExP in response to the margin-parallel indentation of the JdF plate from the south (Hutchinson et al., 2019; Savard et al., 2020). This revised model is also more compatible with the inference that the subducted ExP may be severely deformed and fragmented (Long, 2016).

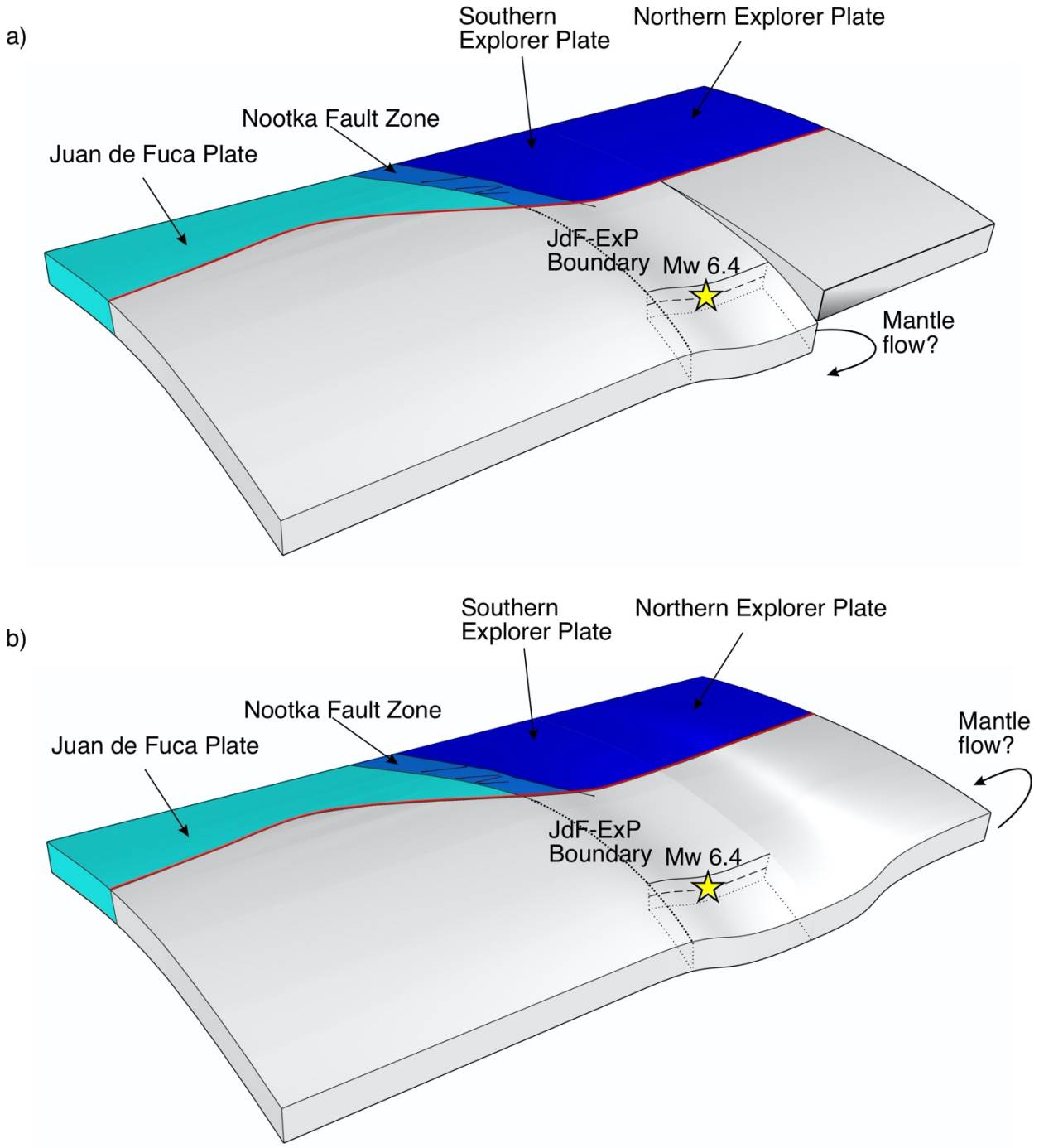

Figure 3.9. Illustrative diagrams of the two proposed plate geometries for the northern extent of the Explorer plate. The bend on the Explorer plate is based on the hypocenter distribution observed from the 2014 Nootka Sequence. The bold dashed line passing through the M_W 6.4 event represents the Nootka Sequence. Note that the Cascadia subduction front is delineated by the red line. A) Model scenario where mantle flow around the slab edge is initiated by a slab tear between southern and northern portions of the ExP. Mantle flow could drive down the southern ExP, leading to the observed hypocenter distribution from the Nootka Sequence, while uplifting the northern ExP. B) Model scenario where mantle flow around the slab edge occurs further to the north. Mantle flow could uplift the northern ExP, leading to shortening and buckling of the subducting plate north of the NFZ.

Since we did not find any evidence for a tear boundary in our study area, a simpler alternative slab geomorphology model is to have a continuously deformed oceanic plate northwest of the Nootka Sequence fault that connects to the shallowly dipping northern ExP segment (Figure 3.9b). In this case, the margin-parallel mantle flow probably originates from the northernmost edge of the subducted slab (e.g, Audet et al., 2008) or from a slab tear located farther downdip beneath the northern Cascadia arc (e.g., Mullen and Weis, 2015). Unfortunately, our results cannot substantiate either scenario. Future research efforts on the detailed slab morphology beneath the northern Cascadia arc are required to provide additional insight into this issue.

3.6 Discussion and Conclusion

The SeaJade II experiment has allowed us to delineate the complex seismogenic pattern and the corresponding interaction between the oceanic JdF and ExP at an unprecedented resolution. Using the results of the SeaJade I study (Hutchinson et al., 2019) as boundary conditions, we are, for the first time, able to image the detailed geometry of the subducted oceanic crust and uppermost mantle across the JdF-ExP boundary zone. Based on the 3D distribution of the 2014 Nootka earthquake sequence, our study suggests that the southern, subducted portion of the ExP immediately adjacent to the northernmost JdF slab has been bent sharply, potentially leading to tearing of the oceanic slab within the ExP farther to the northwest (Figure 3.9a).

Our conclusion of a severely deformed subducted ExP is qualitatively consistent with its overall weak mechanical strength toward the northern terminus of the Cascadia margin. The northern ExP segment, defined as the portion between Brooks Peninsula and the Nootka Sequence fault (Figure 3.1), is stretched with a smaller dip (Audet et al., 2008). Further to the north, the Winona block is both young (1-5 Ma) and has been proposed by some to be too buoyant to subduct (Clowes et al., 1981; Davis and Riddihough, 1982; Riddihough et al., 1980).

As the ExP undergoes severe deformation, fragmentation and break-up of the subducting slab is highly possible. Margin-parallel mantle flow, as inferred from both seismic and geochemical observations (Mosher et al., 2014; Mullen and Weis, 2015), is likely one of the consequences of

slab tearing downdip of the subduction front. This scenario is analogous to the subducted Cocos plate beneath the NAm in central Mexico, where the transition between the southern and northern segments of the Cocos slab is characterized by a sharp dip increase across the Orozco fracture zone. This sharp dip increase is interpreted as a possible slab tear that facilitates margin-parallel mantle flow (Dougherty et al., 2012; Stubailo, 2015).

The complex pattern of focal mechanisms shown in Figures 3.5 and 3.6 is also quantitatively consistent with the dramatic slab geomorphology inferred from the hypocenter distribution. The combined effects of bending/unbending of the oceanic plate along both the margin-normal and margin-parallel directions, plus the possible internal deformation within the young and warm ExP slab help to explain the close proximity of different types of faulting in both segments of the Nootka Sequence.

Intraslab earthquakes are not uncommon in Cascadia. A detailed analysis of the source characteristics of the 2001 Nisqually earthquake indicates that the sub-vertical rupture probably extends ~10 km from the oceanic Moho into the uppermost mantle (Kao et al., 2008), similar to our observation for the 2014 Nootka Sequence. What makes the Nootka Sequence unique is the concentrated, planar occurrence of aftershocks within the overriding plate that appears to be an upward extension of the intraslab rupture (i.e., the Nootka Sequence fault) across the plate interface (Figure 3.6). The relatively aseismic behavior of the subducted oceanic ExP crust in the Nootka Sequence source zone (Figure 3.7) is consistent with the temperature range of 350–400°C inferred from the regional thermal model (Gao et al., 2017). However, the development of a fault zone within the overriding plate in response to intraslab faulting is at odds with the constant relative motion across the interface thrust zone. One possible explanation is the combined effect of the very slow convergence rate between the ExP and NAm plates (Braunmiller and Nabelek, 2002) and the frequent occurrence of *M* 6+ intraslab earthquakes in the downdip portion of the NFZ. The repeated stress perturbation limited to a finite width (<5 km) over a time window of thousands of years probably has created a weak zone within the overriding plate to host shallow aftershocks.

Geometric variation of the ExP can have important implications for the rupturing and propagation of megathrust earthquakes in the CSZ. Several authors have studied the effects of changes in slab geometry on megathrust rupture propagation. For example, Lu and Wyss (1996) and Von Huene et al. (1999) find that fracture zones, such as the Adak, Amlia, and Aja fracture zones in the Aleutian arc, could act as zones of weakness through which stress cannot be fully transmitted. Similarly, subducted seamounts (Wang and Bilek, 2011; Yang et al., 2013) and ridges (Park et al., 2004) can potentially act as barriers. In all of the reported cases, significant along-strike geometric anomalies of the subduction interface are considered a key factor. Based on this analogy, we infer that the sudden change of the slab geometry across the JdF-ExP boundary may significantly reduce the likeliness of rupture propagating southward into the JdF from megathrust earthquakes originating within the ExP and vice versa. Further support for this conclusion is provided by the significant decrease in the number of earthquakes observed within the overriding plate from the southeast segment toward the northwest (Figure 3.7), which strongly implies decoupling of ExP from NAm. Possible intraslab tearing between the southern and the northern segments of the subducted ExP could also act as an additional barrier against the megathrust propagation. Therefore, our results may impose new constraints on the maximum distance and magnitude of Cascadia megathrust events. The effective maximum size of megathrust earthquakes can, in turn, contribute to a better regional tsunami hazard assessment, such as the tsunami generation models presented by Gao et al. (2017).

3.7 Supplementary Materials

3.7.1 Estimation of Hypocenter Uncertainty

We determined mean major, minor, and depth axes for each event via bootstrap resampling 80% of the original picks with 500 trials. For the earthquakes that occurred as part of the Nootka Sequence, the uncertainty of the mean major and minor ellipse axes and depth were found to be 3.14, 1.40, and 5.7 km, respectively.

In order to calculate epicentral uncertainties for TomoDD, we subset two groups of events and solved for their hypocenters with singular value decomposition, as opposed to the LSQR

method (Paige and Saunders, 1982) which underestimates uncertainty. The subsets of events were chosen from the northern and southern terminuses of the Nootka rupture zone, with 116 and 120 events, respectively. When compared to the epicentral uncertainties of the original locations, the relocations show an improvement in depth uncertainty by a factor of 6-22 and horizontal uncertainty by a factor of 2-30. At the northern terminus of the Nootka rupture zone, we calculated an average horizontal uncertainty of 0.7 km and an average depth uncertainty of 1.2 km, while we found the average horizontal and depth uncertainties for the southern terminus to be 0.12 and 0.15 km, respectively. The increasing uncertainty toward the north is reflective of decreasing station coverage.

3.7.2 Verification of Source Depths for Two Representative Events

We first calculated predicted travel-times for the *P*- and *S*- phases at the closest stations to each event at their respective depths using the original 1-D velocity model derived from Spence et al. (1985). These calculations were performed with the TauP (Buland and Chapman, 1983; Crotwell et al., 1999) module of the Obspy Python package (Krischer et al., 2015; Megies et al., 2011; Wassermann et al., 2010). We then calculated predicted travel-times for incorrect depths, e.g. a shallower depth of 23.84 km for event no. 74 vs the original calculated depth of 33.05 km. For the closest station to each event, we calculated separate origin times for the correct and incorrect depths so that the predicted *P* arrivals would occur concurrently with the observed *P* arrivals. We then applied a time correction to the *S*-phases. For subsequent, more distant, stations, we calculated the arrival times for the *P*- and *S*-phases of the correct and incorrect depths using the origin times determined from the closest station and applied station corrections to account for the complex 3d velocity structure of the region.

Chapter 4 Shallow tomographic imaging and hypocenter distribution of the Nootka fault zone and the subducting Juan de Fuca/Explorer plate in northern Cascadia as revealed by SeaJade II

Chapter 4 focuses on further refining delineation of the Nootka fault zone and tomographic imaging of the shallow subducted Explorer plate. The main body of this chapter consists of the first draft of a manuscript in preparation for submission to a peer-reviewed journal, and so this chapter is formatted specifically for this publication. By utilizing earthquake hypocenter distributions, focal mechanisms, and seismic tomography, this study further examines the Nootka fault zone and shallow subducting Juan de Fuca and Explorer plates. Hypocenters reveal possible paleo-boundaries for the Nootka fault zone, while seismic tomography further supports observations of a geometrically deformed Explorer plate. Section 4.1 provides article information. Subsequent sections (4.2-4.6) present the article in full.

4.1 Article Information

4.1.1 Author and Coauthor Contributions

This chapter consists of a manuscript to be submitted to a peer-reviewed journal. The author of this dissertation, J. Hutchinson, carried out hypocenter relocations, double-difference tomography, statistical analysis, and focal mechanism calculations. Coauthor H. Kao and J. Hutchinson jointly designed and wrote most of the study. Coauthor M. Riedel was the Chief Scientist collecting OBS data for SeaJade II. Coauthor K. Obana provided initial phase picks and hypocenters for earthquakes. Coauthors K. Wang and S. Kodaira led the SeaJade project. Coauthors T. Tsutomo and Y. Yamamoto acquired data for SeaJade II. All coauthors provided useful feedback and contributions for refinement of the article.

4.1.2 Citation

Hutchinson, J., H. Kao, M. Riedel, K. Obana, K. Wang, S. Kodaira, T. Takahashi, and Y. Yamamoto, Shallow tomographic imaging and hypocenter distribution of the Nootka fault zone and the

subducting Juan de Fuca/Explorer plate in northern Cascadia as revealed by SeaJade II, *Journal of Geophysical Research*, in preparation.

4.1.3 Author's Names and Affiliations

Jesse Hutchinson[1], Honn Kao[1,2], Michael Riedel[3], Koichiro Obana[4], Kelin Wang[1,2], Shuichi Kodaira[4], Tsutomo Takahashi[4], and Yojiro Yamamoto[4]

[1] School of Earth and Ocean Sciences, University of Victoria, Victoria, BC, V8P 5C2, Canada

[2] Pacific Geoscience Centre, Geological Survey of Canada, Natural Resources Canada, Sidney, BC, V8L 4B2, Canada

[3] GEOMAR Helmholtz-Centre for Ocean Research Kiel, Kiel, Germany

[4] Japan Agency for Marine-Earth Science and Technology (JAMSTEC), Yokohama, Japan

4.1.4 Data and Resources

Seismograms used in this study were collected as part of the SeaJade II (Seafloor Earthquake Array – Japan Canada Cascadia Experiment) project. Arrival data, relocated hypocenters, focal mechanisms, *P*-wave tomography, and *S*-wave tomography can be found in Appendix Tables A.3, A.4, B.2, C.3, and C.4. Waveform data can be obtained from JAMSTEC upon request.

The Natural Resources Canada - Earthquakes Canada database was searched using http://www.earthquakescanada.nrcan.gc.ca/stndon/NEDB-BNDS/bulletin-en.php.

Some plots were made using the Generic Mapping Tools version 5.4.2 (http://gmt.soest.hawaii.edu/; Wessel and Smith 1998).

Global Multi-Resolution Topography (GMRT) was used to generate high resolution topography and bathymetry for GMT maps (Ryan et al., 2009).

4.2 Abstract

At the northern extent of the Cascadia subduction zone, the subducting Explorer and Juan de Fuca plates interact across a translational deformation zone, known as the Nootka fault zone (NFZ). The second phase of the Seafloor Earthquake Array Japan Canada Cascadia Experiment (SeaJade II) consisted of combined recordings for nine months of ocean-bottom and land-based seismometer data. Double-difference hypocenter relocations have led to the discovery of additional seismogenic features, including lineations to the southeast of the NFZ and east of the subduction front, which resemble the currently active faults, only less mature and rotated 15° clockwise. These features may represent the paleo-configuration of the Nootka fault zone from ~3.5 Ma, which would have rotated and subducted during the reconfiguration of the Explorer plate since the capture of the Winona block. With the rupture of a M_W 6.4 earthquake and subsequent aftershocks along a previously unknown fault, known as the Nootka Sequence, seismic tomography reveals the geometry of the shallow subducting Explorer plate. Hundreds of high-quality focal mechanism solutions were determined from the SeaJade II ocean-bottom seismometer data. The mechanisms express a complex regional tectonic state, with normal faulting of the Explorer plate west of the Nootka fault zone, left-lateral strike slip behaviour of the Nootka fault zone, and antithetic thrust faulting above the subduction interface of the Juan de Fuca plate.

4.3 Introduction

The Cascadia subduction zone (CSZ) is an unusually quiescent tectonic margin. It is defined by the subduction of the Explorer (ExP), Juan de Fuca (JdF), and Gorda plates, formerly parts of the Farallon plate, beneath the western margin of the North America plate (NAm) from northern Vancouver Island to northern California (Atwater, 1970). The CSZ is capable of producing M_W 9+ earthquakes, the last of which occurred during 1700 AD (Atwater, 2005; Leonard et al., 2010; Satake, 2003). Recent research, such as the Cascadia Initiative (Toomey et al., 2014), has focused primarily on studying the JdF with ocean-bottom seismometers (OBS). Few experiments, however, have focused on the ExP.

The Seafloor Earthquake Array Japan Canada Cascadia Experiment (SeaJade) is one such experiment, designed to monitor the shallow Cascadia subduction interface at the transition zone between the subducting Juan de Fuca and Explorer plates, known as the Nootka fault zone (NFZ). Thirty-five ocean-bottom seismometer were deployed off the west coast of Vancouver Island, Canada in two phases from 2010 to 2014.

Data from the first deployment was recorded for three months in 2010 (July - September). This experiment allowed for the delineation of the Nootka fault zone. The NFZ is bounded to the north and south by two primary faults that run roughly NE-SW, between which lie several less well-developed sub-perpendicular conjugate faults. SeaJade I also provided some insight into the depths to velocity-contrasting interfaces, such as the oceanic Moho, within the subducting plate. It was found that the oceanic crust is approximately 7 km thick near the subduction front (Hutchinson et al., 2019).

The second deployment recorded data for nine months, beginning in January 2014. Several stations were placed further north of the NFZ than during SeaJade I in order to allow for a comprehensive analysis of the NFZ. During the same time, land seismometers were deployed in the Nootka sound region on the coast of Vancouver Island to accompany the OBS network (Figure 4.1).

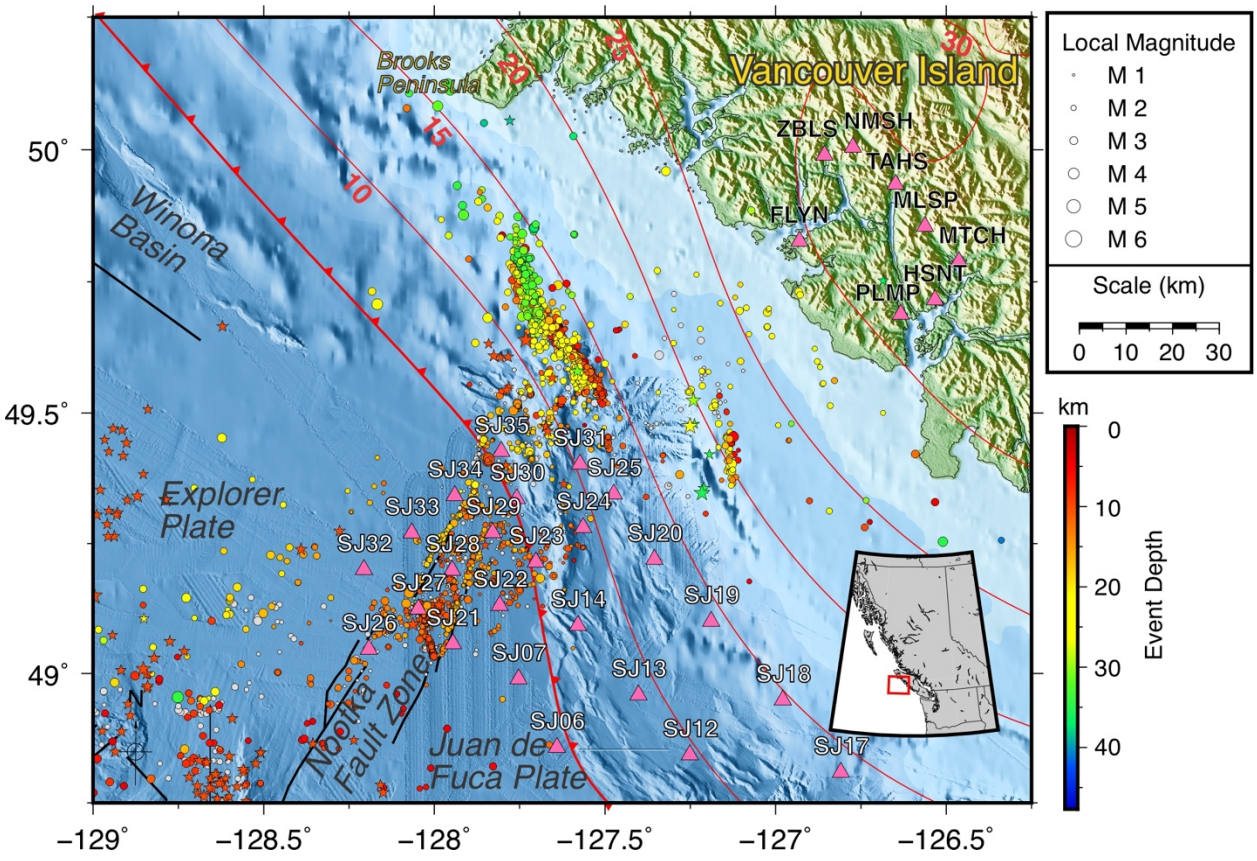

Figure 4.1. Map of the study area of SeaJade II and the Nootka fault zone. The inset in the lower-right shows the western coastline of North America with a focus on British Columbia and Washington state. The study area is indicated by the red rectangle. Within the primary map, the locations of earthquakes from the previous SeaJade I study are shown as filled gray circles. Earthquakes from the current study are shown as circles filled with colour, which is dependent on depth. Historical earthquakes exceeding magnitudes >= 4 are shown as colour-filled stars (Earthquakes Canada). Circle and star sizes are indicative of earthquake magnitude. Stations from both the ocean-bottom and land components of SeaJade II are shown as pink triangles. The subduction front of the Cascadia subduction zone is indicated by the curving red line running from northwest to southeast with triangular teeth pointing in the direction of subduction (Audet et al., 2010). The thinner red lines are 5 km contours, which deepen toward the northeast.

The dataset from SeaJade II is the central focus of this analysis. Our previous study of SeaJade II data focused primarily on the M_W 6.4 earthquake that occurred on 24 April 2014 and the associated aftershocks, known as the Nootka Sequence (Chapter 3). From these results, we were able to determine that a subducted fault within the downgoing Explorer plate was ruptured by this event. The hypocenter distribution of the Nootka Sequence has revealed that the subducting plate is bending downward to the northwest, nearly perpendicular to the direction of subduction.

Among the objectives for SeaJade II, one of the most important is in defining the plate geometry of the shallow Juan de Fuca and Explorer plates. The results show that the Nootka fault zone not only marks a change in subduction rate and plate motion vectors, but it also marks a transition from more shallowly dipping subduction to the south, to more steeply dipping subduction to the north. Substantial evidence has been provided for this change in plate geometry in the analysis of the hypocenter distribution and in the complexity of focal mechanisms. Further support can be drawn from the 3-dimensional seismic tomography obtained in this study that maps regions of low-velocities within the downgoing oceanic plates.

Additionally, the SeaJade II study highlights hypocenter lineations previously unnoticed. The tectonic significance of these seismogenic structures may reflect the paleo-orientations of the Nootka fault zone from when shear was shallower and more broadly distributed.

4.4 Methods and Data Analysis

SeaJade II was conducted in two parts: an OBS (ocean-bottom seismometer) deployment and a land-based seismic array. During October 2013, eight broadband seismometers were deployed on western Vancouver Island in the Nootka Sound region. These seismometers recorded data for approximately one year. Thirty-five short-period OBS were deployed later, during December 2013, and recorded data from January to September 2014.

Between the land and OBS components of SeaJade II, we were able to obtain high-quality seismic data to accurately locate earthquakes within the NFZ and within the subducting and overriding plates east of the Cascadia subduction front. For the entire dataset, we calculated error by bootstrapping 80% of the associated phases over 1000 iterations for each event. Upon the removal of outliers, we found the average 3-sigma values for the major, minor, and depth of the error ellipses to be 2.93, 1.17, and 4.45 km, respectively.

To better determine hypocenter locations and a suitable 3-D seismic velocity model for our study area, we utilized the TomoDD method (Zhang and Thurber, 2006). TomoDD jointly determines double-difference hypocenter solutions and inverts for 3-D velocities. The double-difference relocations are determined by utilizing travel-time differences of seismic phases (*P*

and/or *S*) and waveform cross-correlations (Waldhauser, 2001). These data allow for the relative relocation of events to one another. TomoDD also accounts for the absolute locations of hypocenters so that both the accuracy and precision of hypocenter locations are greatly improved.

The 3-D velocity model was determined for a 200-by-200 km area with 2.1 km spacing centered around 49.25° N, 127.75° W. The vertical nodes were spaced more closely, at 1 km intervals to a depth of 52 km below sea level with the exception of the shallowest node, which is placed 1.3 km above sea level. To test for the sensitivity of the velocity model to node spacing, we also performed joint inversions with horizontal node spacings of 3, 4, and 5 km. We found that low- and high-velocity structures are comparable between the different spacings; however, with larger distances between nodes the velocity outputs are coarser with more pronounced velocity highs and lows.

Double-difference relocations and joint determination of 3-D velocities and relocations were alternated between steps of iterations. In total, 78 iterations were performed to calculate the final 3-D *P*- and *S*-velocity models. Parameters used for these computations are provided in Appendix C. We also calculated V_P/V_S ratios for each grid cell by dividing the *P*-velocities by the *S*-velocities. Because we observed nearly equal numbers of *P*- and *S*-phases, and both types of phases were well-picked, we determined that this was the best method for determining the V_P/V_S ratio, unlike cases with poorer *S*-wave datasets (Eberhart-Phillips, 1990; Wagner et al., 2005; Zhang and Thurber, 2006).

We quantitatively compared the location errors before and after TomoDD. The hypocentral location error before TomoDD are estimated by the bootstrapping method described above, whereas TomoDD determines the errors by singular-value decomposition (SVD). We selected two representative subsets of events, based on different OBS coverage. The northern subset of 116 events was taken from the northwestern segment of the Nootka Sequence area (Figure 3.1, Chapter 3). The bootstrapping-determined 3-sigma values for the major, minor, and depth of the error ellipses are, on average, 3.17, 1.28 and 7.77 km, respectively. By comparison, the

average error for the X, Y, and depth axes of the error ellipses after TomoDD are 0.66, 0.67, and 1.22 km, respectively.

We selected 120 events from the southeastern segment of the Nootka sequence area where the OBS coverage was better. For this subset, we found significantly lower errors with average errors for the X, Y, and depth axes of the error ellipses of 0.10, 0.14, and 0.15 km, respectively. By comparison, the bootstrapping errors have average 3-sigma values for the major, minor, and depth of the error ellipses of 2.92, 1.22 and 3.41 km, respectively. Overall, TomoDD relocations have reduced the location error by up to an order of magnitude.

To test the resolution of our tomography model, we performed checkerboard tests with square sizes of 10, 8, 5, and 3 km in X, Y, and Z directions. We calculated synthetic travel-times for each phase using the finite-difference scheme of Hole and Zelt (1995). Checkerboard squares were set to have alternating velocities of ±5% of 5 km/s. We found that the minimum resolvable resolution was 5 km near the Nootka Sequence fault, although 3 km squares could be resolved in areas with the greatest raypath densities. The results from the 10, 8, 5, and 3 km resolution tests are shown in Figure 4.2a, b, c, and d, respectively. It should be noted that the checkerboard test results are limited due strictly to calculation only with synthetic travel-times, while our final tomography model also utilizes waveform cross-correlations.

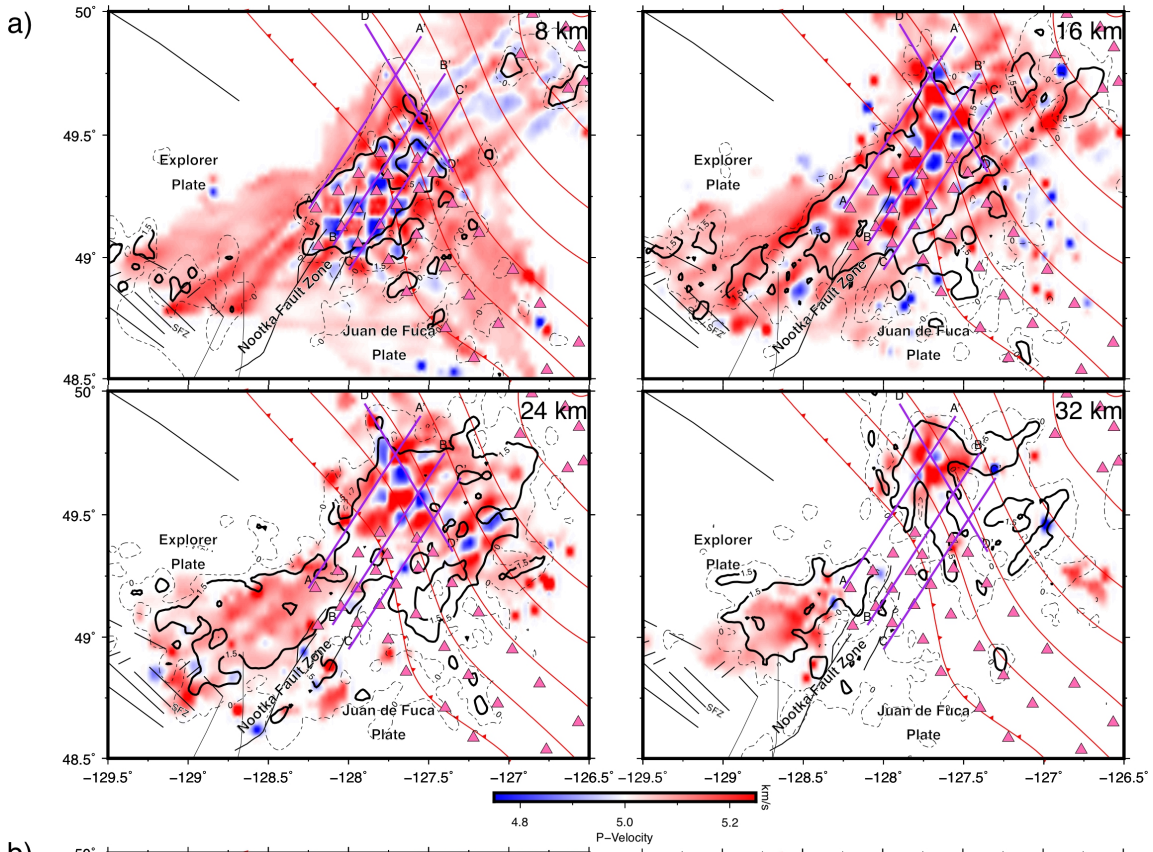
a)
8 km
16 km
24 km
32 km
Explorer Plate
Juan de Fuca Plate
Nootka Fault Zone
SFZ
A
A'
B
B'
C
C'
D
D'
50°
49.5°
49°
48.5°
−129.5°
−129°
−128.5°
−128°
−127.5°
−127°
−126.5°
4.8
5.0
5.2
km/s
P−Velocity

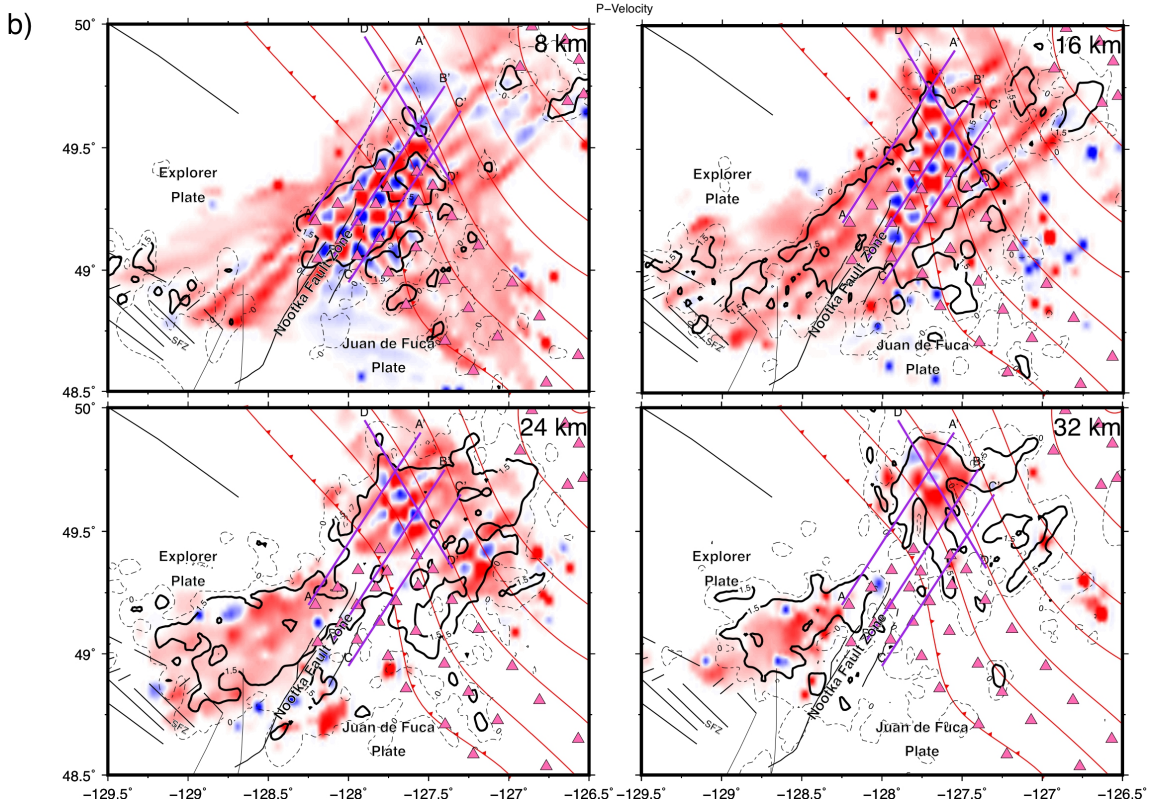
b)
8 km
16 km
24 km
32 km
Explorer Plate
Juan de Fuca Plate
Nootka Fault Zone
SFZ
A
A'
B
B'
C
C'
D
D'
50°
49.5°
49°
48.5°
−129.5°
−129°
−128.5°
−128°
−127.5°
−127°
−126.5°

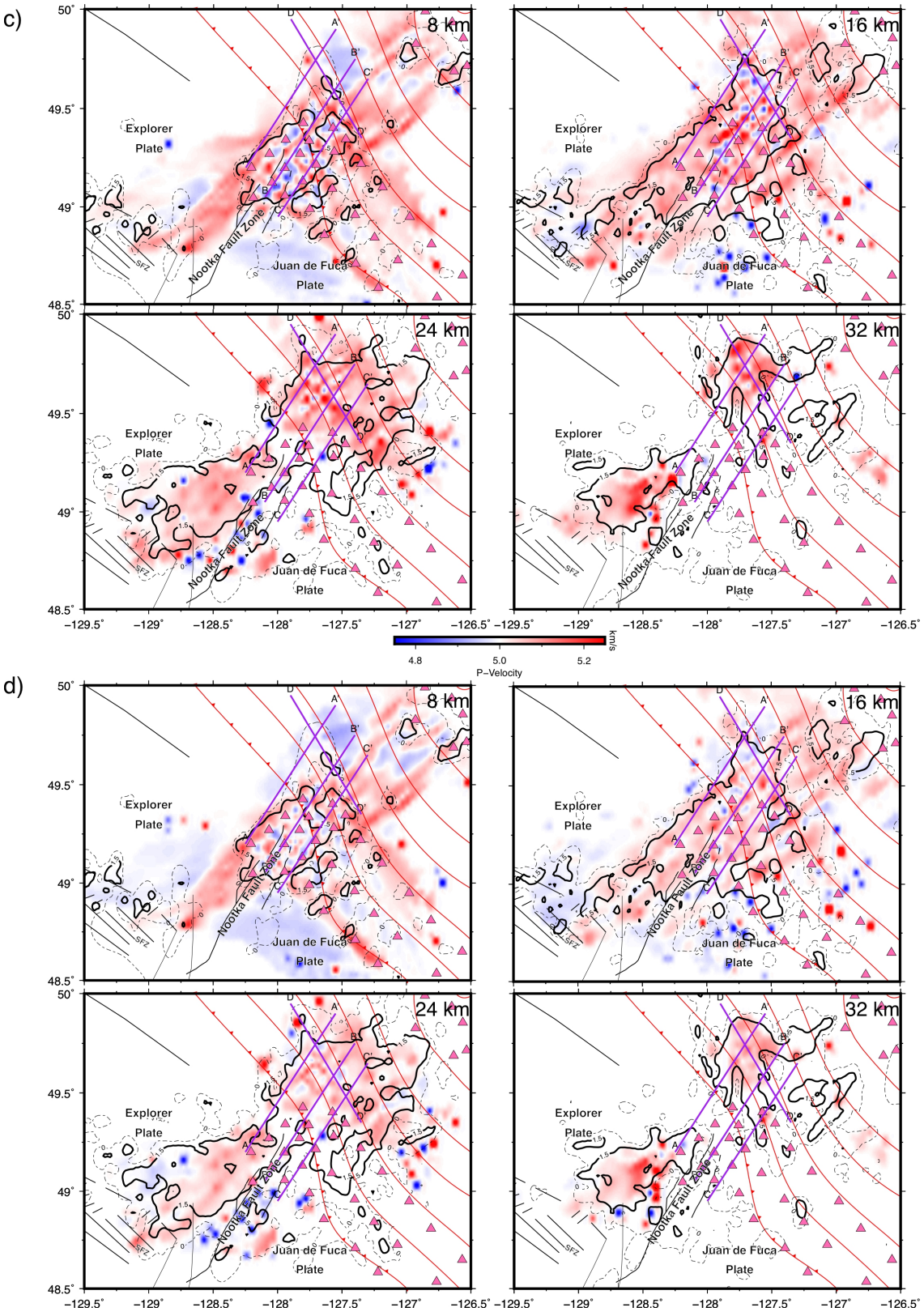

Figure 4.2. Maps of checkerboard tomography resolution tests. Tests at depths of 8, 16, 24, and 32 km are shown for resolutions of a) 10-km, b) 8-km, c) 5-km, and d) 3-km.

The derivative-weight sum (DWS) of the raypath density, as determined with TomoDD, also provides a method of determining the areas within the tomography model with the highest resolution. We calculated the base-10 logarithm for each DWS value and contoured the results in Figure 4.2. We have found that these results are consistent with the checkerboard output.

Focal mechanisms for the entire SeaJade II catalog were calculated using the program HASH (Hardebeck and Shearer, 2002, 2003). We used relocated hypocenters and the original 1-D velocity model derived from Spence et al. (1985) for our calculations. The peak displacements of *P*- and *S*-phases were used to calculate *S*/*P* ratios, which greatly improved our results. Events with 8 or more clearly identifiable first-motions were selected for calculating focal mechanism solutions (see Appendix B). We found a total of 1,564 solutions (Appendix Table B.2), of which 822 are considered A-ranked.

4.5 Results and Interpretations

We take the maximum curvature approach (Wiemer and Wyss, 2000) for determining the Gutenberg-Richter (G-R) distribution of seismicity in our study area prior to the Nootka Sequence (April 24 2014), and after the Nootka Sequence (June 1 2014) (Figure 4.3). We consider events within the bounds of 48.75-49.5° N and 127.5-129° W, roughly the area containing the NFZ. Standard deviations for G-R parameters were determined via bootstrapping 1,000 samples per test. Prior to the Nootka Sequence, *a*- and *b*-values and the magnitude of completeness (M_C) are 3.82 ± 0.17, 0.87 ± 0.08, and 1.62 ± 0.14, respectively. Following the Nootka Sequence, *a*- and *b*-values and the M_C are 3.82 ± 0.11, 0.79 ± 0.05, and 1.76 ± 0.07, respectively. These *b*-value results are very similar to what was calculated for the Nootka Sequence, which is 0.86 ± 0.07 (Section 3.5), while they are lower than the *b*-value of 1.07 ± 0.08 from SeaJade I (Hutchinson et al., 2019).

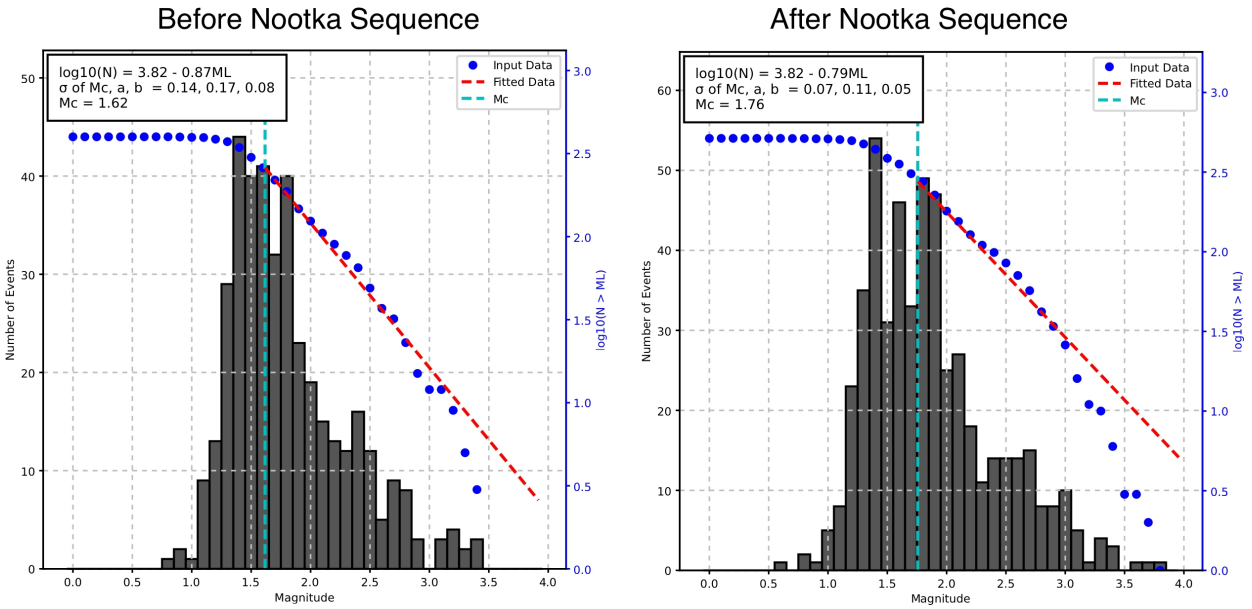

Figure 4.3. Gutenberg-Richter distributions for earthquakes within the Nootka fault zone (left) before the Nootka Sequence and (right) after the Nootka Sequence. The M_C by *b*-value stability method (Cao and Gao, 2002) was used to determine the best fit G-R distributions.

4.5.1 Hypocenter Distribution

Relocated hypocenters are shown in Figure 4.4. Seaward of the subduction front, the majority of seismicity is concentrated within the NFZ, with some diffuse epicenters in the ExP and JdF. Landward of the subduction front, most seismicity is located within the Nootka Sequence, with another, smaller concentration of events east of the southeastern terminus of the Nootka Sequence.

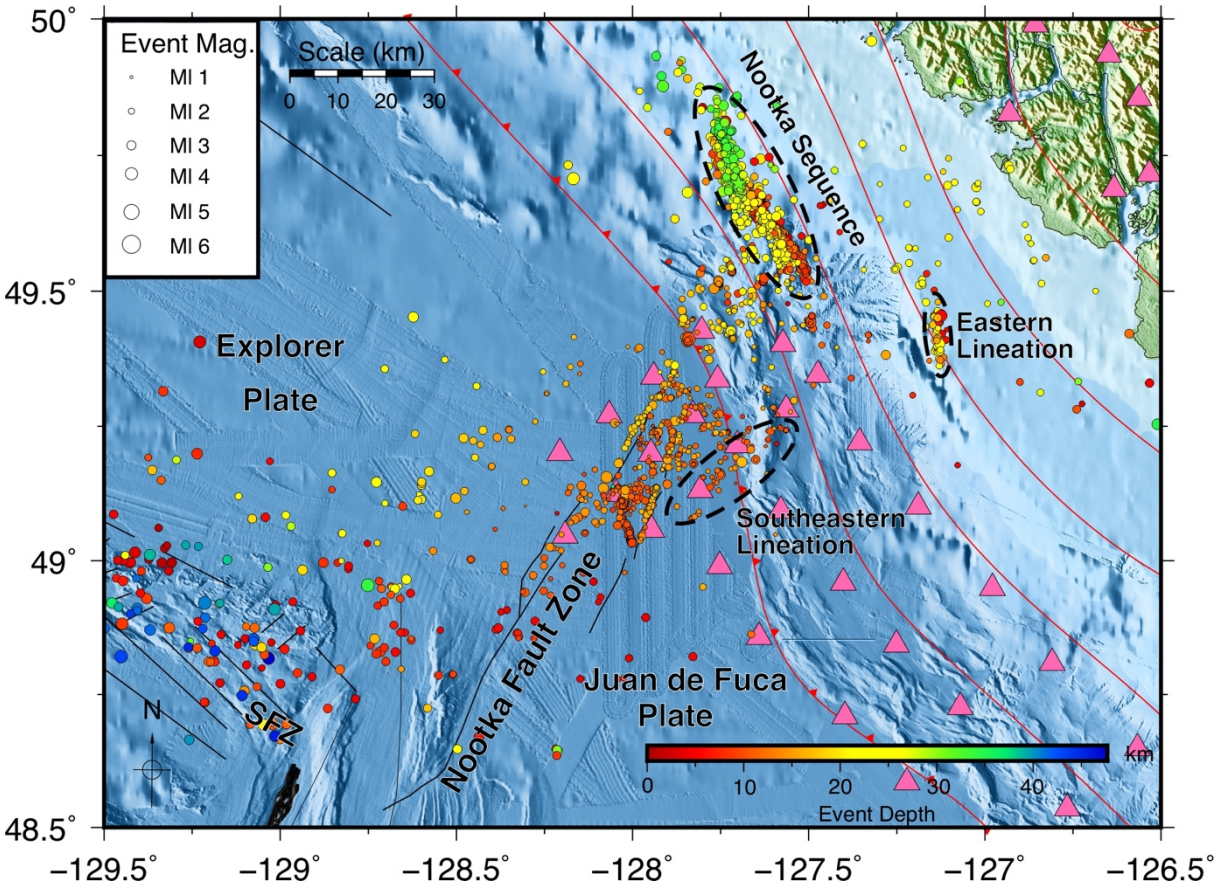

Figure 4.4. Map of the study area and hypocenters that occurred during the deployment of SeaJade II. Seismometers are indicated by pink triangles. Red lines indicate the approximate location and depths of the Cascadia subduction zone (Audet et al., 2010; Gao et al., 2017). Earthquakes relocated with the double-difference method (Waldhauser, 2001; Zhang and Thurber, 2006) are shown as circles filled with colours indicating depth and size indicating local magnitude. Several areas important to discussion are circled with dashed black lines and labelled.

As was observed from SeaJade I, the Nootka fault zone is comprised of many faults, identified as primary and secondary. These faults are represented by lineations of hypocenters, which can be seen in Figures 4.4 and 4.5. Approximate fault strike, dip, width, and length for faults are given in Table 4.1.

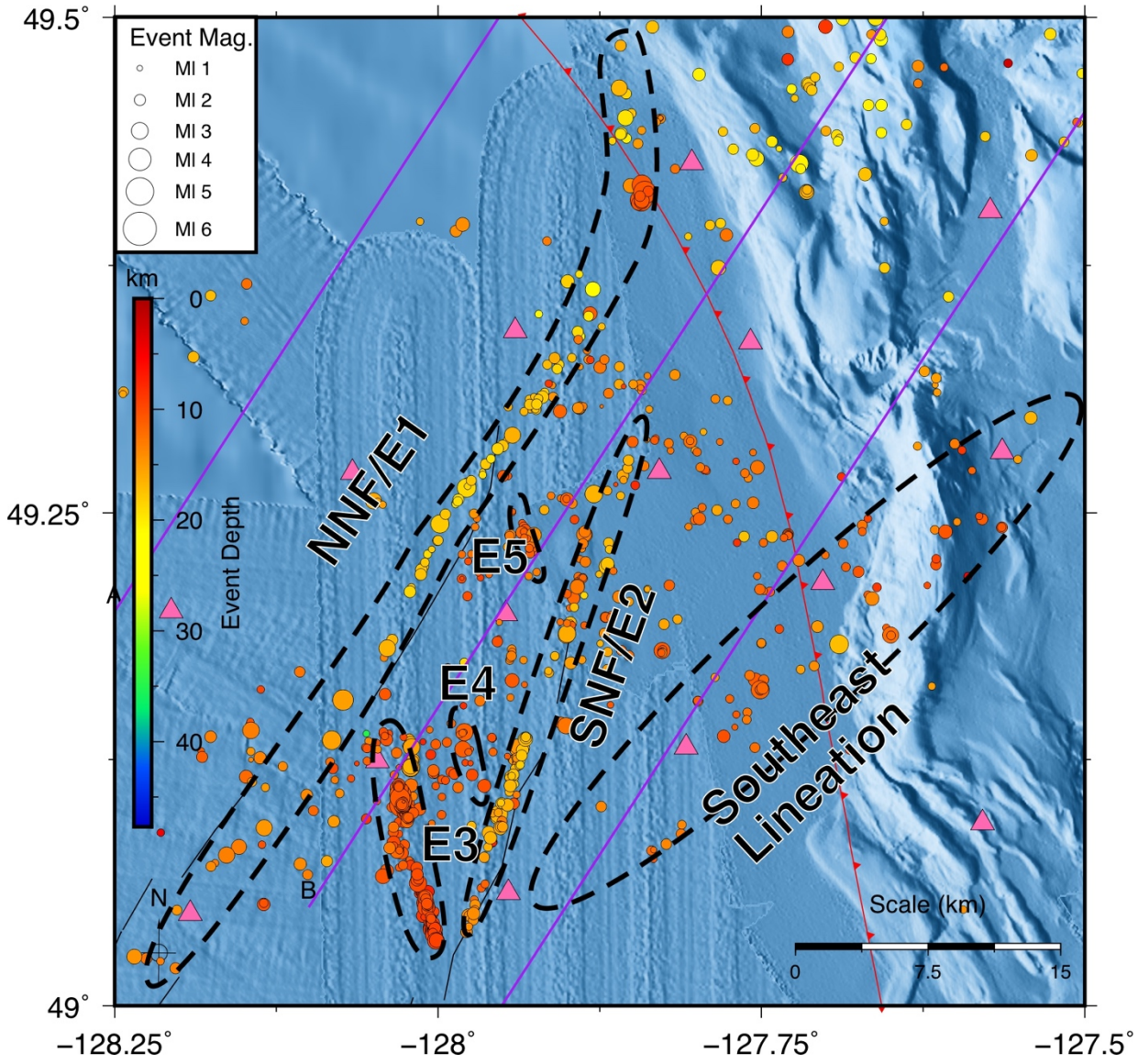

Figure 4.5. Detailed map of hypocenters focused on the Nootka fault zone. Pink triangles mark OBS. Purple lines are vertical transects shown in Figures 4.9 and 4.10. Earthquakes are shown with colour-filled circles (colour indicates depth). Seismic features, including faults and more diffuse lineations, are outlined with black dashed lines and labelled after the conventions established in Chapter 2. E1 and E2 are also labelled NNF and SNF, for northwestern and southeastern Nootka faults, after Rohr et al. (2018).

Table 4.1. Hypocenter lineations/zones and associated attributes.

Lineation/Zone	Strike	Dip	Lineation Length (km)	Lineation Width (km)	Number of Events	Earthquake Depth Range (km)	Earthquake Magnitude Range (M_L)
E1 or NNF[1,2]	32.7° ± 0.5°	71.1° ± 2.8°	55	1	~ 80	16 - 20	0.9-3.4
E2 or SNF[3]	197.5° ± 0.2°	81.2 ± 1.3	30	2	~ 100	11-19	0.9-3.2
E3	165.4° ± 0.1°	80.1° ± 0.3°	13	2	~ 450	8 – 11	0.6-4.5
E4	Too few eqs.	Too few eqs.	6	1.5			
E5	155.1° ± 2.5°	Too few eqs., appears nearly vertical	5	1.5	~20	10.5-13.5	0.8 – 2.2
Eastern Lineation	170° ± 0.9°	86.8° ± 2.8°	20	4.5	~ 30	5 - 24	1.9-3.8
Southeastern Lineation	46.6° ± 1.5°	Too Diffuse	40	7	~ 60	8-16	1.0 – 3.4
ExP	N/A	N/A	N/A	N/A	~ 80	10 - 22	0.8 – 3.4
JdF	N/A	N/A	N/A	N/A	~ 15	5 - 16	1.4 – 3.0
NW Nootka Sequence	157.3° ± 0.6°	Nearly Vertical	30	5-8	~ 610	9 – 17 (overriding), 20 – 36 (subducting)	1.6 – 6.4
SE Nootka Sequence	141.3° ± 0.4°	Nearly Vertical	40	6	~ 530	5 – 15 (overriding), 15 – 27 (subducting)	1.2 – 4.8

[1] Near to the subduction front, the NNF appears to change direction to a more northerly strike. Due to the small number of earthquakes, the strike has not been calculated.

[2] NNF is an abbreviation for the northwestern Nootka fault.

[3] SNF is an abbreviation for the southeastern Nootka fault.

Since SeaJade I, several previously undefined zones of seismicity have been observed. The Nootka Sequence fault, located approximately 20 km landward of the terminus of the NFZ and described in Chapter 3, is the most obvious of these features, extending over 60 km in length with a width of up to 6 km.

Another fault, located 25 km east of station SJ25, extends approximately 20 km in length along a more northerly trend in comparison to the Nootka Sequence fault and is labelled as the Eastern Lineation. This fault ranges in depth from 5 to 24 km and coincides with several

historical earthquakes, including a M_W 6.4 and M_W 6.3 that occurred on 19 July 2005 and 9 September 2011 (Earthquakes Canada). The occurrence of such large events near the lineation implies that it is likely a fault that has consistently reactivated and is capable of generating M_W 6+ earthquakes (Figure 4.1).

Approximately 10-12 km southeast of the southern primary fault of the NFZ, a less well-lineated feature, labelled as the Southeastern Lineation, extends for nearly 15 km before encountering the subduction front (Figure 4.5). Earthquake hypocenters continue to follow the trend of this lineation northeast of the subduction front but are less well-clustered. Because earthquakes are confined to shallower depths (extending to depths of 16 km) than the northern and southern primary faults (extending to depths of 20 km) of the NFZ and seismicity is less concentrated, we consider this fault to be less mature.

4.5.2 Seismic Tomography

The 3-D tomography indicates both low- and high-velocity anomalies, defined as regions in which *P*-velocities, calculated over 1-km depth slices, are lower or higher than the average background velocities by 2%. In Figure 4.6, depths of 8, 16, 24, and 32 km are selected in order to focus on the shallower oceanic crust and oceanic mantle seaward of the subduction front, and the deeper oceanic crust and oceanic mantle landward of the subduction front.

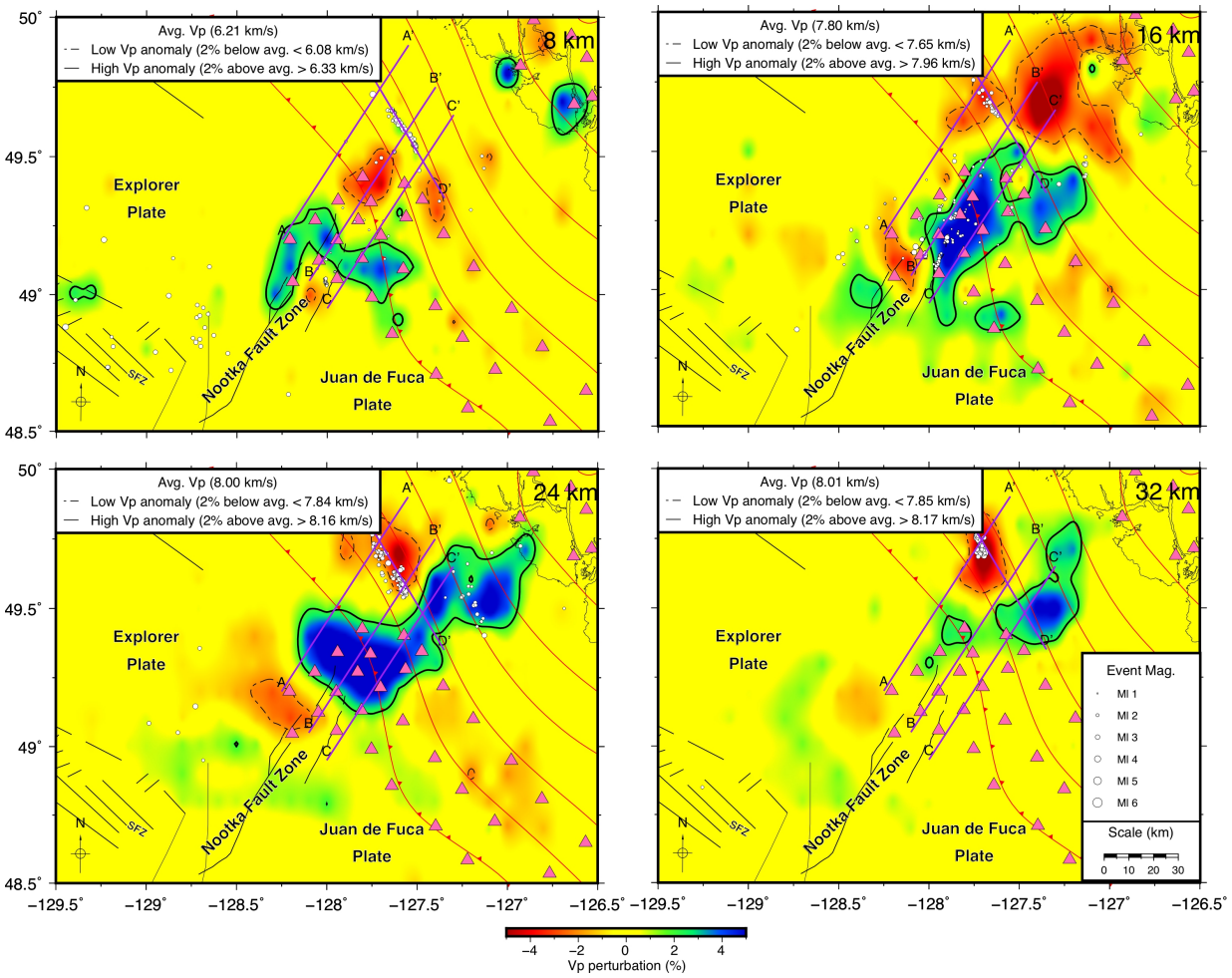

Figure 4.6. Depth slices of Vp of seismic tomography. From the upper left to the lower right, depths increase by 8 km intervals from 8-32 km. Hypocenters within a vertical distance of 1 km are shown as white-filled circles, with size indicating magnitude. Velocity anomalies are contoured where they are 2% above or below mean *P*-velocities for the depth slice. Low and high velocity anomalies are indicated by red and blue colours, as well as by dashed and solid contours, respectively. The subduction front is shown as a red line with teeth facing downdip. Subduction interface contours (Audet et al., 2010), shown as solid red lines, increase in depth toward the northeast in 5 km intervals. The purple lines show the locations of vertical cross-sections.

Landward of the subduction front, where the Nootka Sequence occurred, a low-velocity anomaly is present at a shallow depth of ~8 km at approximately 49.5° N 127.7° W and generally extends northwestward at greater depths, with the exception of localized variations, such as at the depth of 16 km (Figure 4.6). A high-velocity anomaly is adjacent to the low-velocity anomaly to the southeast. We infer that the low-velocity anomaly represents the oceanic crust of the subducting ExP, and that the high-velocity anomaly is the oceanic mantle.

At a depth of 16 km, the SeaJade I results show a continuous low-velocity anomaly within the NFZ; in SeaJade II, the low-velocity anomaly is no longer so pronounced (Figure 4.6).

The new data show that low-velocity anomalies within the southwestern NFZ and landward of the NFZ appear to be separated by a high-velocity anomaly over a distance of approximately 30 km. This high-velocity anomaly is particularly apparent at depths of 16 and 24 km (Figure 4.6). Detailed tomography maps from depths of 20 to 31 km, the presumed depth range of the oceanic Moho discussed in Chapter 3, are shown in Figure 4.7.

The discrepancies between the SeaJade I and II velocity models within and to the west of the NFZ can be explained by differences in earthquake distributions and the tomography resolution. For SeaJade II, fewer earthquakes were recorded along the northern portion of the NFZ than for SeaJade I, which could lead to a decreased data resolution in the tomography model. In this scenario, the seismic tomography seaward of the subduction front is better constrained by the SeaJade I data, while the seismic tomography landward of the subduction front is better constrained by the SeaJade II data. Alternatively, with a generally higher resolution model, the SeaJade II data may be a truer representation of seismic velocities in the region. A partial reinterpretation of NFZ structure as determined for SeaJade I would be required in this instance. I plan to resolve this question by combining SeaJade I and II dataset for a joint seismic tomography inversion in a future project.

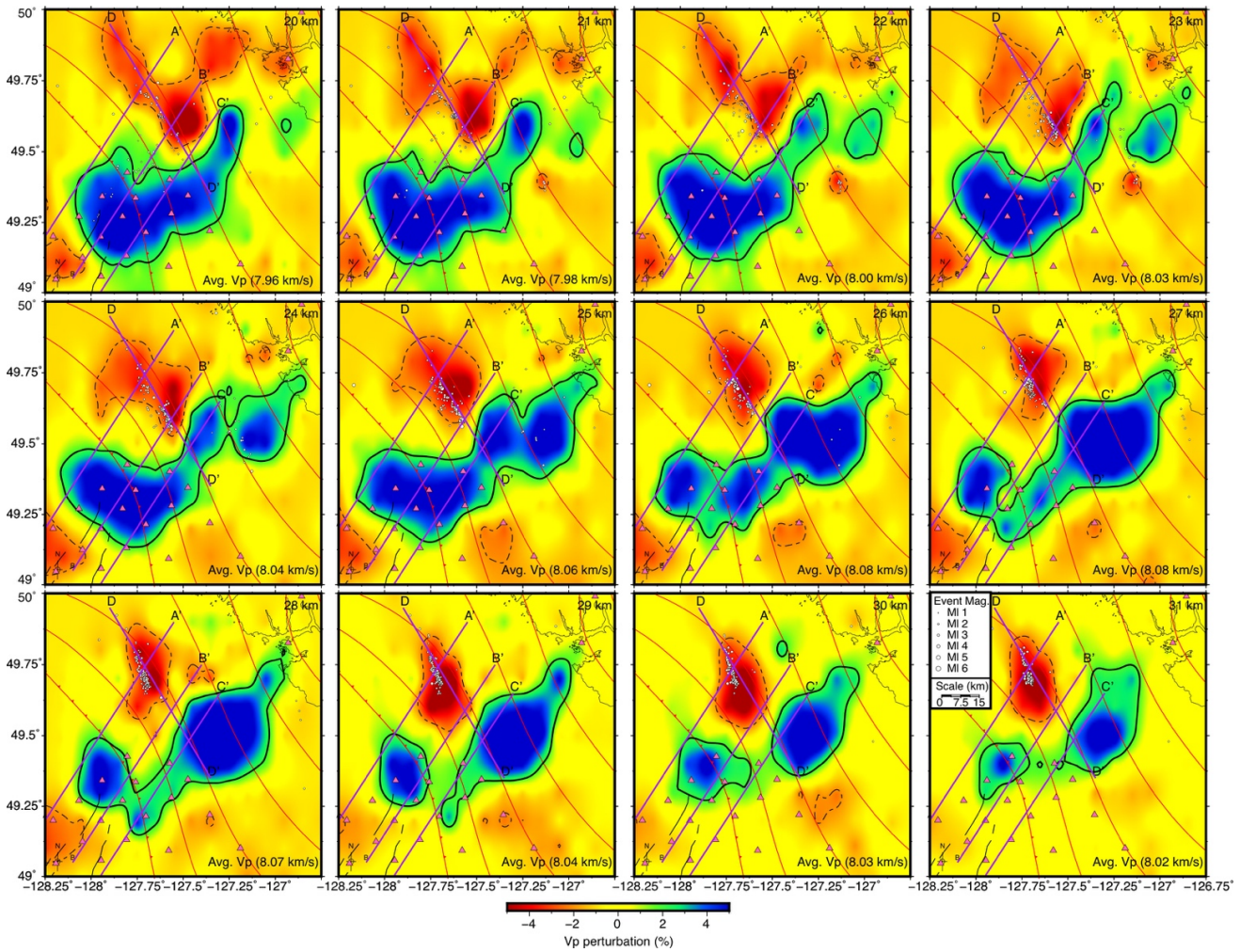

Figure 4.7. Detailed V_P seismic tomography depth slices focusing mainly on the region landward of the subduction front. From the upper left to the lower right, depths increase from 20-31 km. Hypocenters within a vertical distance of 1 km are shown as white-filled circles, with size indicating magnitude. Velocity anomalies are contoured where they are 2% above or below mean velocities for the depth slice. Low and high velocity anomalies are indicated by red and blue colours, as well as by dashed and solid contours, respectively. The subduction front is shown as a red line with teeth facing downdip. Subduction interface contours (Audet et al., 2010), shown as solid red lines, increase in depth toward the northeast in 5 km intervals. The northeastern end of the NFZ seaward of the subduction front is shown by black lines. The purple lines show the locations of vertical cross-sections.

Similar to the V_P tomography model, V_P/V_S ratios within the NFZ are higher for this study (~1.8, Figure 4.8) than what was observed for SeaJade I (~1.5, Figure 2.9) at a depth of 16 km. Around 49° N, 128.1° W we still observe low V_P/V_S anomalies with the Nootka fault zone, which coincides with the location of E3 (Figure 4.6).

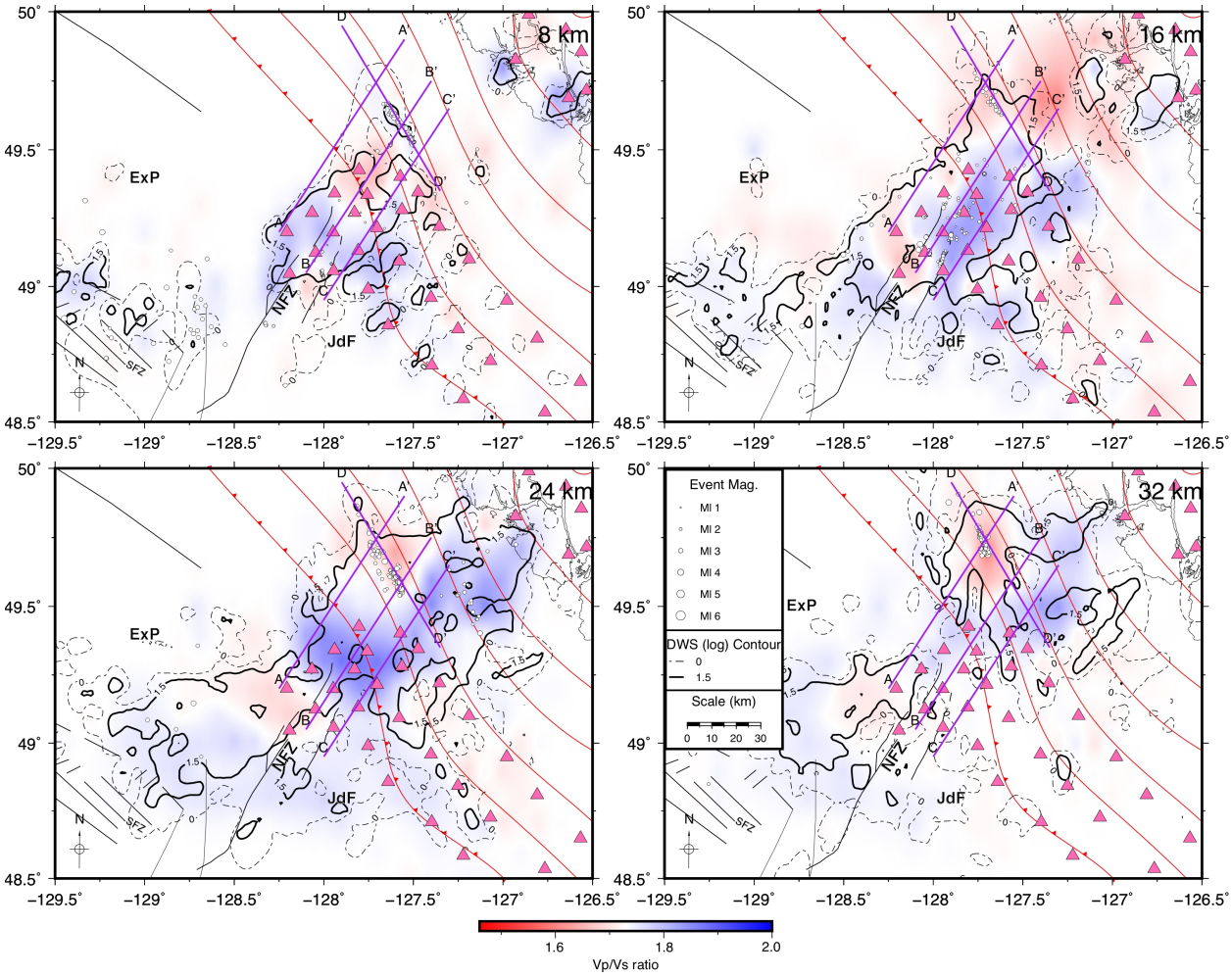

Figure 4.8. Depth slices of V_p/V_s seismic tomography . From the upper left to the lower right, depths increase by 8 km intervals from 8-32 km. V_p/V_s ratios greater than or less than 1.73 are shown as blue and red, respectively. Hypocenters within a vertical distance of 1 km are shown as white-filled circles, with size indicating magnitude. The subduction front is shown as a red line with teeth facing downdip. Subduction interface contours (Audet et al., 2010), shown as solid red lines, increase in depth toward the northeast in 5 km intervals. DWS contours illustrate areas of high raypath densities and typically indicate where the tomography is best resolved. The purple lines show the locations of vertical cross-sections.

In general, high-velocities and high V_P/V_S ratios east of the NFZ, within the Juan de Fuca plate, are consistent with our SeaJade I results (Chapter 2). Within the Explorer plate immediately west of the NFZ, seismic velocities appear to be higher than average, and V_P/V_S appears to be slightly lower (Figures 4.6 and 4.8).

Several velocity profiles illuminate a change in the subducting slab geometry, from northwest to southeast (Figure 4.9). Along the same profiles, we show derivative-weight sum contours of raypath densities (Figure 4.10), which indicate areas with the best-resolved tomography. Generally, in regions where the Vp tomography results vary the most from the initial 1-D model, raypath densities are sufficiently high to indicate that the lateral variation of seismic velocity cannot be an artefact. Orange dashed lines in Figures 4.9 and 4.10 are representative of the oceanic Moho, which is interpreted from the general increase in depth of low-velocities within the tomography model and the distribution of hypocenters. From Chapter 3, the estimated seismogenic thickness of the oceanic Moho was found to be ~5-7 km, with a high concentration of earthquakes distributed near the crust-mantle interface. The depth to the top of the oceanic crust, indicated with dashed white lines in Figures 4.9 and 4.10 is extrapolated from the orientation of the Moho and the assumed crustal thickness of ~7 to 8 km as determined in Chapter 2.

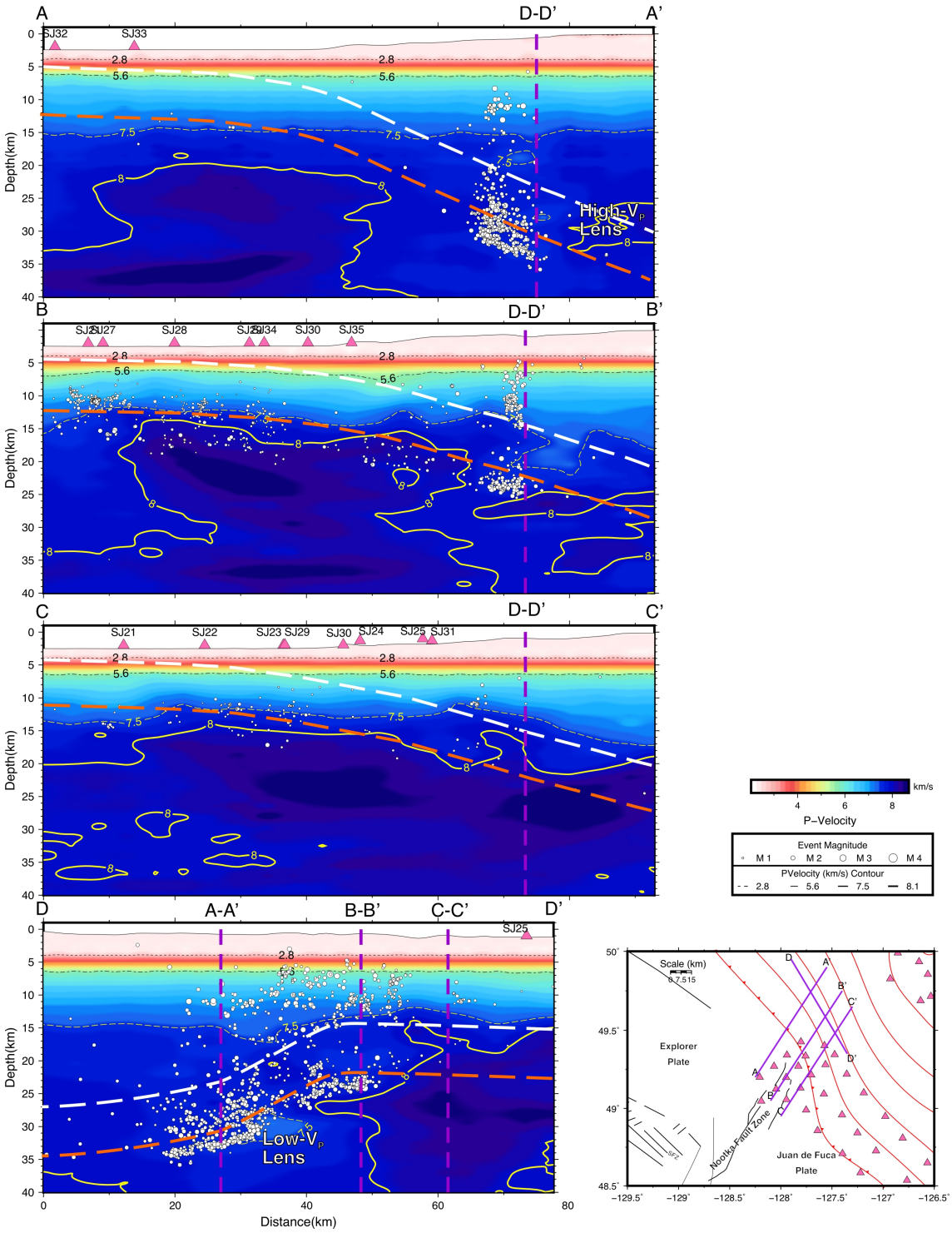

Figure 4.9. Cross-section profiles of Vp seismic tomography. Earthquakes within 5 km of the profiles are projected and marked as white-filled circles, while stations within 10 km of the profiles are marked as red triangles. Vp contours are shown as black and white dashed lines labeled with representative *P*-velocities. A reference map for the study area and the profile lines is shown in the lower right corner. Cross-section intersections are shown with purple lines and are labelled accordingly. White and orange dashed lines are representative of the inferred top of the oceanic plate and oceanic Moho, respectively.

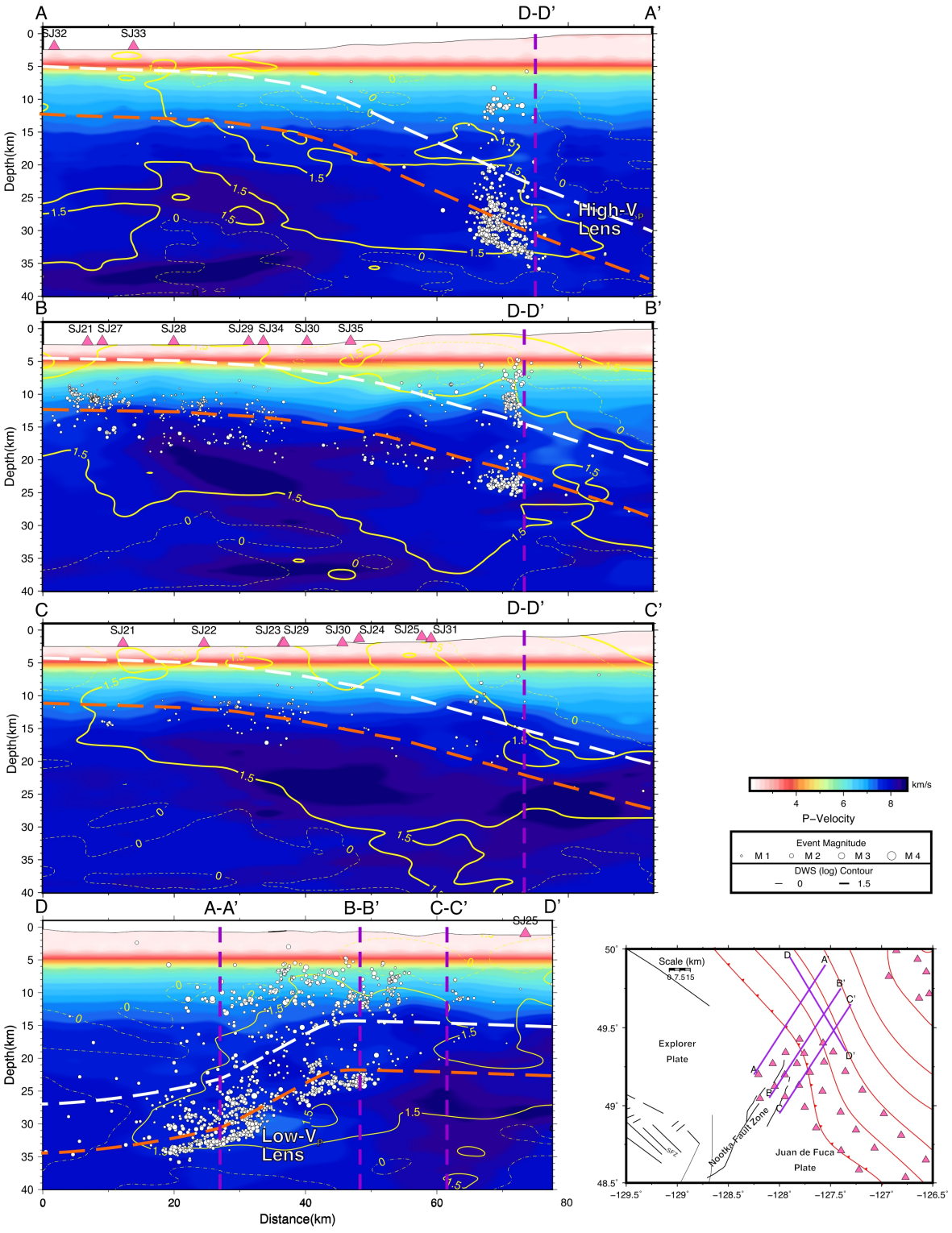

Figure 4.10. Cross-section profiles of seismic tomography with raypath density DWS contours. Earthquakes within 5 km of the profiles are projected and marked as white-filled circles, while stat within 10 km of the profile etc. [see Figure 4.9 caption]. A reference map for the study area and the profile lines is shown in the lower right corner. Cross-section intersections are shown with purple lines and are labelled accordingly.

In general, the 7.5–8.0 km/s *P*-wave velocity contours mark the transition from crust to uppermost mantle, i.e., the Moho discontinuity (Kao et al., 2013). Within the oceanic plate seaward of the subduction front, the 7.5 and 8 km/s contours are nearly horizontal, parallel, and separated by a depth interval varying from ~2 km (Profile C-C') to ~7 km (Profile A-A'; Figure 4.9). This is indicative of a nearly uniform, near-horizontal geometry for the lower crust/upper mantle seaward of the subduction front, so the transition is representative of the Moho discontinuity. However, after subduction, the 7.5 and 8 km/s contours diverge significantly. For example, along the northwesternmost profile (A-A'), located within the ExP, the slab is most likely more steeply dipping, since the 8 km/s contour goes from a depth of ~18 km to the lower limit of the tomography model at a depth 40 km (Figure 4.9). The geometry of the slab in this region is not well determined from the tomography. However, we can estimate the dip of the subducting ExP as ~23° based on the distribution of hypocenters. Northeast of the intersection of profile D-D' with A-A', a lens of high-velocity material overlies lower-velocity materials at a depth of approximately 25 km.

Within the NFZ, the velocity structure becomes more complicated on the landward side of the subduction front (profile B-B', Figure 4.9). The 7.5 km/s contour within the overriding plate appears to be deeper toward the northeast with several localized small-scale velocity variations. Similarly, the 8 km/s contour occurs at a depth of ~25 km at a model distance of 80 km along profile B-B' (Figure 4.9). Together, they are compatible with a subducted oceanic slab dipping at ~17°. Similar to profile A-A', a lens of high-velocity materials overlies lower-velocity materials at the intersection with D-D' at depths increasing from ~25 to 35 km toward B'.

Further southeast, within the JdF, the dip of the subucting slab appears to be even shallower, although it is difficult to estimate the dip of the slab without a more robust downdip hypocenter distribution. However, based on the Vp tomography (profile C-C'), the 7.5 km/s contour landward of the subduction front between the distances of 65 and 85 km shows an estimated dip of 13–15°.

Across profile D-D', seismic velocities vary drastically at depths below 15 km. Southeast of the intersection with profile B-B', V_P is generally higher than to the northwest. In particular, a lens

of low-velocity materials (< 7.5 km/s) is located approximately 30-40 km along profile D-D' at a depth of ~30 km.

Seaward of the subduction front, velocities within the NFZ are higher than the expected values of the 1-D velocity model. At the depth of ~16 km, the *P*-wave velocity generally exceeds 8 km/s (Figure 4.6). This indicates that the upper mantle is located shallower within the NFZ than in the ExP, where the *P*-wave velocity is less than 8 km/s at the same depth. We interpret the depth to the Moho within the NFZ to be ~13 km, where velocities exceed 7.5 km/s. In comparison, the oceanic crust of the ExP appears thicker (profile A-A'), potentially extending to the depth of 15 km with a less well-defined Moho than along the NFZ and JdF tomography (profiles B-B' and C-C', respectively).

4.5.3 Focal Mechanism Solutions and Implications

Focal mechanism from before, during, and after the Nootka Sequence are shown in Figure 4.11. In particular, we focus on normal mechanisms to the west of the NFZ, reverse mechanisms to the northeast of the Nootka Sequence fault, and strike-slip mechanisms along the primary and secondary faults of the NFZ.

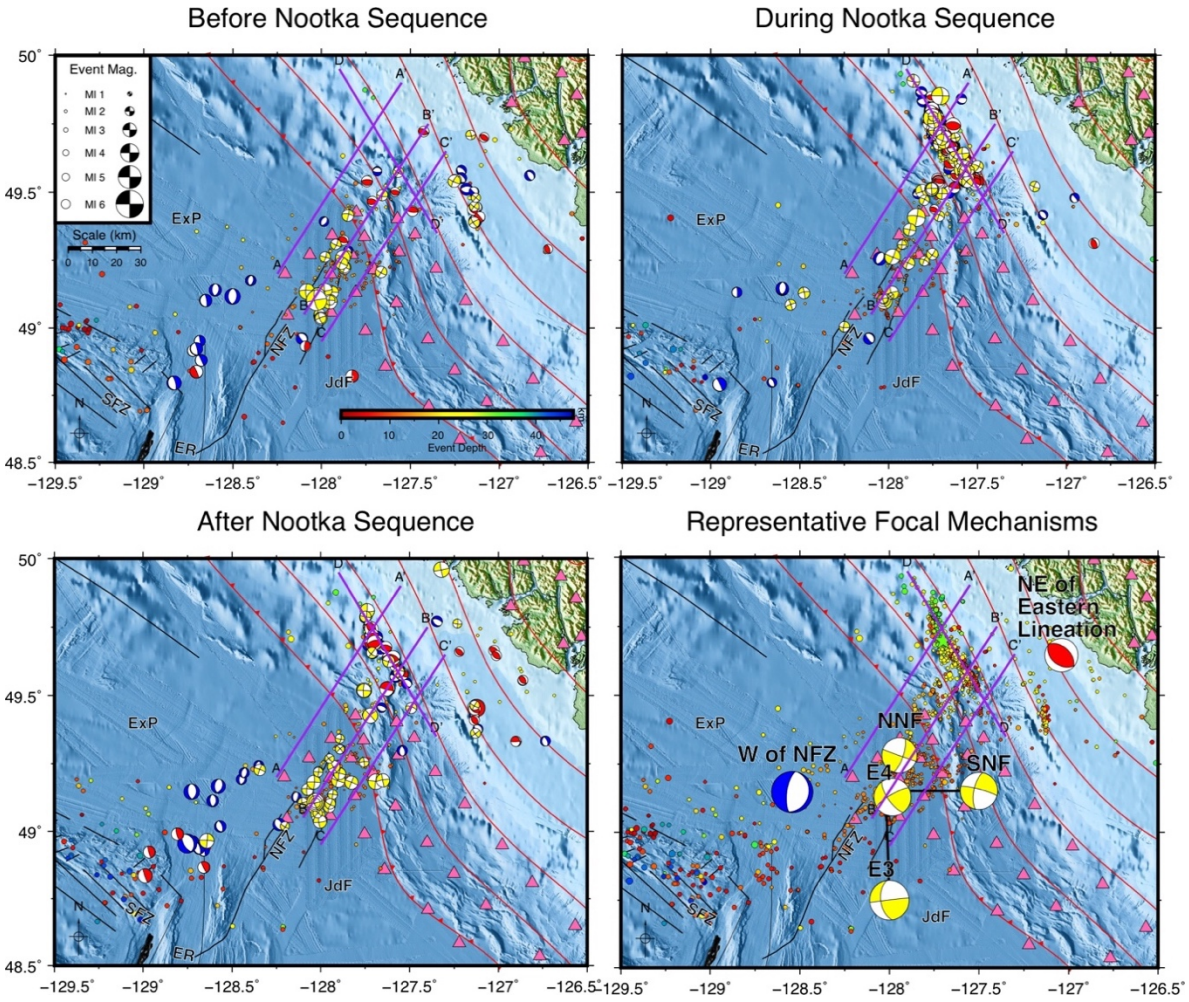

Figure 4.11. Maps of focal mechanism solutions from before (upper-left), during (upper-right), and after (lower-left) the Nootka Sequence. Representative averaged focal mechanism solutions are shown in the lower-right and are given in Table 4.2. The subduction front is shown as a red line with teeth facing downdip. Subduction interface contours (Audet et al., 2010), shown as solid red lines, increase in depth toward the northeast in 5 km intervals. The purple lines show the locations of vertical cross-sections. Earthquake hypocenters from these time periods are shown as colour-filled circles, with colour and size indicating depth and M_L, respectively. The size of the focal mechanisms is indicative of M_L while colour represents rupture type; red = reverse, blue = normal, yellow = strike-slip. Abbreviations are for the following features: ExP – Explorer plate, JdF – Juan de Fuca plate, SFZ – Sovanco fracture zone, NFZ – Nootka fault zone, ER – Explorer Ridge. Representative focal mechanisms sizes have a scale 3 times larger than the other diagrams.

Representative focal mechanism solutions for areas of interest are provided in Table 4.2 and shown in Figure 4.11. Computations were performed with code adapted from FMC (Álvarez-Gómez, 2019). First, we compute the Aki-Richards (Aki and Richards, 1980) Cartesian components of outward normal and slip vectors from the strike, dip, and rake for focal mechanisms grouped by rupture type and geographic setting. From these components, we then

calculate and average the Cartesian components of the P-, T-, and B-axes. Finally, we compute the strike, dip, and rake for representative focal mechanisms from the averaged P-, T-, and B-axis components.

Table 4.2. Representative average focal mechanism solutions for selected areas.

Zone	Strike (°)	Dip (°)	Rake (°)	Aux-Strike (°)	Aux-Dip (°)	Aux-Rake (°)	P-axis Trend (°)	P-axis Plunge (°)	T-axis Trend (°)	T-axis Plunge (°)
W of NFZ[1]	16.5	20.8	-82.4	188.3	69.4	-92.9	321.0	86.0	282.7	51.5
NE of Eastern Lineation[2]	127.0	41.0	85.2	313.3	49.2	94.1	40.3	5.8	272.0	86.0
NNF	19.3	72.2	-1.5	109.8	88.6	-162.2	323.7	15.6	255.2	14.1
SNF	191.5	67.3	-8.7	284.9	82.0	-157.1	144.7	22.7	61.4	12.0
E3	172.4	54.2	178.4	263.3	88.7	35.9	32.9	23.9	133.0	25.9
E4	145.2	69.8	167.1	239.7	77.9	20.6	23.4	10.4	89.6	23.8

[1] Located within the vicinity of 49.15° N, 128.5° W.

[2] Located within the vicinity of 49.7° N, 127° W.

The NFZ is dominated by strike-slip mechanisms both before and after the Nootka Sequence. At 49.25° N, 128° W, the approximate motion of the ExP relative to the JdF is 219.35° from north at a speed of 2.5 cm/yr using model B of Braunmiller and Nabelek (2002), resulting in pure strike-slip behaviour between the two plates. Model A has a slight oblique-extensional component with a direction of 243.12° at 2.3 cm/yr. By comparison, the average trend of the T-axes for the NNF and SNF are in directions of 255.2° and 61.4°, respectively, more compatible with model A.

Normal mechanisms west of the NFZ, within the ExP at approximately 49.15° N, 128.5° W, have strikes aligned roughly north-south. The average trend of the T-axes for the normal mechanisms is 282.7° (or 102.7°), indicating that the normal faulting cannot only be attributed to the relative motion between the ExP and JdF. In a regional context, distributed deformation in the form of Riedel shears can lead to complex rupture sequences, with normal faulting along the σ3 axis. The observed normal mechanisms are likely a result of the combined effect of Riedel shear associated with the relative motion between the ExP and JdF and locally transmitted stress from extensions along the Explorer Ridge to the south.

Reverse mechanisms located above the subduction interface to the NE of the subduction front at approximately 49.7° N, 127° W may have been produced by antithetic faults related to locking/coupling of the subducting plate with the overriding plate. The trend of the average P-axes of these focal mechanisms (40.3°) is sub-parallel to the direction of subduction for the JdF relative to the NAm (3.8 cm/yr in a direction of 60.8°), but in fact more closely matches that of the ExP (2.1 cm/yr in a direction of 42.2°).

4.6 Discussion and Conclusions

4.6.1 Northwestward Bending and Deformation of the Shallow Subducted Explorer Plate

The hypocenter distribution of the Nootka Sequence demonstrates the variation in geometry of the shallow subducted ExP (Chapter 3; Figure 3.9). Toward the northwest along the Nootka Sequence fault the depth to the oceanic Moho increases from ~22 to 24.5 km (Figure 3.7) over a distance of 25 km. The change in Moho depth indicates a significant bend in the ExP nearly perpendicular to the direction of subduction.

In this study, we observed lower-velocity materials increasing in depth from the southeast to the northwest along profile D-D' (Figure 4.9) from depths of ~15 km to greater than 30 km. This change in *P*-velocity is representative of the change in geometry of the subducting slab. The distribution of hypocenters and deep low-velocity materials are a clear indicator of northwestward bending of the shallow subducted Explorer Plate.

Past a distance of 80 km along profile A-A', a lens of high-velocity material is sandwiched between lower-velocity materials. Presumably, this lens could be mantle materials overlaying subducted slab, either the upper mantle of the overriding plate or oceanic mantle emplaced by margin-parallel flow. Shear-wave splitting analysis has indicated margin-parallel flow in this region (Mosher et al., 2014), but whether it is induced at the edge of the subducted Explorer plate further north, or by a more local intraslab tear (Figure 3.9), as has been attributed to the fragmenting Cocos plate (Stubailo, 2015), remains unknown.

A large, low-velocity anomaly at 30-40 km along profile D-D’ and a depth of ~30 km could be related to a high degree of fracturing. The bending and unbending process in the subducting plate toward the northwest is the most likely candidate for the nucleation of fractures, resulting in low *P*-velocities, not unlike the observations made for the deep low-velocity anomalies within the Nootka fault zone discussed in Section 2.6.2.

4.6.2 Evolution of the NFZ

Faults from outside of the NFZ may be representative of a time when shearing was more broadly distributed (Rohr et al., 2018). The decrease in fault length from the Nootka Sequence fault (~60 km) to that of the conjugate faults (~10 km) probably implies the NFZ has matured by changing from a more broadly distributed shear zone to a concentrated zone with well-defined bounding faults. The Nootka Sequence fault itself has also presumably matured with time, as hypocenters are located within the oceanic mantle, similar to the northern and southern primary faults, and unlike the conjugate faults within the NFZ.

A lineation southeast of the southern primary fault (Figures 4.4 and 4.5; Table 4.1) may have formed at a time when the NFZ was broader. This lineation appears rotated clockwise by approximately 14° relative to the current northern primary fault. Another lineation observed east of the Nootka Sequence (Figure 4.4; Table 4.1), landward of the subduction front, also appears rotated clockwise by approximately 15° relative to the average strike of the NFZ conjugate faults and the Nootka Sequence (155°). Davis and Riddihough (1982) have demonstrated that the Explorer Ridge migrated to the northwest with the isolation of the Winona Block from the Pacific plate from ~4 to 1 Ma. As migration occurred, clockwise rotation of the Explorer Ridge and the ExP reduced the rate of margin normal subduction.

In Figure 4.12, we present an illustrated evolution of the NFZ based on the rotation of lineations and plate reconstructions from previous authors (Braunmiller and Nábělek, 2002; Davis and Riddihough, 1982; Riddihough, 1984; Rohr et al., 2018).

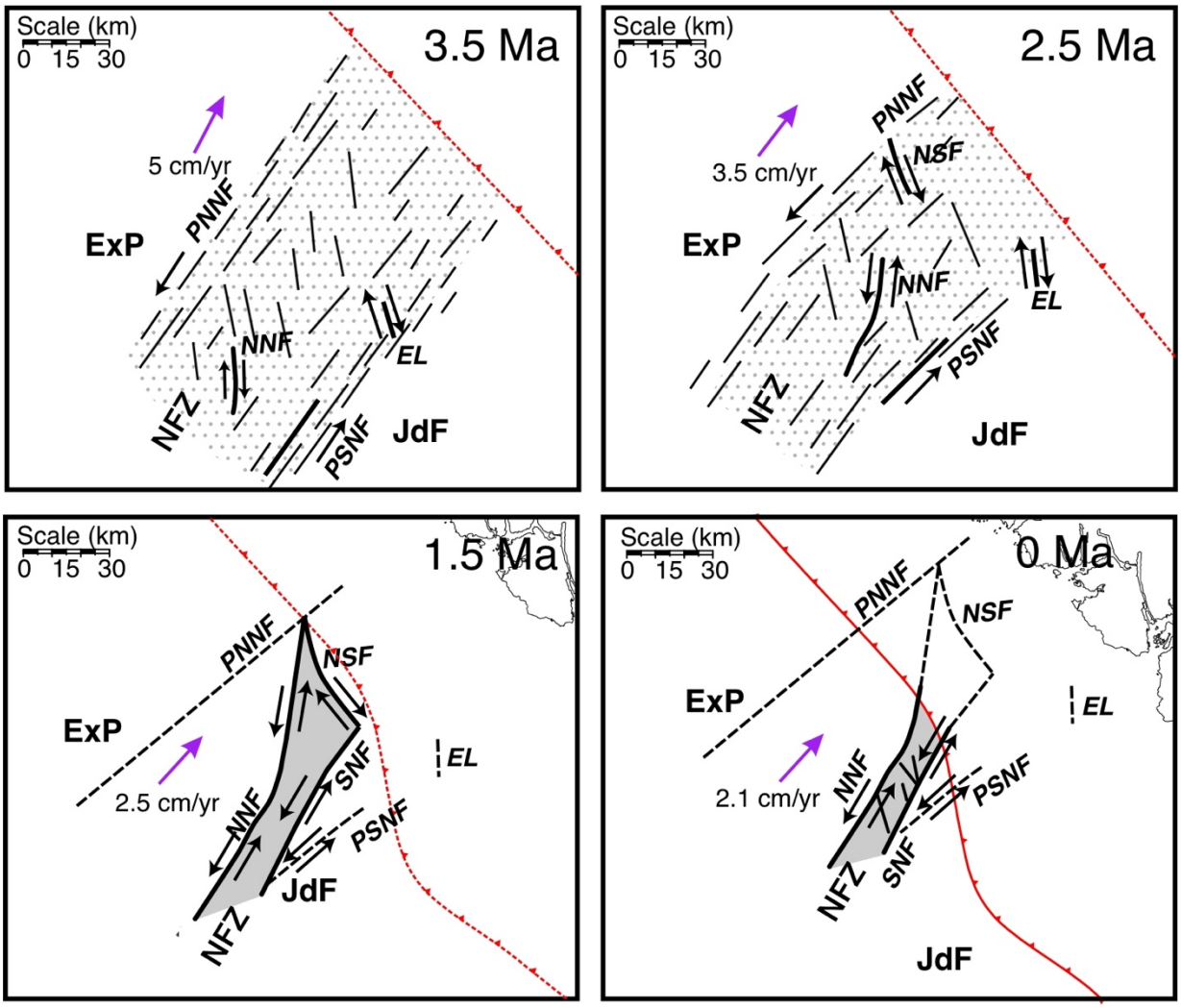

Figure 4.12. Illustrative diagram of the presumed evolution of the Nootka fault zone from 3.5 Ma (upper left) to 0 Ma (lower right). At 3.5 Ma, the Nootka fault zone begins as a region of distributed shear between the Explorer and Juan de Fuca plates. Clockwise rotation occurs between ~ 3.5 Ma and 1.5 Ma. The subduction front has presumably developed with the deposition of sediments, so the exact configuration prior to 0 Ma is unknown. Relative motions along faults are indicated by opposing black arrows. Areas of distributed shear are indicated by gray stippling. Solid gray regions indicate that shear dislocation only happens along individual faults. Purple arrows show the relative motion of the Explorer plate relative to North America. Text labels are abbreviations for the following features; ExP – Explorer plate, JdF – Juan de Fuca plate, NFZ – Nootka fault zone, PNNF – paleo-northwestern Nootka fault, SNNF – paleo-southeastern Nootka fault, NNF – northwestern Nootka fault, SNF – southeastern Nootka fault, EL – eastern lineation, NSF – Nootka Sequence fault.

3.5 Ma

At 3.5 Ma, the ExP subducts at a rate of ~ 5 cm/yr nearly perpendicular to the subduction front (Riddihough, 1984) at an orientation 15-25° counterclockwise to what is presumed today (Braunmiller and Nábělek, 2002). The exact configuration of the subduction front at this time is

unknown, so it is portrayed as a straight dashed red line. The oceanic lithosphere of the easternmost ExP is ~1 Myr old. The early NFZ formed at ~4 Ma, and at 3.5 Ma it is portrayed as a broad deformation zone with many smaller immature faults. The boundaries of the NFZ, the paleo-northwestern Nootka fault (PNNF) and paleo-southeastern Nootka fault (PSNF), are based on the maximum distance between the northern terminus of the Nootka sequence fault (NSF) and the southeastern lineation as well as the location of several strike-slip events to the northwest of the current NFZ. We have inferred that the current northern primary fault, demarcated as the northwestern Nootka fault (NNF), may have initiated as a conjugate fault during this time along with the eastern lineation, based on their paleo-orientations.

2.5 Ma

Clockwise rotation of the Pacific plate and the Explorer ridge relative to North America has led to partial breakup and capture of the Pacific plate by North America in this region. This capturing initializes the formation of the Winona block, reducing the convergence rate of the ExP (Davis and Riddihough, 1982). Due to rotation of the ExP and continued rupturing and evolution of the NFZ, we estimate that the NSF began as a conjugate fault. The NNF continues to mature and lengthen nearly parallel to the direction of the relative motion between the JdF and ExP. Subduction of the eastern lineation begins shortly before 1.5 Ma.

1.5 Ma

Further rotation of the ExP to the current azimuth led to lengthening of the NNF to the southwest. Maturation of the NFZ has led to the formation of the current SNF and lengthening of the NSF, bridging the distance between the NNF and SNF. The NNF has further lengthened toward the NSF. As plate motion is accommodated by the narrower NFZ, the PNNF and PSNF are abandoned as active boundaries of the NFZ. Subduction of the NSF begins. Further northwest, at ~1 Ma, the Winona block is isolated from the Pacific plate. The subduction front may more closely resemble the present-day configuration, but it is still portrayed with a dashed red line to account for uncertainty.

0 Ma

Orientation of paleo-faults with currently active faults indicate an average of 15° clockwise rotation. Since 3.5 Ma the NFZ has matured and narrowed. The current NNF and SNF extend well into the mantle, acting as potential conduits for hydration of mantle materials. Conjugate faults, particularly E3, have become well-developed between the NNF and SNF. The current orientations of the NNF and SNF reflect the relative motions between the ExP and JdF. As the NFZ has matured, the majority of plate motion has been accommodated by seismic slip along the primary faults (Willoughby and Hyndman, 2005). Rupturing along paleo-faults continues to occur regularly, as they were first noted during SeaJade I by Hutchinson et al. (2019), but much less frequently than the currently active faults.

4.6.3 Focal Mechanisms and Regional Tectonics

Section 4.5.3 and Table 4.2 discuss the current stress fields in the area surrounding the NFZ in relation to current regional tectonic models. The orientations of focal mechanisms from the NNF and SNF generally agree with the sense of motion between the JdF and ExP. However, plate motion vectors inadequately explain the normal mechanisms west of the NFZ and the reverse mechanisms northeast of the Nootka Sequence fault.

Normal mechanisms within the ExP to the west of the NFZ indicate a locally dominant tensional stress field. Given the contrast between subduction of the southern ExP and the apparent lack of subduction of the Winona block (Clowes et al., 1981; Davis and Riddihough, 1982; Riddihough et al., 1980), it is likely that the ExP is not acting as a single contiguous plate, or could be in the process of reconfiguration. The normal mechanisms appear to line up with the strike of the Explorer Ridge when following its trace from the south (Figure 4.11). These mechanisms can be explained by regional Riedel shearing, where the T-axes align with σ3.

Because the averaged P-axes of the reverse mechanisms are nearly identical to the sense of motion between the NAm and ExP, we propose that the northern JdF is subducting nearly 20° counterclockwise to the relative plate motions as determined with the NUVEL-1A model (DeMets et al., 1994). Brothers et al. (2020) calculated a new Euler rotation pole for the

interaction between the Pacific plate and the NAm by analysis of morphological features and reconstructions of fault offsets along the Queen Charlotte fault. They proposed that relative motions between the two plates result in almost purely strike-slip behaviour, rather than having an oblique component (DeMets and Merkouriev, 2016). If so, this demonstrates that relative plate motions for both the JdF (DeMets et al., 1994, 2010) and ExP (Braunmiller and Nábělek, 2002) may require re-evaluation, as they both depend on the interaction between the Pacific and North America plates.

Our observed focal mechanism solutions, deformation of the shallow subducted ExP, and the continuous evolution of the NFZ as determined from the distribution of faults (Rohr et al., 2018) and lineations of hypocenters are indicative of an unstable and changing tectonic regime. We propose that direct observations of the Explorer and Juan de Fuca plates in northern Cascadia, such as with ocean-bottom GPS, is required for re-evaluation of relative plate motions.

Chapter 5 Conclusions

This Ph.D. dissertation focuses on the subducting Juan de Fuca and Explorer plates of the Cascadia subduction zone, west of Vancouver Island, Canada, and the transition in between, known as the Nootka fault zone. The main contributions of this project are summarized below.

Chapter 2 focuses on the data obtained from the first phase of the Seafloor Earthquake Array Japan Canada Cascadia Experiment (SeaJade I). Thirty-three ocean-bottom seismometers (OBS) were utilized to locate over 1,200 earthquakes, which occurred mostly along the Nootka fault zone. With the application of double-difference relocation and joint tomography (Zhang and Thurber, 2006) to improve hypocenter locations, this study revealed that the two primary faults bounding the NW and SE extent of the active NFZ extended through the crust and into the mantle. Between these two primary faults, the hypocenter distributions reveal secondary conjugate faults sub-perpendicular to the primary faults, striking NNW-SSE. Shallower hypocenter distributions and less well-defined lineations indicate that the conjugate faults are less mature in comparison to the primary faults. Using seismic tomography and converted phase analyses to help constrain the depths to velocity-contrasting interfaces, we showed that the top of the oceanic plate is at a depth of ~4-6 km, the Moho is at ~11-14 km, and the dip of the slab is ~9-10° beneath the westernmost Cascadia subduction front.

In Chapter 3, I examine a M_W 6.4 earthquake that occurred on 24 April 2014 during the SeaJade II deployment. The ensuing aftershock sequence, known as the Nootka Sequence, highlights a previously unknown subducted fault within the Explorer plate. The depth distribution of hypocenters shows a significant geometric SE-NW variation of the Explorer. Over a distance of ~25 km, hypocenters within the upper mantle increase in depth from ~22 to 32 km. These results show that deformation of the southern Explorer plate is nearly dip-perpendicular. This deformation is further supported by the complex distribution of focal mechanisms. Reverse mechanisms are dominant on the inside of the plate bend, while normal mechanisms are more common along the outside of the plate bend. Normal mechanisms within the overriding plate above the southeastern Nootka Sequence fault are indicative of strong coupling with the subducting Explorer plate. Further northwest, after the downward bend in the Nootka

Sequence fault, a severe decrease of seismic activity within the overriding plate indicates weaker coupling with the subducting slab. It is possible that this bending is induced by margin-parallel mantle flow (Mosher et al., 2014).

The complete SeaJade II catalogue is presented in Chapter 4. Relocated hypocenters along the Nootka fault zone maintain consistency with the observations from SeaJade I. The longer duration of the experiment, however, has led to the discovery of possible paleo-faults delineating the former extent of the Nootka fault zone, estimated to have formed at approximately 3.5 Ma. Representative average P- and T-axes from clusters of focal mechanisms have highlighted inconsistencies in currently accepted relative plate motions when applied to detailed motions within and on either side of the NFZ. Three-dimensional V_P velocity models from seismic tomography derived from this study are generally consistent with the results from SeaJade I data (Chapter 2), but the SeaJade II data provide greater resolution and cover a greater areal extent. Specifically, the velocity structure seaward of the subduction front could be ascertained because of the distribution of events downdip of the subduction front and the addition of land-based seismometers onshore from the OBS network. The tomography results show a low-velocity structure dipping toward the northwest, which coincides with the Nootka Sequence, further supporting the argument for northwestward bending and deformation of the southern Explorer plate.

Based on these results, I infer that the deformation in the southern Explorer plate may act as a barrier to the along-strike rupture of megathrust earthquakes. Intense geometric deformation of the downgoing plate has resulted from subduction resistance by the northern Explorer plate. This study shows that a possible intraslab tear inducing margin-parallel mantle flow has led to bending of the southern Explorer plate. It is possible that these effects isolate the Explorer plate from the rest of the megathrust zone.

Together, these studies provide a comprehensive analysis of the Nootka fault zone in relation to the subducting southern Explorer plate. Nootka fault zone maturation has been proposed by Rohr et al. (2018) through analysis of seismic reflection and multibeam bathymetry data. Constraint for the tectonic evolution of the Explorer – Juan de Fuca boundary zone is derived

from the distribution and orientation of hypocenters. Broadly distributed earthquakes reveal the extent of the paleo-Nootka fault zone at an orientation approximately 15° clockwise from the currently active faults, consistent with the inferred rotation of the Explorer plate since the initiation of the Nootka fault zone ~ 4 Ma (Riddihough, 1984; Wilson, 1993). The Nootka fault zone has evolved from a region of broadly distributed shear to one of distinct primary and secondary conjugate faults. Distributed Riedel shearing is indicated by the observation of normal faulting within the Explorer plate, implying that local stresses do no strictly act on the Nootka fault zone alone.

While much about the region remains unknown, this study has contributed significantly to our understanding of northern Cascadia. The Nootka fault zone and Explorer plate are truly unique tectonic environments, providing a glimpse into the fate of oceanic plates as they are fractured and subducted. The methodology applied to this study can be used in other subduction settings in order to draw comparisons and better understand the fate of downgoing plates at their terminus.

Several experiments can be developed to further test the hypotheses presented in this Ph.D. dissertation. First, continued monitoring by OBS networks may discover additional faults in the region. Second, ocean-bottom GPS measurements could provide the best constraints on the relative motion of the ExP with respect to neighboring plates, and could reveal regional variances, such as localized block rotations and differences in subduction rates along the Cascadia margin. Further seismic reflection profiles could illuminate the surface of the subducting slab landward of the subduction front to a higher degree of precision than my current estimations, providing a more accurate model of the southern ExP geometric variance. With the current SeaJade I and II datasets, a machine learning approach could be utilized to identify and locate additional earthquakes, increasing the completeness of the earthquake catalogues. Regardless of experiment or method, northern Cascadia would benefit from further investigation to mitigate future tsunami and earthquake hazards.

References

Aki, K., and Richards, P. G. (1980). *Quantitative seismology* (Vol. II). Retrieved from https://ui.adsabs.harvard.edu/abs/2002quse.book.....A/abstract

Alvarez-Gomez, J. A. (2009). *Tectónica Activa y Geodinámica en el Norte de Centroamérica*. *Thesis*. PhD, Complutense University of Madrid, Spain. Retrieved from https://eprints.ucm.es/30783/

Álvarez-Gómez, J. A. (2019). FMC—Earthquake focal mechanisms data management, cluster and classification. *SoftwareX*, *9*, 299–307. https://doi.org/10.1016/j.softx.2019.03.008

Amorèse, D. (2007). Applying a change-point detection method on frequency-magnitude distributions. *Bulletin of the Seismological Society of America*, *97*(5), 1742–1749. https://doi.org/10.1785/0120060181

Atwater, B. F. (2005). *The orphan tsunami of 1700: Japanese clues to a parent earthquake in North America*. US Geological Survey. https://doi.org/https://doi.org/10.3133/pp1707

Atwater, B. F., Nelson, A. R., Clague, J. J., Carver, G. A., Yamaguchi, D. K., Bobrowsky, P. T., Bourgeois, J., Darienzo, M. E., Grant, W. C., Hemphill-Haley, E., et al. (1995). Summary of coastal geologic evidence for past great earthquakes at the Cascadia subduction zone. *Earthquake Spectra*, *11*(1), 1–18. https://doi.org/https://doi.org/10.1193/1.1585800

Atwater, T. (1970). Implications of plate tectonics for the cenozoic tectonic evolution of western north america. *Bulletin of the Geological Society of America*, *81*(12), 3513–3536. https://doi.org/10.1130/0016-7606(1970)81[3513:IOPTFT]2.0.CO;2

Audet, P., Bostock, M. G., Mercier, J. P., and Cassidy, J. F. (2008). Morphology of the explorer - Juan de Fuca slab edge in northern Cascadia: Imaging plate capture at a ridge-trench-transform riple junction. *Geology*, *36*(11), 895–898. https://doi.org/10.1130/G25356A.1

Audet, P., Bostock, M. G., Boyarko, D. C., Brudzinski, M. R., and Allen, R. M. (2010). Slab

morphology in the Cascadia fore arc and its relation to episodic tremor and slip. *Journal of Geophysical Research: Solid Earth*, *115*(4), B00A16. https://doi.org/10.1029/2008JB006053

Van Avendonk, H. J. A., Holbrook, W. S., Lizarralde, D., and Denyer, P. (2011). Structure and serpentinization of the subducting Cocos plate offshore Nicaragua and Costa Rica. *Geochemistry, Geophysics, Geosystems*, *12*(6), 1–23. https://doi.org/10.1029/2011GC003592

Bayrak, Y., Yilmaztürk, A., and Öztürk, S. (2002). Lateral variations of the modal (a/b) values for the different regions of the world. *Journal of Geodynamics*, *34*(5), 653–666. https://doi.org/10.1016/S0264-3707(02)00037-6

Bezacier, L., Reynard, B., Bass, J. D., Sanchez-Valle, C., and Van de Moortèle, B. (2010). Elasticity of antigorite, seismic detection of serpentinites, and anisotropy in subduction zones. *Earth and Planetary Science Letters*, *289*(1–2), 198–208. https://doi.org/10.1016/j.epsl.2009.11.009

Braunmiller, J., and Nábělek, J. (2002). Seismotectonics of the Explorer region. *Journal of Geophysical Research: Solid Earth*, *107*(B10), 1-1—1-25. https://doi.org/10.1029/2001jb000220

Brocher, T. M. (2005). Empirical relations between elastic wavespeeds and density in the Earth's crust. *Bulletin of the Seismological Society of America*, *95*(6), 2081–2092. https://doi.org/10.1785/0120050077

Brothers, D. S., Miller, N. C., Barrie, J. V., Haeussler, P. J., Greene, H. G., Andrews, B. D., Zielke, O., Watt, J., and Dartnell, P. (2020). Plate boundary localization, slip-rates and rupture segmentation of the Queen Charlotte Fault based on submarine tectonic geomorphology. *Earth and Planetary Science Letters*, *530*. https://doi.org/10.1016/j.epsl.2019.115882

Buland, R., and Chapman, C. H. (1983). The computation of seismic travel times. *Bull. Seismol. Soc. Am.*, *73*(5), 1271–1302. Retrieved from https://pubs.geoscienceworld.org/ssa/bssa/article-abstract/73/5/1271/118430

Cannat, M. (1993). Emplacement of mantle rocks in the seafloor at mid-ocean ridges. *Journal of Geophysical Research: Solid Earth*, *98*(B3), 4163–4172. https://doi.org/10.1029/92JB02221

Cao, A., and Gao, S. S. (2002). Temporal variation of seismic b -values beneath northeastern Japan island arc. *Geophysical Research Letters*, *29*(9), 48-1—48-3. https://doi.org/10.1029/2001gl013775

Christensen, N. I. (2004). Serpentinites, Peridotites, and Seismology. *International Geology Review*, *46*(9), 795–816. https://doi.org/10.2747/0020-6814.46.9.795

Christensen, N. I., and Salisbury, M. H. (1975). Structure and constitution of the lower oceanic crust. *Reviews of Geophysics*, *13*(1), 57–86. https://doi.org/10.1029/RG013i001p00057

Clowes, R. M., and Malecek, S. J. (1976). Preliminary interpretation of a marine deep seismic sounding survey in the region of Explorer ridge. *Canadian Journal of Earth Sciences*, *13*(11), 1545–1555. https://doi.org/https://doi.org/10.1139/e76-160

Clowes, R. M., Thorleifson, A. J., and Lynch, S. (1981). Winona Basin, west coast Canada: crustal structure from marine seismic studies. *Journal of Geophysical Research*, *86*(B1), 225–242. https://doi.org/10.1029/JB086iB01p00225

Clowes, R. M., Baird, D. J., and Dehler, S. A. (1997). Crustal structure of the Cascadia subduction zone, southwestern British Columbia, from potential field and seismic studies. *Canadian Journal of Earth Sciences*, *34*(3), 317–335. https://doi.org/10.1139/e17-028

Crotwell, H. P., Owens, T. J., and Ritsema, J. (1999). The TauP Toolkit: Flexible Seismic Travel-time and Ray-path Utilities. *Seismological Research Letters*, *70*(2), 154–160. https://doi.org/10.1785/gssrl.70.2.154

Davis, E. E., and Riddihough, R. P. (1982). The Winona Basin: structure and tectonics. *Canadian Journal of Earth Sciences*, *19*(4), 767–788. https://doi.org/10.1139/e82-065

DeMets, C., and Merkouriev, S. (2016). High-resolution reconstructions of Pacific-North America

plate motion: 20 Ma to present. *Geophysical Journal International*, *207*(2), 741–773. https://doi.org/10.1093/gji/ggw305

DeMets, C., Gordon, R. G., Argus, D. F., and Stein, S. (1994). Effect of recent revisions to the geomagnetic reversal time scale on estimates of current plate motions. *Geophysical Research Letters*, *21*(20), 2191–2194. https://doi.org/10.1029/94GL02118

DeMets, C., Gordon, R. G., and Argus, D. F. (2010). Geologically current plate motions. *Geophysical Journal International*, *181*(1), 1–80. https://doi.org/10.1111/j.1365-246X.2009.04491.x

Detrick, R., Collins, J., Stephen, R., and Swift, S. (1994). In situ evidence for the nature of the seismic layer 2/3 boundary in oceanic crust. *Nature*, *370*(6487), 288–290. https://doi.org/10.1038/370288a0

Dougherty, S. L., Clayton, R. W., and Helmberger, D. V. (2012). Seismic structure in central Mexico: Implications for fragmentation of the subducted Cocos plate. *Journal of Geophysical Research: Solid Earth*, *117*(9), 1–17. https://doi.org/10.1029/2012JB009528

Dragert, H., and Hyndman, R. D. (1995). Continuous GPS monitoring of elastic strain in the Northern Cascadia Subduction Zone. *Geophysical Research Letters*, *22*(7), 755–758. https://doi.org/10.1029/95GL00469

Earthquakes Canada, G. (2017). Earthquake Search (On-line Bulletin). Retrieved June 1, 2017, from http://earthquakescanada.nrcan.gc.ca/stndon/NEDB-BNDS/bulletin-en.php

Eberhart-Phillips, D. (1990). Three-dimensional P and S velocity structure in the Coalinga Region, California. *Journal of Geophysical Research*, *95*(B10), 15343–15363. https://doi.org/10.1029/jb095ib10p15343

Evans, B. W. (2004). The Serpentinite Multisystem Revisited: Chrysotile Is Metastable. *International Geology Review*, *46*(6), 479–506. https://doi.org/10.2747/0020-6814.46.6.479

Ewell, R. H., Bunting, E. N., and Geller, R. F. (1935). Thermal decomposition of talc. *Journal of Research of the National Bureau of Standards*, *15*, 551–556.

Fujie, G., Kodaira, S., Yamashita, M., Sato, T., Takahashi, T., and Takahashi, N. (2013). Systematic changes in the incoming plate structure at the Kuril trench. *Geophysical Research Letters*, *40*(1), 88–93. https://doi.org/10.1029/2012GL054340

Gao, D. (2016). *Defining megathrust tsunami sources at northernmost Cascadia using thermal and structural information*. MSc Thesis, University of Victoria, Canada. Retrieved from http://dspace.library.uvic.ca/handle/1828/7435

Gao, D., Wang, K., Davis, E. E., Jiang, Y., Insua, T. L., and He, J. (2017). Thermal state of the Explorer segment of the Cascadia subduction zone: Implications for seismic and tsunami hazards. *Geochemistry, Geophysics, Geosystems*, *18*(4), 1569–1579. https://doi.org/10.1002/2017GC006838

Goebel, T. H. W., Kwiatek, G., Becker, T. W., Brodsky, E. E., and Dresen, G. (2017). What allows seismic events to grow big?: Insights from b-value and fault roughness analysis in laboratory stick-slip experiments. *Geology*, *45*(9), 815–818. https://doi.org/10.1130/G39147.1

Goldfinger, C., Grijalva, K., Bürgmann, R., Morey, A. E., Johnson, J. E., Nelson, C. H., Gutiérrez-Pastor, J., Ericsson, A., Karabanov, E., Chaytor, J. D., et al. (2008). Late Holocene rupture of the northern San Andreas fault and possible stress linkage to the Cascadia Subduction Zone. *Bulletin of the Seismological Society of America*, *98*(2), 861–889. https://doi.org/10.1785/0120060411

Goldfinger, C., Nelson, C. H., Morey, A. E., Johnson, J. E., Patton, J. R., Karabanov, E. B., Gutierrez-Pastor, J., Eriksson, A. T., Gracia, E., Dunhill, G., et al. (2012). Turbidite event history--Methods and implications for Holocene paleoseismicity of the Cascadia subduction zone. *U.S. Geological Survey*, 170. https://doi.org/10.3133/PP1661F

Grevemeyer, I., Ranero, C. R., Flueh, E. R., Kläschen, D., and Bialas, J. (2007). Passive and active

seismological study of bending-related faulting and mantle serpentinization at the Middle America trench. *Earth and Planetary Science Letters*, *258*(3–4), 528–542. https://doi.org/10.1016/j.epsl.2007.04.013

Han, S., Carbotte, S. M., Canales, J. P., Nedimović, M. R., Carton, H., Gibson, J. C., and Horning, G. W. (2016). Seismic reflection imaging of the Juan de Fuca plate from ridge to trench: New constraints on the distribution of faulting and evolution of the crust prior to subduction. *Journal of Geophysical Research: Solid Earth*, *121*(3), 1849–1872. https://doi.org/10.1002/2015JB012416

Hardebeck, J. L., and Shearer, P. M. (2002). A new method for determining first-motion focal mechanisms. *Bulletin of the Seismological Society of America*, *92*(6), 2264–2276. https://doi.org/10.1785/0120010200

Hardebeck, J. L., and Shearer, P. M. (2003). Using S/P amplitude ratios to constrain the focal mechanisms of small earthquakes. *Bulletin of the Seismological Society of America*, *93*(6), 2434–2444. https://doi.org/10.1785/0120020236

Hilairet, N., Reynard, B., Wang, Y., Daniel, I., Merkel, S., Nishiyama, N., and Petitgirard, S. (2007). High-pressure creep of serpentine, interseismic deformation, and initiation of subduction. *Science*, *318*(5858), 1910–1913. https://doi.org/10.1126/science.1148494

Hole, J. A., and Zelt, B. C. (1995). 3-D finite-difference reflection travel times. *Geophysical Journal International*, *121*(2), 427–434. https://doi.org/10.1111/j.1365-246X.1995.tb05723.x

Hutchinson, J., Kao, H., Spence, G., Obana, K., Wang, K., and Kodaira, S. (2019). Seismic characteristics of the nootka fault zone: Results from the seafloor earthquake array Japan–Canada cascadia experiment (seajade). *Bulletin of the Seismological Society of America*, *109*(6), 2252–2276. https://doi.org/10.1785/0120190008

Hyndman, R. D., and Wang, K. (1995). The rupture zone of Cascadia great earthquakes from current deformation and the thermal regime. *Journal of Geophysical Research: Solid Earth*,

100(B11), 22133–22154. https://doi.org/https://doi.org/10.1029/95JB01970

Hyndman, R. D., and Weichert, D. H. (1983). Seismicity and rates of relative motion on the plate boundaries of western North America. *Geophysical Journal International*, *72*(1), 59–82. https://doi.org/10.1111/j.1365-246X.1983.tb02804.x

Hyndman, R. D., Riddihough, R. P., and Herzer, R. (1979). The Nootka Fault Zone -- a new plate boundary off western Canada. *Geophysical Journal International*, *58*(3), 667–683. https://doi.org/10.1111/j.1365-246X.1979.tb04801.x

Kao, H., Wang, K., Chen, R. Y., Wada, I., He, J., and Malone, S. D. (2008). Identifying the rupture plane of the 2001 Nisqually Washington, earthquake. *Bulletin of the Seismological Society of America*, *98*(3), 1546–1558. https://doi.org/10.1785/0120070160

Kao, H., Shan, S. J., Dragert, H., and Rogers, G. (2009). Northern Cascadia episodic tremor and slip: A decade of tremor observations from 1997 to 2007. *Journal of Geophysical Research: Solid Earth*, *114*(11), B00A12 1-20. https://doi.org/10.1029/2008JB006046

Kao, H., Shan, S. J., Bent, A., Woodgold, C., Rogers, G., Cassidy, J. F., and Ristau, J. (2012). Regional centroid-moment-tensor analysis for earthquakes in Canada and adjacent regions: An update. *Seismological Research Letters*, *83*(3), 505–515. https://doi.org/10.1785/gssrl.83.3.505

Kao, H., Behr, Y., Currie, C. A., Hyndman, R., Townend, J., Lin, F. C., Ritzwoller, M. H., Shan, S. J., and He, J. (2013). Ambient seismic noise tomography of Canada and adjacent regions: Part I. Crustal structures. *Journal of Geophysical Research: Solid Earth*, *118*(11), 5865–5887. https://doi.org/10.1002/2013JB010535

Karato, S., and Wu, P. (1993). Rheology of the Upper Mantle: A Synthesis. *Science*, *260*(5109), 771–778. https://doi.org/10.1126/science.260.5109.771

Kim, Y., Clayton, R. W., Asimow, P. D., and Jackson, J. M. (2013). Generation of talc in the mantle wedge and its role in subduction dynamics in central Mexico. *Earth and Planetary*

Science Letters, *384*, 81–87. https://doi.org/10.1016/J.EPSL.2013.10.006

Krischer, L., Megies, T., Barsch, R., Beyreuther, M., Lecocq, T., Caudron, C., and Wassermann, J. (2015). ObsPy: a bridge for seismology into the scientific Python ecosystem. *Computational Science & Discovery*, *8*(1), 014003. https://doi.org/10.1088/1749-4699/8/1/014003

Leonard, L. J., Currie, C. A., Mazzotti, S., and Hyndman, R. D. (2010). Rupture area and displacement of past Cascadia great earthquakes from coastal coseismic subsidence. *Geological Society of America Bulletin*, *122*(11–12), 2079–2096. https://doi.org/10.1130/B30108.1

Long, M. D. (2016). The Cascadia Paradox: Mantle flow and slab fragmentation in the Cascadia subduction system. *Journal of Geodynamics*, *102*, 151–170. https://doi.org/10.1016/j.jog.2016.09.006

Lu, Z., and Wyss, M. (1996). Segmentation of the Aleutian plate boundary derived from stress direction estimates based on fault plane solutions. *Journal of Geophysical Research: Solid Earth*, *101*(B1), 803–816. https://doi.org/10.1029/95JB03036

Mainprice, D., Le Page, Y., Rodgers, J., and Jouanna, P. (2008). Ab initio elastic properties of talc from 0 to 12 GPa: Interpretation of seismic velocities at mantle pressures and prediction of auxetic behaviour at low pressure. *Earth and Planetary Science Letters*, *274*(3–4), 327–338. https://doi.org/10.1016/J.EPSL.2008.07.047

Malecek, S. J., and Clowes, R. M. (1978). Crustal structure near Explorer Ridge from a marine deep seismic sounding survey. *Journal of Geophysical Research: Solid Earth*, *83*(B12), 5899–5912. https://doi.org/10.1029/JB083iB12p05899

Mazzotti, S., Dragert, H., Henton, J., Schmidt, M., Hyndman, R., James, T., Lu, Y., and Craymer, M. (2003). Current tectonics of northern Cascadia from a decade of GPS measurements. *Journal of Geophysical Research: Solid Earth*, *108*(B12), 1-1—1-18. https://doi.org/https://doi.org/10.1029/2003JB002653

McCaffrey, R., Qamar, A. I., King, R. W., Wells, R., Khazaradze, G., Williams, C. A., Stevens, C. W., Vollick, J. J., and Zwick, P. C. (2007a). Fault locking, block rotation and crustal deformation in the Pacific Northwest. *Geophysical Journal International*, *169*(3), 1315–1340. https://doi.org/10.1111/j.1365-246X.2007.03371.x

McCaffrey, R., Qamar, A. I., King, R. W., Wells, R., Khazaradze, G., Williams, C. A., Stevens, C. W., Vollick, J. J., and Zwick, P. C. (2007b). Fault locking, block rotation and crustal deformation in the Pacific Northwest. *Geophysical Journal International*, *169*(3), 1315–1340. https://doi.org/10.1111/j.1365-246X.2007.03371.x

McCrory, P. A., Blair, J. L., Waldhauser, F., and Oppenheimer, D. H. (2012). Juan de Fuca slab geometry and its relation to Wadati-Benioff zone seismicity. *Journal of Geophysical Research: Solid Earth*, *117*(9), B09306 1-23. https://doi.org/10.1029/2012JB009407

Megies, T., Beyreuther, M., Barsch, R., Krischer, L., and Wassermann, J. (2011). ObsPy - what can it do for data centers and observatories? *Annals of Geophysics*, *54*(1), 47–58. https://doi.org/10.4401/ag-4838

Mével, C. (2003). Serpentinization of abyssal peridotites at mid-ocean ridges. *Comptes Rendus Geoscience*, *335*(10–11), 825–852. https://doi.org/10.1016/J.CRTE.2003.08.006

Mignan, A., and Woessner, J. (2012). Estimating the magnitude of completeness in earthquake catalogs. *Community Online Resource for Statistical Seismicity Analysis*, 1–32. https://doi.org/10.5078/corssa-00180805.

Mosher, S. G., Audet, P., and L'Heureux, I. (2014). Seismic evidence for rotating mantle flow around subducting slab edge associated with oceanic microplate capture. *Geophysical Research Letters*, *41*(13), 4548–4553. https://doi.org/10.1002/2014GL060630

Mullen, E. K., and Weis, D. (2015). Evidence for trench-parallel mantle flow in the northern Cascade Arc from basalt geochemistry. *Earth and Planetary Science Letters*, *414*, 100–107. https://doi.org/10.1016/j.epsl.2015.01.010

Obana, K., Scherwath, M., Yamamoto, Y., Kodaira, S., Wang, K., Spence, G., Riedel, M., and Kao, H. (2015). Earthquake Activity in Northern Cascadia Subduction Zone Off Vancouver Island Revealed by Ocean-Bottom Seismograph Observations. *Bulletin of the Seismological Society of America*, *105*(1), 489–495. https://doi.org/https://doi.org/10.1785/0120140095

Omori, F. (1894). On the aftershocks of earthquakes. *Journal of the College of Science, Imperial University*, *7*, 111–200.

Park, J. O., Moore, G. F., Tsuru, T., Kodaira, S., and Kaneda, Y. (2004). A subducted oceanic ridge influencing the Nankai megathrust earthquake rupture. *Earth and Planetary Science Letters*, *217*(1–2), 77–84. https://doi.org/10.1016/S0012-821X(03)00553-3

Pavlis, G. L., Vernon, F., Harvey, D., and Quinlan, D. (2004). The generalized earthquake-location (GENLOC) package: an earthquake-location library. *Computers & Geosciences*, *30*(9–10), 1079–1091. https://doi.org/10.1016/j.cageo.2004.06.010

Pawley, A. R., and Wood, B. J. (1995). The high-pressure stability of talc and 10 Aa phase; potential storage sites for H_2O in subduction zones. *American Mineralogist*, *80*(9–10), 998–1003. https://doi.org/10.2138/am-1995-9-1015

Peacock, S. M., and Hyndman, R. D. (1999). Hydrous minerals in the mantle wedge and the maximum depth of subduction thrust earthquakes. *Geophysical Research Letters*, *26*(16), 2517–2520. https://doi.org/10.1029/1999GL900558

Ranero, C. R., Phipps Morgan, J., McIntosh, K., and Reichert, C. (2003). Bending-related faulting and mantle serpentinization at the Middle America trench. *Nature*, *425*(6956), 367–373. https://doi.org/10.1038/nature01961

Reasenberg, P., and Oppenheimer, D. H. (1985). FPFIT, FPPLOT and FPPAGE: Fortran computer programs for calculating and displaying earthquake fault-plane solutions. *U.S. Geological Survey Open-File Report*, (85), No. 85-739. https://doi.org/10.3133/OFR85739

Riddihough, R. P. (1977). A model for recent plate interactions off Canada's west coast.

Canadian Journal of Earth Sciences, *14*(3), 384–396. https://doi.org/10.1139/e77-039

Riddihough, R. P. (1984). Recent Movements of the Juan de Fuca Plate System. *Journal of Geophysical Research*, *89*(B8), 6980–6994. https://doi.org/10.1029/JB089iB08p06980

Riddihough, R. P., Currie, R. G., and Hyndman, R. D. (1980). The Dellwood Knolls and their role in triple junction tectonics off northern Vancouver Island. *Canadian Journal of Earth Sciences*, *17*(5), 577–593. https://doi.org/10.1139/e80-057

Riedel, M., Conway, K. W., Côté, M. M., Middleton, G., Neelands, P. J., Obana, K., Saijo, T., Stacey, C. D., Takahashi, T., Terada, I., et al. (2014). Report of Cruise 2014006PGC, SeaJade-II: Seafloor Earthquake Array Japan-Canada Cascadia Experiment OBS Recovery. *Geological Survey of Canada*, *7715*, 1–26. https://doi.org/10.4095/295548

Rohr, K. M. M., Furlong, K. P., and Riedel, M. (2018). Initiation of Strike-Slip Faults, Serpentinization, and Methane: The Nootka Fault Zone, the Juan de Fuca-Explorer Plate Boundary. *Geochemistry, Geophysics, Geosystems*, *19*(11), 4290–4312. https://doi.org/10.1029/2018GC007851

Ross, Z. E., and Ben-Zion, Y. (2014). Automatic picking of direct P, S seismic phases and fault zone head waves. *Geophysical Journal International*, *199*(1), 368–381. https://doi.org/10.1093/gji/ggu267

Ryan, W. B. F., Carbotte, S. M., Coplan, J. O., O'Hara, S., Melkonian, A., Arko, R., Weissel, R. A., Ferrini, V., Goodwillie, A., Nitsche, F., et al. (2009). Global multi-resolution topography synthesis. *Geochemistry, Geophysics, Geosystems*, *10*(3), 1–9. https://doi.org/10.1029/2008GC002332

Saroglou, C., and Kallimogiannis, V. (2017). Fracturing process and effect of fracturing degree on wave velocity of a crystalline rock. *Journal of Rock Mechanics and Geotechnical Engineering*, *9*(5), 797–806. https://doi.org/10.1016/j.jrmge.2017.03.012

Satake, K. (2003). Fault slip and seismic moment of the 1700 Cascadia earthquake inferred from

Japanese tsunami descriptions. *Journal of Geophysical Research*, *108*(B11), 2535. https://doi.org/10.1029/2003JB002521

Sato, H., and Ito, K. (2002). Olivine-Pyroxene-H $_2$ O system as a practical analogue for estimating the elastic properties of fluid-bearing mantle rocks at high pressures and temperatures. *Geophysical Research Letters*, *29*(9), 39-1-39–4. https://doi.org/10.1029/2001GL014212

Scherwath, M., Spence, G., Obana, K., Kodaira, S., Wang, K., Riedel, M., McGuire, J., and Collins, J. (2011). Seafloor seismometers monitor northern Cascadia earthquakes. *Eos, Transactions American Geophysical Union*, *92*(47), 421–422. https://doi.org/https://doi.org/10.1029/2011EO470001

Shimamoto, T., and Noda, H. (2014). A friction to flow constitutive law and its application to a 2-D modeling of earthquakes. *Journal of Geophysical Research: Solid Earth*, *119*(11), 8089–8106. https://doi.org/10.1002/2014JB011170

Spence, G. D., Clowes, R. M., and Ellis, R. M. (1985). Seismic structure across the active subduction zone of western Canada. *Journal of Geophysical Research: Solid Earth (1978–2012)*, *90*(B8), 6754–6772. https://doi.org/10.1029/JB090iB08p06754

Stubailo, I. (2015). *Seismic anisotropy below Mexico and its implications for mantle dynamics*. *ProQuest Dissertation and Theses Database*. PhD Thesis, UCLA. Retrieved from https://escholarship.org/uc/item/3b74j4dh

Thurber, C., and Eberhart-Phillips, D. (1999). Local earthquake tomography with flexible gridding. *Computers & Geosciences*, *25*(7), 809–818. https://doi.org/https://doi.org/10.1016/S0098-3004(99)00007-2

Tilmann, F. J., Grevemeyer, I., Flueh, E. R., Dahm, T., and Goßler, J. (2008). Seismicity in the outer rise offshore southern Chile: Indication of fluid effects in crust and mantle. *Earth and Planetary Science Letters*, *269*(1–2), 41–55. https://doi.org/10.1016/j.epsl.2008.01.044

Toomey, D. R., Allen, R. M., Barclay, A. H., Bell, S. W., Bromirski, P. D., Carlson, R. L., Chen, X.,

Collins, J. A., Dziak, R. P., Evers, B., et al. (2014). The Cascadia initiative: A sea change in seismological studies of subduction zones. *Oceanography*, *27*(2), 138–150. https://doi.org/10.5670/oceanog.2014.49

Tréhu, A. M., Braunmiller, J., and Davis, E. (2015). Seismicity of the Central Cascadia Continental Margin near 44.5° N: A Decadal View. *Seismological Research Letters*, *86*(3), 819–829. https://doi.org/https://doi.org/10.1785/0220140207

Utsu, T. (1961). A statistical study of the occurrence of aftershocks. *Geophysical Magazine*, *30*, 521–605.

Wagner, L. S., Beck, S., and Zandt, G. (2005). Upper mantle structure in the south central Chilean subduction zone (30° to 36°S). *Journal of Geophysical Research: Solid Earth*, *110*(1), 1–20. https://doi.org/10.1029/2004JB003238

Waldhauser, F. (2001). HypoDD–A program to compute double-difference hypocenter locations. *US Geol. Surv. Open File Rep., 01*, *113*, 1–25. https://doi.org/10.7916/D8SN072H

Waldhauser, F., and Ellsworth, W. L. (2000). A double-difference earthquake location algorithm: method and application to the northern Hayward fault, California. *Bulletin of the Seismological Society of America*, *90*(6), 1353–1368. https://doi.org/https://doi.org/10.1785/0120000006

Wang, K., and Bilek, S. L. (2011). Do subducting seamounts generate or stop large earthquakes? *Geology*, *39*(9), 819–822. https://doi.org/10.1130/G31856.1

Wang, K., and Davis, E. E. (1992). Thermal effects of marine sedimentation in hydrothermally active areas. *Geophysical Journal International*, *110*(1), 70–78. https://doi.org/10.1111/j.1365-246X.1992.tb00714.x

Wang, K., and Tréhu, A. M. (2016). Invited review paper: Some outstanding issues in the study of great megathrust earthquakes—The Cascadia example. *Journal of Geodynamics*, *98*, 1–18. https://doi.org/10.1016/j.jog.2016.03.010

Wang, K., Wells, R., Mazzotti, S., Hyndman, R. D., and Sagiya, T. (2003). A revised dislocation model of interseismic deformation of the Cascadia subduction zone. *Journal of Geophysical Research: Solid Earth*, *108*(B1). https://doi.org/10.1029/2001JB001227

Wassermann, J., Barsch, R., Beyreuther, M., Behr, Y., Megies, T., and Krischer, L. (2010). ObsPy: A Python Toolbox for Seismology. *Seismological Research Letters*, *81*(3), 530–533. https://doi.org/10.1785/gssrl.81.3.530

Wells, R. E., and Simpson, R. W. (2001). Northward migration of the Cascadia forearc in the northwestern U.S. and implications for subduction deformation. *Earth, Planets and Space*, *53*(4), 275–283. https://doi.org/10.1186/BF03352384

Wessel, P., and Smith, W. H. F. (1998). New, improved version of generic mapping tools released. *Eos, Transactions American Geophysical Union*, *79*(47), 579–579. https://doi.org/10.1029/98EO00426

White, R. S., McKenzie, D., and O'Nions, R. K. (1992). Oceanic crustal thickness from seismic measurements and rare earth element inversions. *Journal of Geophysical Research: Solid Earth*, *97*(B13), 19683–19715. https://doi.org/10.1029/92JB01749

Wiemer, S., and Wyss, M. (2000). Minimum Magnitude of Completeness in Earthquake Catalogs: Examples from Alaska, the Western United States, and Japan. *Bulletin of the Seismological Society of America*, *90*(4), 859–869. https://doi.org/10.1785/0119990114

Williams, M. C., Tréhu, A. M., and Braunmiller, J. (2011). Seismicity at the Cascadia plate boundary beneath the Oregon continental shelf. *Bulletin of the Seismological Society of America*, *101*(3), 940–950. https://doi.org/https://doi.org/10.1785/0120100198

Willoughby, E. C., and Hyndman, R. D. (2005). Earthquake rate, slip rate, and the effective seismic thickness for oceanic transform faults of the Juan de Fuca plate system. *Geophysical Journal International*, *160*(3), 855–868. https://doi.org/https://doi.org/10.1111/j.1365-246X.2005.02523.x

Wilson, D. S. (1993). Confidence intervals for motion and deformation of the Juan de Fuca Plate. *Journal of Geophysical Research*, *98*(B9), 16053–16071. https://doi.org/10.1029/93JB01227

Woessner, J., and Wiemer, S. (2005). Assessing the quality of earthquake catalogues: Estimating the magnitude of completeness and its uncertainty. *Bulletin of the Seismological Society of America*, *95*(2), 684–698. https://doi.org/10.1785/0120040007

Wyss, M., Hasegawa, A., Wiemer, S., and Umino, N. (1999). Quantitative mapping of precursory seismic quiescence before the 1989, M 7.1 off-Sanriku earthquake, Japan. *Annali Di Geofisica*, *42*(5), 851–869. https://doi.org/https://doi.org/10.4401/ag-3765

Wyss, M., Sammis, C. G., Nadeau, R. M., and Wiemer, S. (2004). Fractal Dimension and b-Value on Creeping and Locked Patches of the San Andreas Fault near Parkfield, California. *Bulletin of the Seismological Society of America*, *94*(2), 410–421. https://doi.org/10.1785/0120030054

Yang, H., Liu, Y., and Lin, J. (2013). Geometrical effects of a subducted seamount on stopping megathrust ruptures. *Geophysical Research Letters*, *40*(10), 2011–2016. https://doi.org/10.1002/grl.50509

Zhang, H. (2003). Double-Difference Tomography: The Method and Its Application to the Hayward Fault, California. *Bulletin of the Seismological Society of America*, *93*(5), 1875–1889. https://doi.org/10.1785/0120020190

Zhang, H., and Thurber, C. (2006). Development and applications of double-difference seismic tomography. *Pure and Applied Geophysics*, *163*(2–3), 373–403. https://doi.org/10.1007/s00024-005-0021-y

Zheng, Y., and Lay, T. (2006). Low Vp/Vsratios in the crust and upper mantle beneath the Sea of Okhotsk inferred from teleseismic pMP, sMP, and sMS underside reflections from the Moho. *Journal of Geophysical Research: Solid Earth*. https://doi.org/10.1029/2005JB003724

Appendix A Earthquake Datasets

Data used in the below tables are available from the Open Science Forum at (https://osf.io/w4d3y/?view_only=bded7b7583484cc0a3282f4cce02b79f). Descriptions of the tables are as follows:

Appendix Table A.1. Arrival information for the relocated hypocenters for SeaJade I. The arrivals are included in the file 'Appendix_Table_A1.txt'. Hypocenter origin IDs are first provided in the following format:

> #, origin ID, station, travel-time(s), weight(1, by default), phase
>
> (repeat for each additional phase)

Appendix Table A.2. Hypocenter information for the relocated events for SeaJade I.The locations are included in the file 'Appendix_Table_A2.xlsx'. The columns are organized as follows:

> Origin ID, latitude, longitude, depth, X(m), Y(m), Z(m), EX(m), EY(m), EZ(m), year, month, day, hour, minute, second, magnitude, NCCP, NCCS, NCTP, NCTS, RCC(s), RCT(s), CID.

The X, Y, and Z parameters are measured in meters from the cluster centroid. EX, EY, and EZ are the estimated LSQR errors in E-W, N-S, and depth, respectively. NCCP, NCCS, NCTP, and NCTS, are the numbers of P and S phase used in the cross-correlation and travel-time difference datasets to locate the earthquakes, respectively. RCC and RCT are the time residuals, in seconds, for the cross-correlation and travel-time difference datasets, respectively.

Appendix Table A.3. Arrival information for the relocated hypocenters for SeaJade II. The arrivals are included in the file 'Appendix_Table_A3.txt'. Hypocenter origin IDs are first provided in the following format:

> #, origin ID, station, travel-time(s), weight(1, by default), phase
>
> (repeat for each additional phase)

Appendix Table A.4. Hypocenter information for the relocated events for SeaJade II.The locations are included in the file 'Appendix_Table_A4.xlsx'. The columns are organized as follows:

> Origin ID, latitude, longitude, depth, X(m), Y(m), Z(m), EX(m), EY(m), EZ(m), year, month, day, hour, minute, second, magnitude, NCCP, NCCS, NCTP, NCTS, RCC(s), RCT(s), CID.

The X, Y, and Z parameters are measured in meters from the cluster centroid. EX, EY, and EZ are the estimated LSQR errors in E-W, N-S, and depth, respectively. NCCP, NCCS, NCTP, and NCTS, are the numbers of P and S phase used in the cross-correlation and travel-time difference datasets to locate the earthquakes, respectively. RCC and RCT are the time residuals, in seconds, for the cross-correlation and travel-time difference datasets, respectively.

Appendix B Focal Mechanism Datasets

Focal mechanism solutions were computed with the program HASH (Hardebeck and Shearer, 2002, 2003). Like many programs used to calculate focal mechanism solutions (e.g. FPFIT; Reasenberg and Oppenheimer, 1985), HASH calculates the best-fit solutions for earthquakes from input *P*-arrival first motions. An additional benefit of HASH is that *S/P* amplitude ratios can be utilized to further constrain focal mechanism solutions. Theoretically, *P* amplitudes along nodal planes would be smallest, while they would be at their largest in the centre of the focal sphere quadrants. Therefore, *S/P* ratios are expected to be much larger along nodal planes than within focal sphere quadrants.

Several factors are utilized for determining the quality of a best-fit focal mechanism solution, which is ranked from A-F, with A being the best rank. Any focal mechanisms with fewer than 8 first motion polarities are given an F rank. Solutions with azimuthal gaps > 90° and takeoff angle gaps > 60° are given an E rank. Any solution with smaller gaps is considered at least a D-ranked solution. Higher ranks are given provided smaller average misfits and RMS fault plane uncertainties, and larger station distribution ratios and focal mechanism probabilities. For a given earthquake, these values are determined from a set of focal mechanisms calculated over repeated trials. Ultimately, an A-ranked focal mechanism solution has an average misfit ≤ 0.15, an RMS fault plane uncertainty ≤ 25°, a station distribution ratio ≥ 0.5, a mechanism probability ≥ 0.8, a maximum azimuthal gap ≤ 90°, a maximum takeoff angle gap ≤ 60°, and 8 or more first-motion polarities.

The focal mechanism data described for the below tables are available from the Open Science Forum at (https://osf.io/w4d3y/?view_only=bded7b7583484cc0a3282f4cce02b79f). Descriptions of the tables are as follows:

Appendix Table B.1. Focal mechanism information for events from SeaJade I.The focal mechanisms are included in the file 'Appendix_Table_B1.xlsx'. The columns are organized as follows:

> ID, Date, Latitude, Longitude, Depth, Magnitude, Strike, Dip, Rake, FP_unc, Aux_unc, num_P_pol, Wght % Misfit, Rank, Probability, num_SP, and Mode.

The depth parameter is measured in km. The magnitude parameter is measured in local magnitude (M_L). The parameters FP_unc and Aux_unc are the uncertainties for the primary and auxiliary fault planes, given in degrees.

The parameter num_P_pol is the number of *P* first motion polarities used in calculating the focal mechanism. Wght % Misfit is the weighted percent misfit of first motions. Rank can range from A-F (although only A-ranked data are provided), and is a measure of focal mechanism quality. Probability is a measure of how close the mechanism is to the true solution. num_SP is the number of *S/P* ratios used in calculating the focal mechanism. Mode is the failure mode of the focal mechanism: N – normal, R – reverse, S – strike-slip.

Appendix Table B.2. Focal mechanism information for events from SeaJade II.The focal mechanisms are included in the file 'Appendix_Table_B2.xlsx'. Focal mechanisms from the Nootka Sequence have bolded italicized IDs. The columns are organized as follows:

> ID, Date, Latitude, Longitude, Depth, Magnitude, Strike, Dip, Rake, FP_unc, Aux_unc, num_P_pol, Wght % Misfit, Rank, Probability, num_SP, and Mode.

The depth parameter is measured in km. The magnitude parameter is measured in local magnitude (M_L). The parameters FP_unc and Aux_unc are the uncertainties for the primary and auxiliary fault planes, given in degrees. The parameter num_P_pol is the number of *P* first motion polarities used in calculating the focal mechanism. Wght % Misfit is the weighted percent misfit of first motions. Rank can range from A-F (although only A-ranked data are provided), and is a measure of focal mechanism quality. Probability is a measure of how close the mechanism is to the true solution. num_SP is the number of *S/P* ratios used in calculating the focal mechanism. Mode is the failure mode of the focal mechanism; classification is derived from Alvarez-Gomez (2009): N – normal, R – reverse, S – strike-slip, N-S – normal oblique strike-slip, R-S – reverse oblique strike-slip, S-N – strike-slip oblique normal, S-R, strike-slip oblique reverse.

Appendix C Tomography Datasets

TomoDD parameters from the TomoDD input file for SeaJade I and II are listed below. Note that the parameters are described in the documentation for both HypoDD (Waldhauser, 2001) and TomoDD (Zhang and Thurber, 2006). Descriptions for the TomoDD velocity model data tables are provided following the input parameter information.

SeaJade I:

```
*--- input file selection
* cross correlation diff times:
./dt.cc
*
*catalog P diff times:
./dt.ct
* catalog absolute times
./absolute.dat
*
* event file:
./events.dat
*
* station file:
./tomosta.dat
*
*--- output file selection
* original locations:
tomodd_seajade_03.loc
* relocations:
tomodd_seajade_03.reloc
* station information:
tomodd_seajade_03.sta
* residual information:
tomodd_seajade_03.res
* source paramater information:
tomodd_seajade_03.src
*Output velocity
tomodd_seajade_03.vel
* Vp model
Vp_model_03.dat
* Vs model
Vs_model_03.dat
*--- data type selection:
* IDAT:  0 = synthetics; 1= cross corr; 2= catalog; 3= cross & cat
* IPHA: 1= P; 2= S; 3= P&S
* DIST:max dist [km] between cluster centroid and station
* IDAT   IPHA   DIST
   3      3     400
*
*--- event clustering:
* OBSCC:    min # of obs/pair for crosstime data (0= no clustering)
* OBSCT:    min # of obs/pair for network data (0= no clustering)
```

```
* OBSCC  OBSCT  CC_format
    8      8      1
*
*--- solution control:
* ISTART:   1 = from single source; 2 = from network sources
* ISOLV:    1 = SVD, 2=lsqr
* NSET:           number of sets of iteration with specifications following
*  ISTART  ISOLV  NSET weight1 weight2 weight3 air_depth
    2        2     14    6     6     6    -1.5
* i3D delt1 ndip iskip scale1 scale2 iuses
   2    0    9     1     0.5   1.00    2
* xfac   tlim     nitpb(1) nitpb(2) stepl
  1.3   0.0002    50       50       0.2
* lat_Orig lon_Orig Z_Orig iorig rota
    49       -128     0      1     0
*
*--- data weighting and re-weighting:
* NITER:          last iteration to used the following weights
* WTCCP, WTCCS:         weight cross P, S
* WTCTP, WTCTS:         weight catalog P, S
* WRCC, WRCT:           residual threshold in sec for cross, catalog data
* WDCC, WDCT:           max dist [km] between cross, catalog linked pairs
* WTCD:   relative weighting between absolute and differential data
* THRES: Scalar used to determine the DWS threshold values
* DAMP:           damping (for lsqr only)
*       ---  CROSS DATA ----- ----CATALOG DATA ----
* NITER WTCCP WTCCS WRCC   WDCC  WTCTP  WTCTS WRCT WDCT WTCD DAMP JOINT THRES
  2    0.01   0.01    -9   -9    0.01   0.005     9   -9  10   200  1  0.2
  2    0.01   0.01    -9   -9    0.01   0.005     9   -9  10   200  0  0.2
  2    0.01   0.01     8   -9    0.01   0.005     8   -9  10   200  1  0.2
  2    0.01   0.01     7   -9    0.01   0.005     8   -9  10   200  0  0.2
  2    0.01   0.01     7   -9    0.01   0.005     7   -9  10   200  1  0.2
  2    0.01   0.01     7   -9    0.01   0.005     7   -9  10   200  0  0.2
  2    0.01   0.01     7   -9    1.0    0.5       7   -9  .1   200  1  0.2
  2    0.01   0.01     7   -9    1.0    0.5       7   -9  .1   200  0  0.2
  2    0.01   0.01     7   -9    1.0    0.5       6   -9  .1   200  1  0.2
  2    0.01   0.01     7   -9    1.0    0.5       6   -9  .1   200  0  0.2
  2      1     0.5     6   -9    0.01   0.005     6   -9   1   200  1  0.2
  2      1     0.5     6   -9    0.01   0.005     6   -9   1   200  0  0.2
  2      1     0.5     6   -9    0.01   0.005     6   -9   1   200  1  0.2
  2      1     0.5     6   -9    0.01   0.005     6   -9   1   200  0  0.2
*
*--- event selection:
* CID:      cluster to be relocated (0 = all)
* ID: cuspids of event to be relocated (8 per line)
* CID
    1
* ID
```

SeaJade II:

```
*--- input file selection
* cross correlation diff times:
./dt_mincorr_08.cc
*
```

```
*catalog P diff times:
./dt.ct
* catalog absolute times
./absolute.dat
*
* event file:
./events.dat
*
* station file:
./station.dat
*
*--- output file selection
* original locations:
tomodd_seajade_02.loc
* relocations:
tomodd_seajade_02.reloc
* station information:
tomodd_seajade_02.sta
* residual information:
tomodd_seajade_02.res
* source paramater information:
tomodd_seajade_02.src
*Output velocity
tomodd_seajade_02.vel
* Vp model
Vp_model_02.dat
* Vs model
Vs_model_02.dat
*--- data type selection:
* IDAT:  0 = synthetics; 1= cross corr; 2= catalog; 3= cross & cat
* IPHA: 1= P; 2= S; 3= P&S
* DIST:max dist [km] between cluster centroid and station
* IDAT   IPHA   DIST
   3      3     400
*
*--- event clustering:
* OBSCC:    min # of obs/pair for crosstime data (0= no clustering)
* OBSCT:    min # of obs/pair for network data (0= no clustering)
* OBSCC  OBSCT  CC_format
    8      8      1
*
*--- solution control:
* ISTART:   1 = from single source; 2 = from network sources
* ISOLV:    1 = SVD, 2=lsqr
* NSET:           number of sets of iteration with specifications following
*  ISTART  ISOLV  NSET weight1 weight2 weight3 air_depth
    2        2     18    15       15      15      -1.5
* i3D delt1 ndip iskip scale1 scale2 iuses
   2    0    9     1     0.5   1.00    2
* xfac   tlim     nitpb(1) nitpb(2) stepl
  1.3   0.0005    50       50       0.5
* lat_Orig lon_Orig Z_Orig iorig rota
    49.25  -127.75     0      1     0
*
*--- data weighting and re-weighting:
* NITER:          last iteration to used the following weights
* WTCCP, WTCCS:         weight cross P, S
```

```
* WTCTP, WTCTS:         weight catalog P, S
* WRCC, WRCT:           residual threshold in sec for cross, catalog data
* WDCC, WDCT:           max dist [km] between cross, catalog linked pairs
* WTCD:   relative weighting between absolute and differential data
* THRES: Scalar used to determine the DWS threshold values
* DAMP:           damping (for lsqr only)
*       ---  CROSS DATA ----- ----CATALOG DATA ----
* NITER WTCCP WTCCS WRCC   WDCC  WTCTP  WTCTS WRCT WDCT WTCD DAMP JOINT THRES
  5     0.1   0.05  -9     -9     0.5    0.25  -9   20   1    350   0    0.2
  3     0.1   0.05  -9     -9     0.5    0.25  -9   20   1    350   1    0.2
  5     0.1   0.05  -9     -9     0.5    0.25  -9   20   1    350   0    0.2
  5     0.1   0.05   6     10     0.1    0.05   6   10   1    350   0    0.2
  3     0.1   0.05   6     10     0.1    0.05   6   10   1    350   1    0.2
  5     0.1   0.05   6     10     0.1    0.05   6   10   1    350   0    0.2
  5     1.0   0.5    6      5     0.1    0.05   6    5   0.1  300   0    0.2
  3     1.0   0.5    6      5     0.1    0.05   6    5   0.1  300   1    0.2
  5     1.0   0.5    6      5     0.1    0.05   6    5   0.1  300   0    0.2
  5     1.0   0.5    6      2     0.01   0.005  6    2   0.1  300   0    0.2
  3     1.0   0.5    6      2     0.01   0.005  6    2   0.1  300   1    0.2
  5     1.0   0.5    6      2     0.01   0.005  6    2   0.1  300   0    0.2
  5     1.0   0.5    6      1     0.01   0.005  6    2   0.1  300   0    0.2
  3     1.0   0.5    6      1     0.01   0.005  6    2   0.1  300   1    0.2
  5     1.0   0.5    6      1     0.01   0.005  6    2   0.1  300   0    0.2
  5     1.0   0.5    6      0.5   0.01   0.005  6    2   0.1  300   0    0.2
  3     1.0   0.5    6      0.5   0.01   0.005  6    2   0.1  300   1    0.2
  5     1.0   0.5    6      0.5   0.01   0.005  6    2   0.1  300   0    0.2
*
*--- event selection:
* CID:      cluster to be relocated (0 = all)
* ID: cuspids of event to be relocated (8 per line)
* CID
    1
* ID
```

Data used in the below tables are available from the Open Science Forum at (https://osf.io/w4d3y/?view_only=bded7b7583484cc0a3282f4cce02b79f). Descriptions of the tables are as follows:

Appendix Table C.1. P-wave tomography model for SeaJade I.The model is included in the file 'Appendix_Table_C1.txt', and the columns are organized as follows:

Longitude, latitude, depth, V_P

Appendix Table C.2. S-wave tomography model for SeaJade I.The model is included in the file 'Appendix_Table_C2.txt', and the columns are organized as follows:

Longitude, latitude, depth, V_S

Appendix Table C.3. P-wave tomography model for SeaJade II.The model is included in the file 'Appendix_Table_C3.txt', and the columns are organized as follows:

Longitude, latitude, depth, V_P

Appendix Table C.4. S-wave tomography model for SeaJade II.The model is included in the file 'Appendix_Table_C4.txt', and the columns are organized as follows:

Longitude, latitude, depth, V_S